Solar-Terrestrial Centre of Excellence

Annual Report 2020

Belgian Science Policy Office belspo

Royal Observatory of Belgium

RMI

BIRA·IASB

.be

STCE

Solar-**T**errestrial **C**entre of **E**xcellence

https://stce.be/

Ringlaan 3

B-1180 Brussels

Tel.: +32 2 373 0211

Fax: + 32 2 374 9822

Front page: *The Solar Orbiter satellite was launched from Cape Canaveral in Florida on 10 February 2020. An ESA-led mission with strong NASA participation, its main goals are to take the closest ever images of the Sun, to observe the solar wind and the Sun's polar regions, and to unravel the mysteries of the solar cycle. Solar Orbiter carries 10 scientific instruments, one of which is the Extreme Ultraviolet Imager (EUI) which has an important contribution from the Royal Observatory of Belgium. Due to the sudden outbreak of the COVID-19 pandemic and subsequent lockdowns and quarantines, the testing and commissioning of EUI had to be performed exceptionally from people's home, and with just a minimal staff in the control centre. Nonetheless, the results were successful, the spacecraft became fully operational, and after EUI's first light images, the newly discovered "campfires" became a household term in solar physics.*

(Credits: ESA - S. Corvaja)

Table of Contents

A word from the STCE coordinator

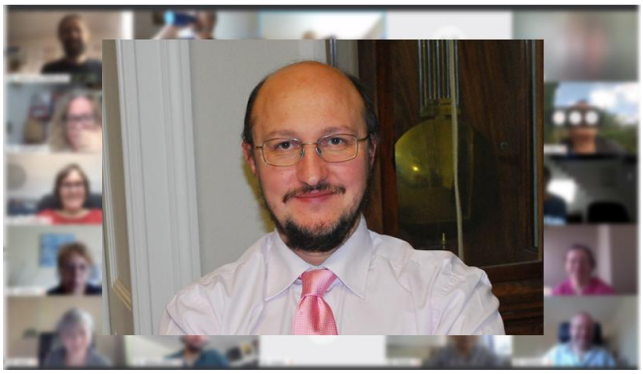

Dear Readers,

2020 was a year which we will always refer to as ‘before’, ‘during’ and ‘after’.

In some respects, it was a year to quickly forget. It gave us a strong blow as human beings and forced us to put everything on hold. Nature, however, kept on as it always does: the very old willow trees bloomed, bees hustled to the first flowers after a long winter sleep. Worries of man made no difference.

In other respects, it was a year to learn. We can only hope that we will have grown from this. As scientists, we found new ways to collaborate and, in a sense, lift ourselves above the virus. Some of our learnings should be preserved. It is not always justified to fly to the other end of the world, even for science.

It was a year that also passed. Luckily.

It was a year that forced us to look ahead. And that is what we did. We set out for new horizons and pushed ourselves and the European space weather and space climate community to make a new start.

That is what this report is about.

Ronald Van der Linden
General Coordinator of the Solar-Terrestrial Centre of Excellence
Director General of the Royal Observatory of Belgium

Structure of the STCE

The Solar-Terrestrial Centre of Excellence is a project of scientific collaboration that focuses on the Sun, through interplanetary space, up to the Earth and its atmosphere.

The solid base of the STCE is the expertise that exists in the 3 Federal Scientific Institutes of the Brussels Space Pole: the Royal Observatory of Belgium, the Royal Meteorological Institute and the Royal Belgian Institute for Space Aeronomy. The STCE supports fundamental solar, terrestrial and atmospheric physics research, is involved in earth-based observations and space missions, offers a broad variety of services (mainly linked to space weather and space climate) and operates a fully established space weather application centre. The scientists act at different levels within the frame of local, national and international collaborations of scientific and industrial partners.

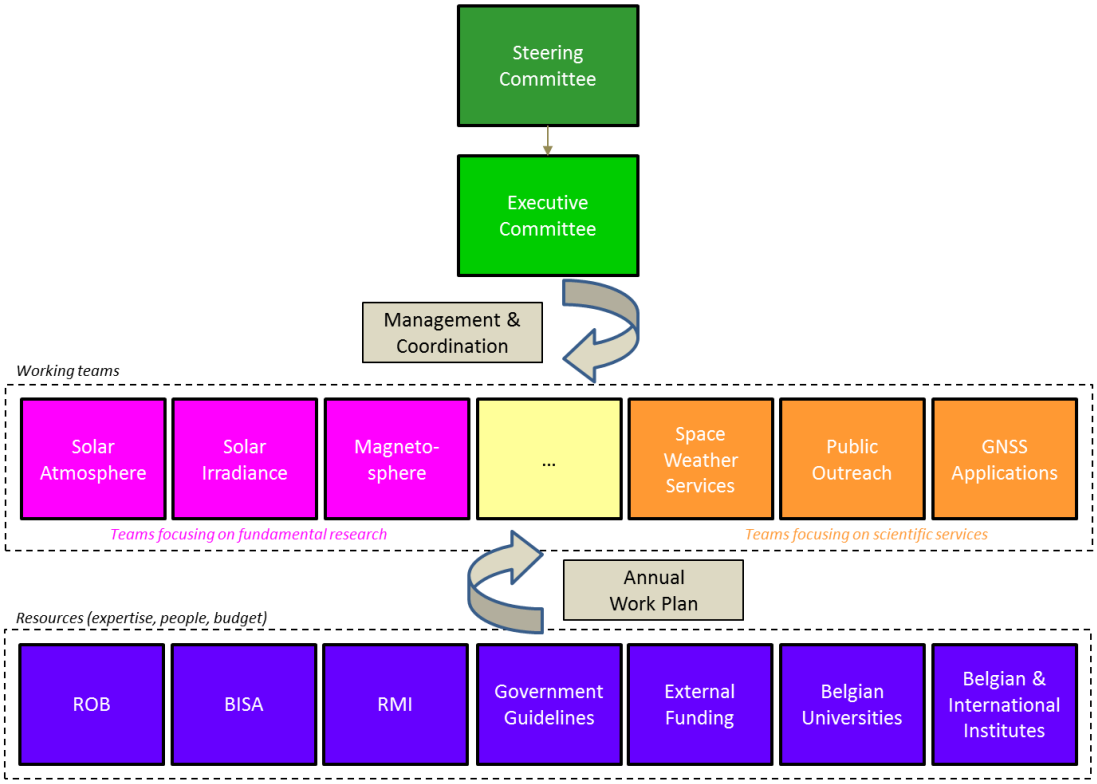

Figure 1: The STCE management structure

The STCE's strengths are based on sharing know-how, manpower, and infrastructure.

In order to optimize the coordination between the various working groups and institutions, as well as the available resources such as ICT, personnel and budget, a management structure for the STCE was put into place, consisting of a steering committee and an executive committee.

The ***steering committee*** takes all the final decisions on critical matters with regard to the STCE. It assures the integration of the STCE into the 3 institutions and the execution of the strategic plans. It is composed of:

- BELSPO Director General "Research Programmes and Applications"

  Dr. Frank Monteny (BELSPO)

- Director General of each of the 3 institutions at the Space Pole

  Dr. Ronald Van der Linden (ROB)
  Dr. Daniel Gellens (RMI)
  Dr. Martine De Mazière (BISA)

The ***executive committee*** assures the global coordination between the working groups and the correct use of the budgetary means for the various projects. It also identifies new opportunities and is the advisory body to the Steering Committee. It is composed of:

- STCE Coordinator

  Dr. Ronald Van der Linden

- Representatives of the research teams in the 3 institutes

  Dr. David Berghmans (ROB)
  Dr. Carine Bruyninx (ROB)
  Dr. Johan De Keyser (BISA)
  Dr. Norma Crosby (BISA)
  Dr. Stanimir Stankov (RMI)
  Dr. Stijn Nevens (RMI)
  Dr. Hugo De Backer (RMI)

A promotional movie giving a flavor of the STCE's tasks, interactions and various research programmes can be found via the STCE website (in English, and subtitled in French and Dutch).

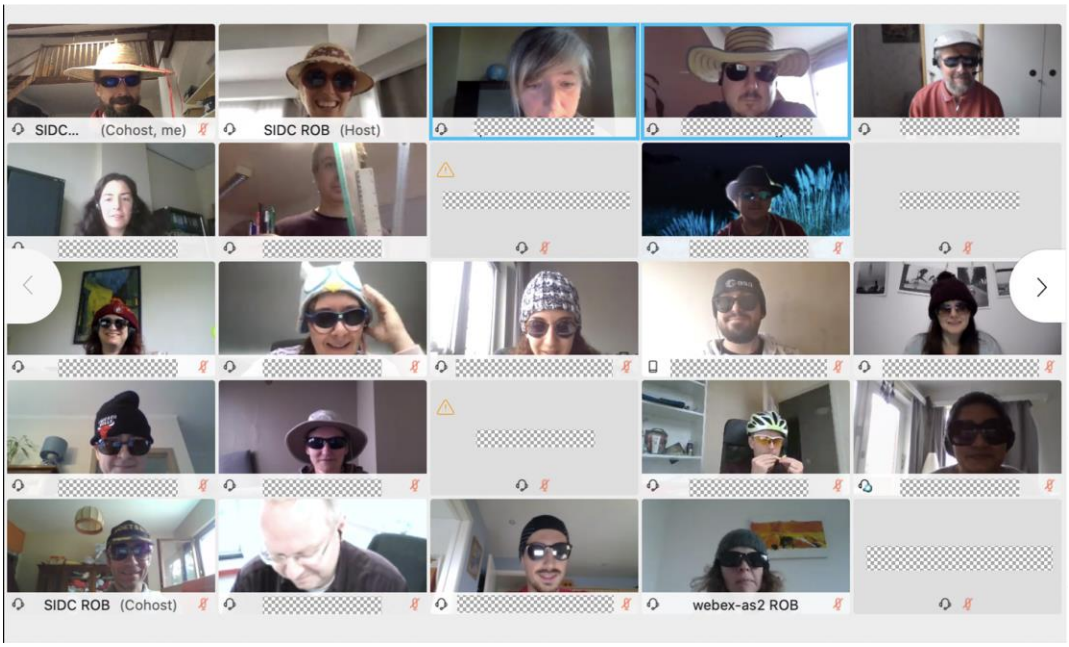

Life at the STCE - Online meetings were numerous during the COVID-19 pandemic. To have some fun, the participants in this Monthly Management Meeting dressed up with sunglasses and hat. The "a-team" organised many more such enjoyable activities mainly on a dedicated Slack channel, keeping spirits high.

Life during COVID-19 - Credits: El Arroyo

Monitoring space weather: solar-terrestrial highlights in 2020

The official annual sunspot number (SN) for 2020, as determined by the WDC-SILSO (World Data Centre - Sunspot Index and Long-term Solar Observations), was 8.8. This is an increase compared to 2019 (3.6), indicating that the new solar cycle 25 (SC25) has begun. A press release issued by SILSO on 15 September and coordinated with NASA and NOAA stated that solar cycle minimum was reached in December 2019 with the SILSO smoothed monthly SN at 1.8, which is even lower than the previous minimum in December 2008 (2.2). SILSO's Spotless Days page indicated there were 192 spotless days, with the longest stretch of 34 spotless days from 2 February till 6 March.

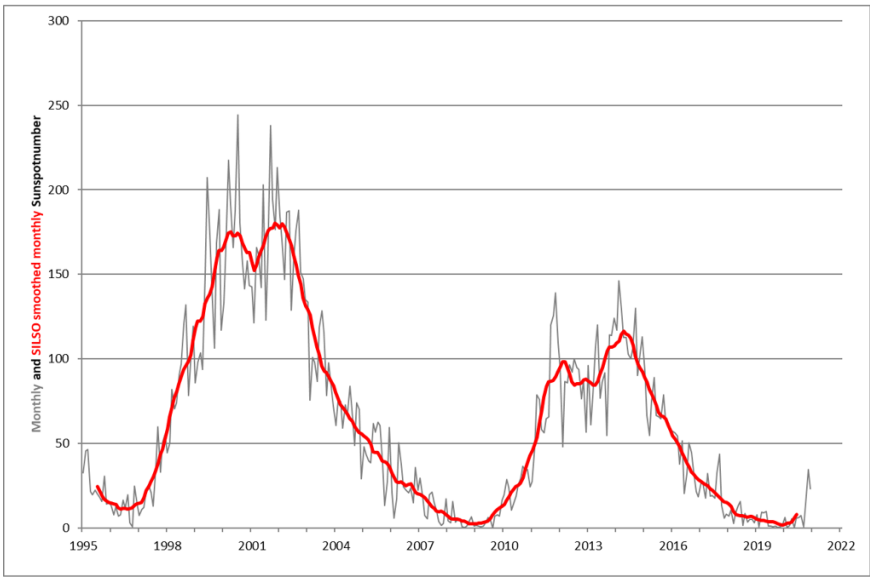

*Figure 2: The evolution of the monthly and SILSO smoothed monthly SN (1995-2020 ; **SILSO formula**). A minimum SN of 1.8 was reached in December 2019.*

Increased sunspot activity was observed from late October till early December. Active region NOAA 2778 developed quickly into a relatively large group on 25 October, and was joined on 28 October by a smaller but relatively more complex region NOAA 2779 to its northeast. NOAA 2781 rotated into view on 2 November, quickly increasing in size. At its maximum on 6 November, its sunspot area had the equivalent of nearly 3 times the surface area of the Earth (NOAA), and it was reported a naked eye sunspot (seen using eclipse glasses) by several solar observers worldwide. During the last days of November, several

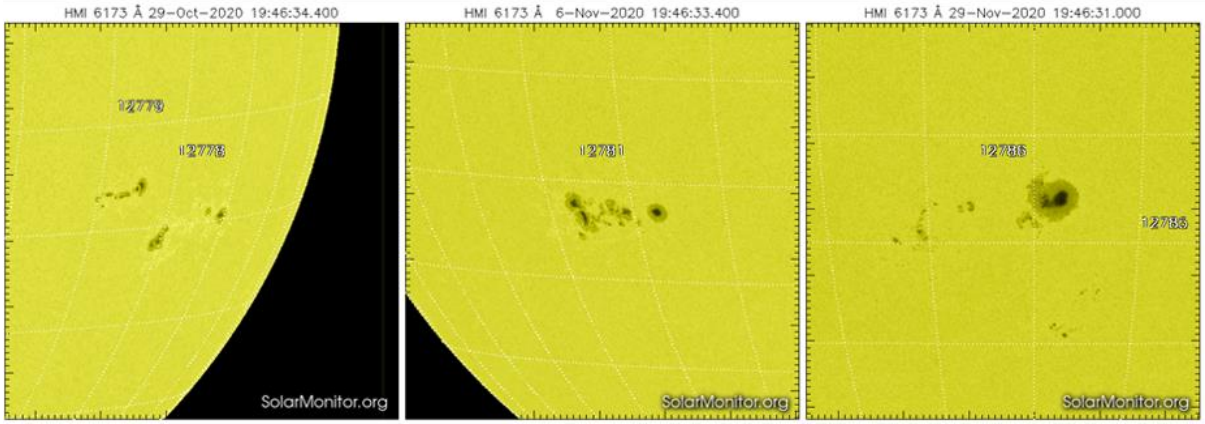

*Figure 3: A view on the most prominent sunspot groups in 2020. On the left the NOAA 2778/2779 duo on 29 October, in the middle NOAA 2781 on 6 November, and on the right NOAA 2786 on 29 November. None of these groups produced M-class flares. **SDO/HMI** imagery taken from the **SolarMonitor.org** website.*

sunspot groups became visible driving the International Sunspot Number (ISN) to its highest levels in 2020. On 29 November, there were no less than 6 groups present at the same time, with the ISN reaching 96, a value not seen since the last episode of major solar activity back in September 2017. The main sunspot group was NOAA 2786, of which the largest spot was reported visible to the naked eye and having a sunspot area corresponding to roughly 6 times the entire surface of the Earth. The presence of so many sunspots also drove the observed 10.7cm solar radio flux above 100 sfu (solar flux units, with 1 sfu = 10^{-22} W m^{-2} Hz^{-1}), for the first time this solar cycle. It reached a maximum value of 116.3 sfu on 29 November, again values not seen in more than 3 years. Despite their size, these regions had relatively simple magnetic configurations and produced only C-class flares.

In 2020, no proton events or Ground Level Enhancements (GLEs) were registered. However, the Sun produced 2 M-class flares. On 29 May, while still behind the northeast solar limb, an active region near +35 degrees latitude produced an M1.1 flare followed 3 hours later by a C9.3 flare. This was the first M-class event since 20 October 2017, and thus also of the new SC25. The associated coronal mass ejections (CMEs) bumped into the fanning, overarching magnetic field of the Sun's northern polar coronal hole (CH), getting deflected towards the east ("left") as if they had hit a brick wall. Consequently, also the CMEs had a very similar (and very distorted) outlook. When the likely source region (NOAA 2764) had finally rotated over the east limb, only a very small spot was remaining, barely visible even in larger telescopes.

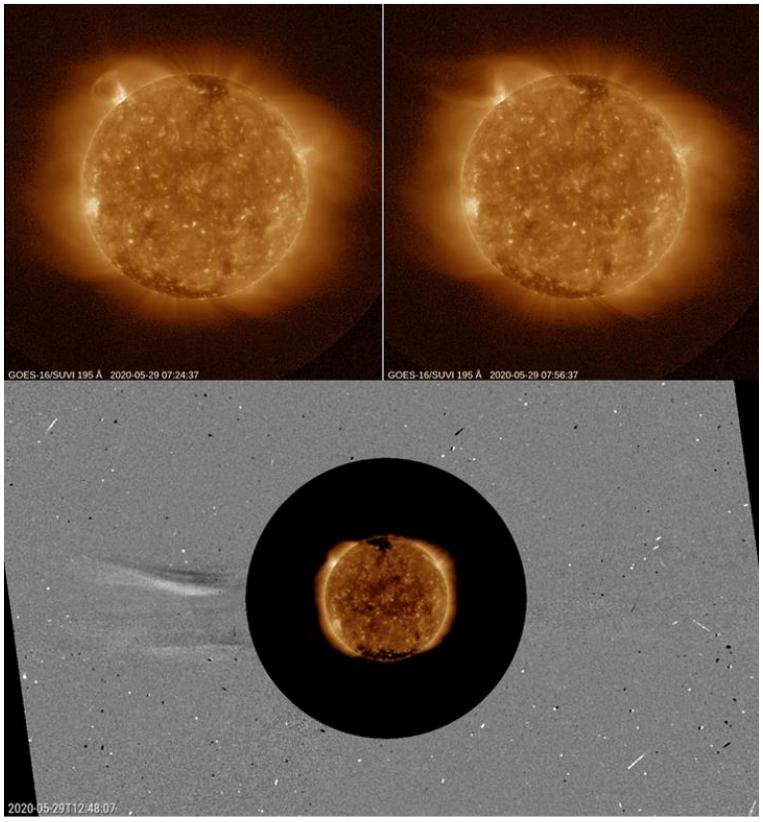

*Figure 4: (Top) Extreme ultraviolet (EUV) view obtained by SUVI onboard **GOES** showing the ejected plasma cloud associated with the M1 flare from 29 May, its deformation following the collision with the overarching magnetic field from the northern polar coronal hole, and (bottom) the heavily distorted (almost jetlike) CME that became eventually visible in **SOHO/LASCO** coronagraphic difference images (one image subtracted from the next).*

On 29 November, a strong long duration M4.4 flare was produced by a region that was still behind the southeast limb. Despite its location, post-flare coronal loops quickly towered a considerable 65,000 km above the solar limb. The associated CME was the fastest so far this solar cycle, with a speed of around 1250 km/s. The very same region was also the source of the first halo CME of SC25 on 24 November, albeit on the Sun's farside as seen from Earth. When the source region NOAA 2790 rounded the east limb, it was an all-in-all relatively simple and decaying active region consisting mainly of a single sunspot. Nonetheless, it continued to surprise with a series of low-level homologous C-class flares on 5-6 December and a spectacular long duration C7.4 flare on 7 December. The associated CME had an earth-directed

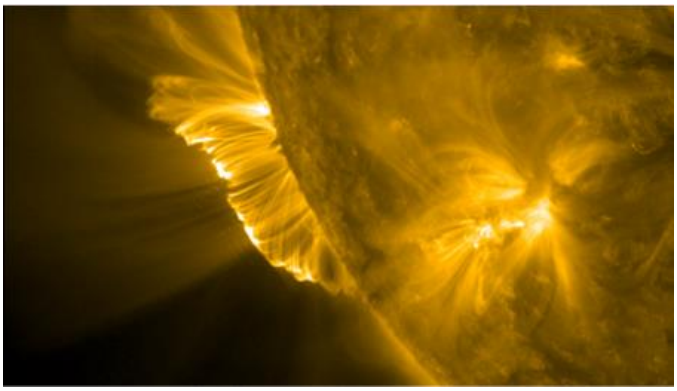

Figure 5: An arcade, a series of post-eruption coronal loops, became visible following the M4 flare on 29 November.

component arriving 3 days later. The solar wind speed jumped from 450 km/s to 560 km/s, however this interplanetary CME did not possess long lasting negative Bz, thus resulting in only unsettled to active geomagnetic conditions.

Geomagnetic activity was determined mostly by the wind streams associated with coronal holes. Several days with minor storming occurred, however the Dst never reached -60 nT, indicating these were not very intense disturbances. Late September, a series of CH related high speed wind streams (HSS) were the source of moderate storming (K_p = 6 ; Dst = -57 nT - WDC Kyoto). Solar wind speed gradually increased from values near 360 km/s on 23 September to values peaking around 675 km/s on 29 September (DSCOVR), and was above 500 km/s from 24 September till 2 October. These persistent HSS generated elevated levels of energetic (energies of more than 2 MeV) electrons in the Earth's outer radiation belt with daily maxima above the alert threshold of 1000 pfu (particle flux units; 1 pfu = 1 electron / (cm^2 s sr)) from 24 September onwards as measured by GOES. A maximum flux of more than 42,000 pfu was reached on 5 October, and the daily electron fluence was at high levels during this period. High levels of these electrons can lead to electrostatic discharges (ESD) resulting in malfunctions of a satellite and occasionally even in satellite failure. Even after the solar wind speed has decreased to nominal values, high levels of energetic electrons can still persist for several days.

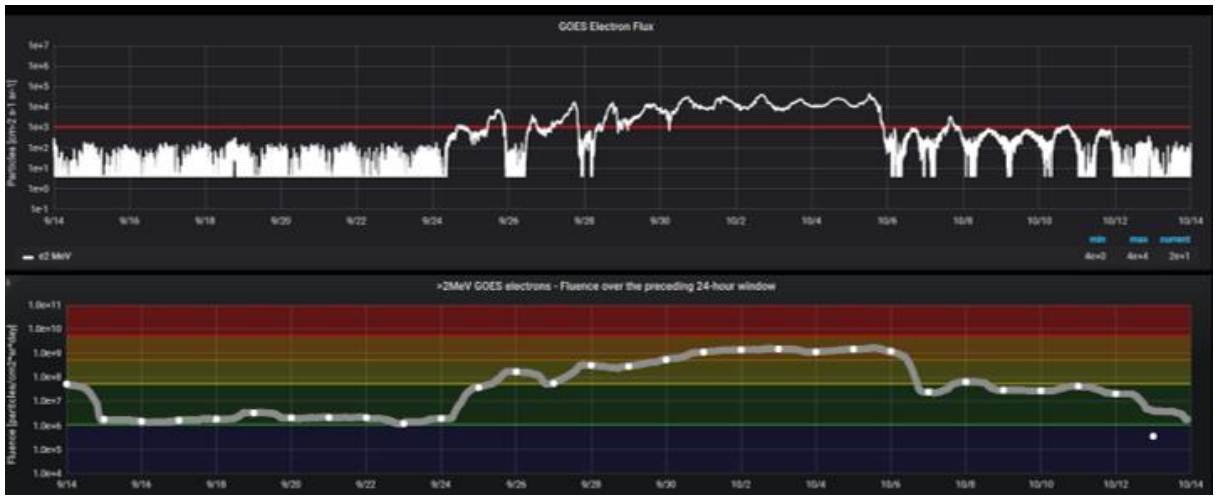

Figure 6: A screenshot of the SIDC/RWC dashboard for the SWx forecasters showing the evolution of the >2 MeV electron flux (top) and 24h electron fluence (accumulated electron flux over 1 day) for the period from 14 September till 14 October. Note both vertical axes are on a logarithmic scale, and the horizontal axis has 2-days increments. The high-speed wind stream (HSS) which arrived around 23 September influenced the >2 MeV electron flux and 24-hours fluence until early October, driving both parameters to high levels, i.e. resp. above 10,000 pfu and into the "orange" zone (> 5 . 10^8 electrons/(cm^2 sr day)).

The lack of substantial CMEs in 2020 was the main reason that no Forbush decrease was observed throughout the year (Oulu neutron monitor). Due to the ongoing solar cycle minimum, cosmic rays were at very high levels. The maximum seems to have been slightly lower than during the previous solar cycle minimum transit in 2008-2010. Due to the typical broad maximum for the current magnetic configuration of the Sun, a precise timing of this maximum is more difficult to establish (see the NMDB for the data from different neutron monitor stations - Figure 7). Cosmic rays are known to pose a radiation hazard to passengers and crew on polar flights, and to astronauts. Increased cosmic ray levels affect the composition of the Earth's upper atmosphere, and it is also believed they may help trigger lightning and lightning-associated effects such as sprites.

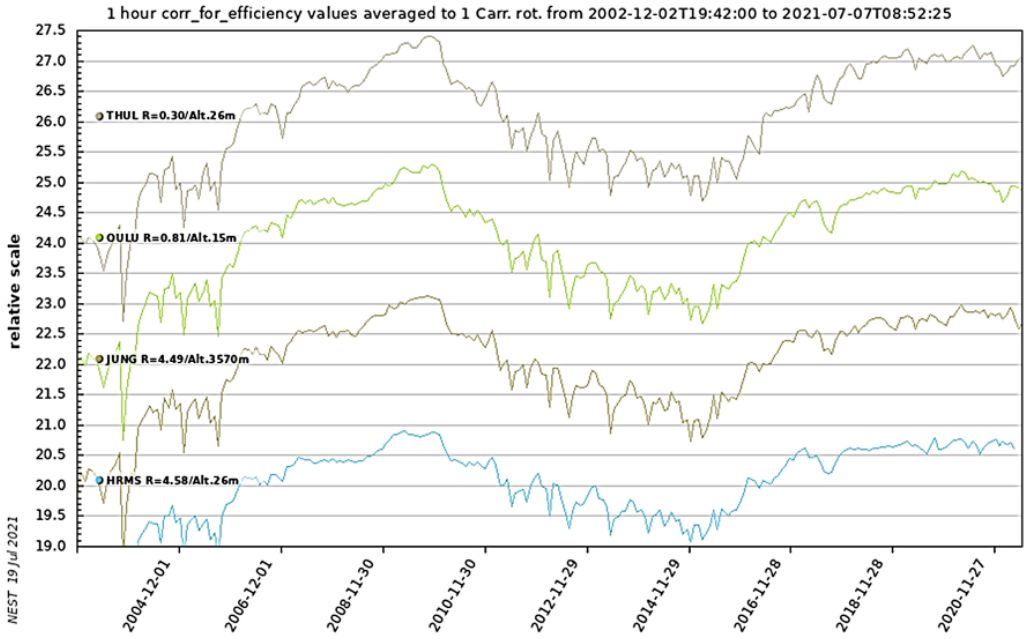

Figure 7: Several neutron monitor stations such as from (top to bottom) Thule (Greenland), Oulu (Finland), Jungfraujoch (Austria) and Hermanus (South-Africa) indicated a broad maximum in the neutron count plateauing in 2019-2020 and at a slightly lower level than during the previous solar cycle minimum in 2008-2009. The vertical axis is a relative scale expressed in % and based on a long-term average from December 2002 till July 2021.

Life during COVID-19 - Credits: El Arroyo

Public outreach meets Science

SWEC - Space Weather Education Center

Introduction - The sporadic and massive eruptions of highly energetic matter and radiation from the Sun can trigger space weather processes in the Earth's atmosphere and magnetosphere. Technology that relies on satellite navigation and radio wave propagation can be impacted, as well as large energy transport systems like electrical grids. Harmful radiation at flight altitude can increase when a solar storm hits Earth.

Impacted stakeholders need to learn about those natural hazards and increase their resilience and awareness. The need for space weather staff, like meteorologists, to meet certain competence levels will increase as more nations and institutes start to install a space weather room, similar to the familiar meteo rooms.

Figure 8: The SWEC logo was created by Olivier Lemaître.

The Space Weather Education Center (SWEC) can help - SWEC offers Space Weather courses and training covering the Sun, solar storms, heliosphere, ionosphere, magnetosphere, space weather impacts on thermosphere, instruments and methods to observe solar activity, reading and interpreting STCE space weather forecasts, impact on navigation systems, radio communication, radiation hazards. It includes visits to the beating heart of our space weather service centre and other key players in space weather operations. The programme focuses on gaining knowledge by fact-learning, short guest lectures, 'meet & greet' of people working in the field and easily accessible methods like games, quizzes and hands-on exercises given by qualified staff.

SWEC offers standard space weather introductory courses as well as modules tailored to the needs, level and business of the participants, e.g. for aviation.

Since 2017, the STCE organises courses on Space Weather and its impacts. Typically, a course takes 3 to 4 days. We keep the number of participants per session low (usually around 8) to guarantee a more personal approach. Due to the COVID-19 pandemic, there were no SWICs organised in 2020. For 2021, we'll move to an online classroom which is only a few clicks away, making it easy for foreigners to follow the course.

Proven inhouse expertise - As part of the STCE, SWEC can rely on its academic and service expertise by its World Data Centre for the Sunspot index; strong involvement in space and ground-based missions including instrumentation-building; research in solar physics, in the space weather domain, in the field of GNSS; a dedicated solar particle radiation group. In 2001, we already started operating a space weather room where researchers continuously collect, analyse and interpret solar data. More recently, the STCE teamed up with scientific institutes in other European countries, jointly creating the Pan-European Consortium for Aviation Space weather User Services - PECASUS, that provides space weather services for civil aviation. Our goal is to become an official ISO-certificated training centre following the World Meteorological Organization (WMO) regulations. Check us out at https://www.stce.be/SWEC

Awards and highlights from STCE researchers

ESPD's "PhD Thesis Prize" for STCE collaborator - Camilla Scolini started her PhD in 2016, executing her job jointly at ROB and at KU Leuven (KUL). In her thesis, she examines the propagation of Coronal Mass Ejections (CMEs) in the heliosphere and their geoeffectiveness upon arrival at the Earth (see page 20 of this Annual Report). By the end of her PhD, Camilla had published more than 10 papers in recognized international journals, and given numerous invited talks at international conferences. She successfully defended her thesis in May 2020, a copy of which can be found at the KU Leuven website.

In 2021, the European Solar Physics Division (ESPD) awarded her the "PhD Thesis Prize", for significant contributions on numerical modelling and observational analyses of the propagation of coronal mass ejections. Camilla has recently received the prestigious Jack Eddy Postdoctoral Fellowship, awarded by the NASA Living With a Star (LWS) programme, that she will carry out at the University of New Hampshire, continuing space weather research. We definitely expect to hear more from her!

Paper in the spotlight - The paper "Height dependency of solar eclipse effects: the ionospheric perspective", written by the STCE collaborators Tobias Verhulst and Stanimir Stankov, was published in the Journal of Geophysical Research: Space Physics in June 2020. Just a few weeks later, it was already selected by the AGU for a research spotlight in their magazine Eos. Quite an accomplishment, in view of the dozens of research papers that are published every week!

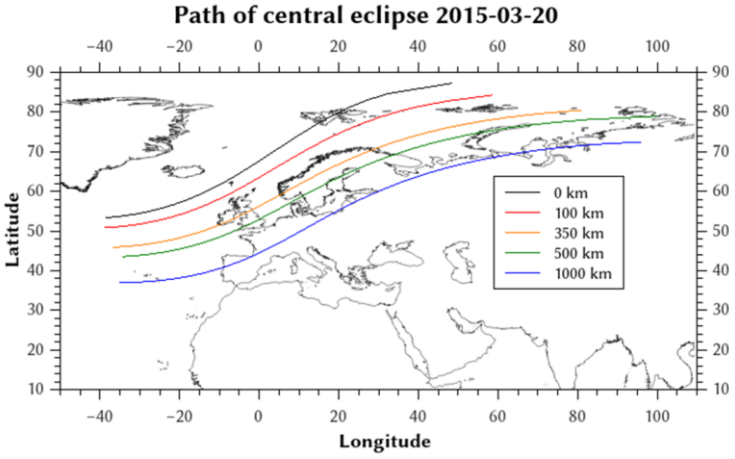

Figure 9: Another example of the authors' research. The path of the central eclipse over the North Atlantic and the Svalbard archipelago on 20 March 2015 at various altitudes, from sea level to 1000 kilometers. The eclipse path was farther to the south at higher altitudes.

In their paper, the authors point out that a reliable interpretation of solar eclipse effects on the geospace environment, and on the ionosphere in particular, necessitates a careful consideration of the so-called eclipse geometry. The standard, most popular way to look at the eclipse geometry is via the two-dimensional representation (map) of the solar obscuration on the Earth's surface.

Such "surface maps" are widely used to readily explain some of the solar eclipse effects including, for example, the well-known decrease in total ionization (due to the substantial decrease in solar irradiation), usually presented by the total electron content (TEC). However, many other effects, especially those taking place at higher altitudes, cannot be explained in this fashion. Instead, a more detailed description of the umbra (and penumbra), would be required. The paper by Tobias and Stanimir addresses the issue of eclipse geometry effects on various ionospheric observations carried out during the total solar eclipse of 21 August 2017. The researchers found that the path of the eclipse at higher altitudes better explains the electron depletions observed there during that solar eclipse.

ESPD's "Media of the Month" award goes to ROB's solar observer - On Saturday 6 June at 14:02:16 UTC, the USET solar telescopes (USET: Uccle Solar Equatorial Table) of the Royal Observatory of Belgium (ROB) imaged a transit of the International Space Station (ISS). ISS is the largest artificial object in space and it flies in a low Earth orbit at about 400 km altitude. Hence, this satellite can be seen with the naked eye as a moving bright point from the Earth's surface at night.

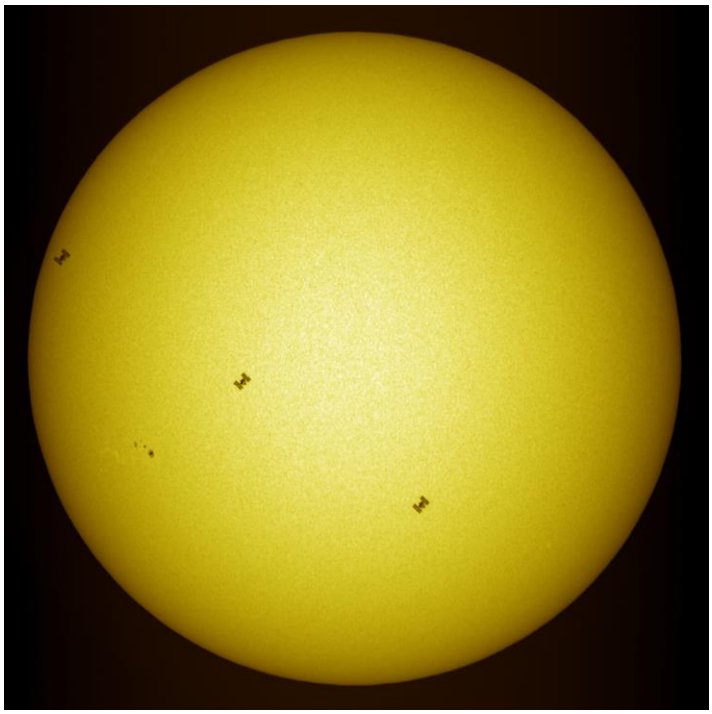

Figure 10: The ISS transit on 6 June as photographed by Sabrina Bechet.

As shown in Figure 10, the ISS appears as three successive black structures taken at around 250 milliseconds interval each. The striking feature of the ISS -its large solar panels- are nicely resolved with the white-light telescope at ROB. As the ISS moves fast (about 8 km/s), the total transit duration is very short, being only a fraction of a second (0.8 seconds for this event), hence it needs a fast-recording camera to be caught.

Sabrina Bechet, solar observer at the SIDC/USET, was there at the right time and the right place to take this amazing picture. In December 2020, the European Solar Physics Division (ESPD) bestowed upon her its "Media of the Month" award. Congratulations Sabrina!

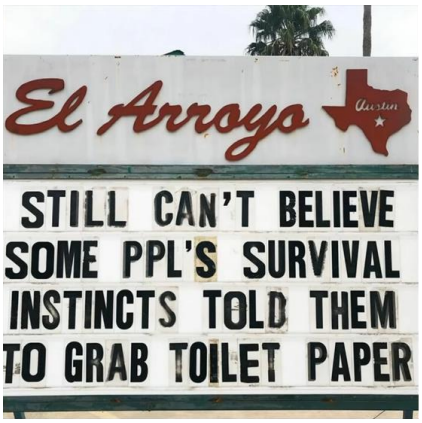

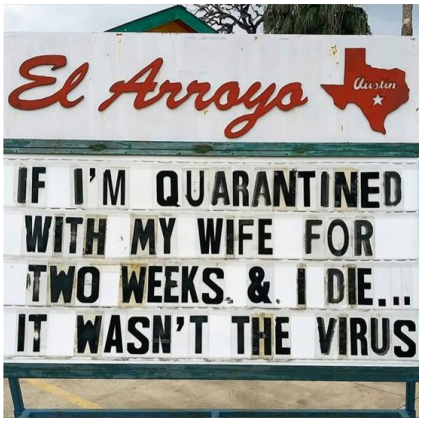

Life during COVID-19 - Credits: El Arroyo

Fundamental research

EUI first light and discovery of campfires on the Sun

On 12 May 2020, only two months after the launch of Solar Orbiter, the doors of its Extreme Ultraviolet Imager (EUI) were opened for the first time, a crucial moment in the mission's life. It is only during this 'First Light' moment that the EUI team can find out whether the telescope survived the launch and is working properly. For EUI, this first light was especially challenging as the whole of Europe, including the Mission Operation Centre in Darmstadt, was in lockdown as a result of the COVID-19 pandemic. In normal circumstances, instrument experts are present in the Operations Room during this procedure so that communication is quick and efficient. Performing this type of operations from home through simultaneous tele-conferences was tough for all teams involved, yet very successful. The high-resolution images of EUI (Figure 11) were breathtaking and immediately led to a scientific discovery: campfires on the Sun.

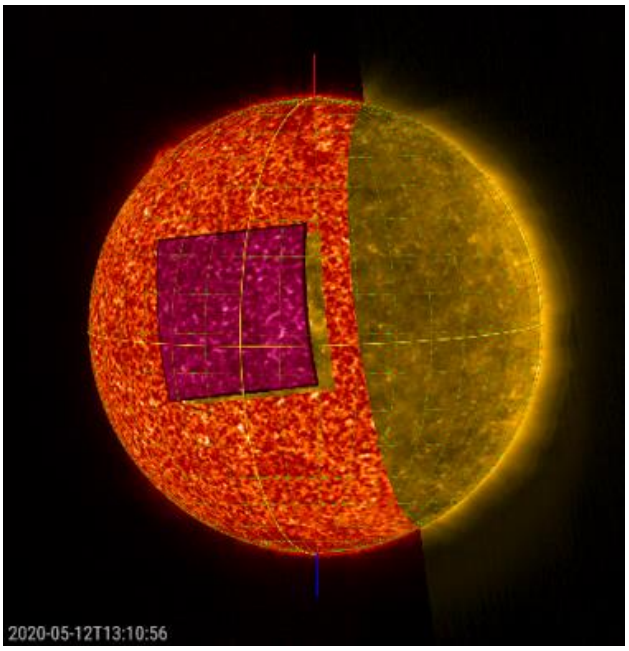

Figure 11: The EUI consists of three telescopes, the Full Sun Imager (FSI) and two High Resolution Imagers (HRI), which are optimized to image in Lyman-α and EUV (17.4 nm, 30.4 nm) to provide a coverage from the chromosphere up to the corona. The above image is a combination of the first light images of EUI in each of its 4 channels. The large red area is the FSI 30.4 nm channel imaging the solar transition region. The square violet area is the HRILYA channel imaging in the Lyman-alpha line and showing the solar chromosphere. The yellow/golden coloured areas are taken in the 17.4 nm bandpass and show the 1 million degree corona by HRIEUV (square area below the HRILYA square) and the FSI (big area on the right).

Solar Orbiter makes one complete orbit around the Sun in 168 days. The point of the orbit that is closest to the Sun is called 'perihelion'. At perihelion, the speed of the spacecraft approaches the speed with which the Sun rotates around its own axis. While the spacecraft hovers closely above the solar surface, the onboard cameras are in an excellent position to photograph the solar atmosphere. The EUI cameras made images overwhelmingly rich in small detail. David Berghmans, principal investigator of EUI telescope, explains: "It is like zooming in on the iconic blue marble Earth and suddenly you see details which you had never expected: rivers, cows, a road with cars, smoking chimneys. This is exactly what we see with EUI: We can now see the solar corona at work on a micro-level."

On 30 May 2020, Solar Orbiter was roughly halfway between the Earth and the Sun, meaning that EUI was closer to the Sun than any other solar telescope has ever been. This allowed the EUI telescopes to see features in the solar corona of only 400 km across.

Figure 12 shows a small part of the solar atmosphere observed on that day. The sequence of images taken on that day shows an unexpected multitude of small loops, bright spots and dark, moving fibrils. The tiny brightening dots and loops sparked immediate excitement in the EUI team as they show up remarkably sharp and contrasted, ubiquitously all over the so-called "quiet Sun" where nothing seemed to happen in

older data. Only now, looking at the Sun with the unprecedented high resolution of EUI, we see very tiny flashes of light almost everywhere. These flashes of light were named 'campfires' by the EUI scientists. They might contribute to the high temperatures of the solar corona and to the origin of the solar wind, possibly answering the question that solar physicists have been tackling for decades.

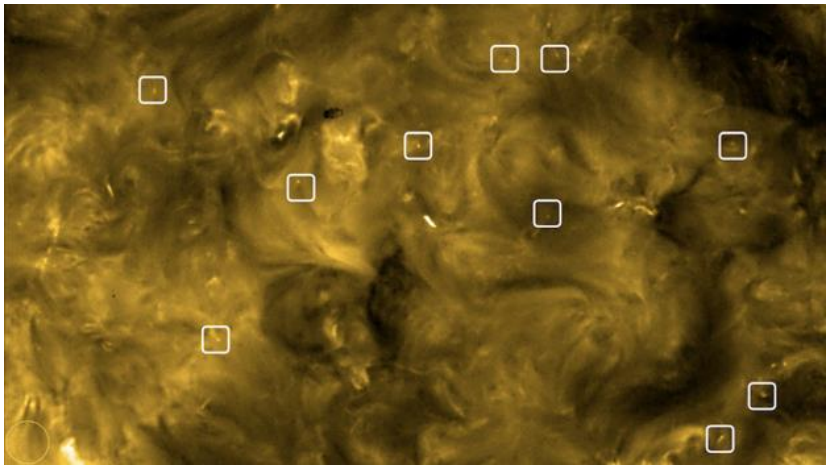

Figure 12: Image from the High Resolution EUV Imager of EUI taken on 30 May 2020. The squares indicate examples of little campfires. The yellow circle in the lower left corner illustrates the size of the Earth for comparison.

It is well known that the solar atmosphere produces flares, sudden flashes of light that release magnetic energy. The biggest solar flares can impact the Earth and its technologies in a process called space weather. The campfires that EUI discovered are their little nephews, typically a billion times smaller than common flares (Figure 13). They are totally insignificant each by themselves, but, summing up their effect all over the Sun, they might be the dominant heating contribution of the solar corona. This idea ("nanoflare heating") has been proposed a long time ago by Eugene Parker (indeed, the scientist after whom the Parker Solar Probe is named). Further research will be needed to find out whether the campfires are indeed just miniature versions of the big flares or whether they are different in some way. We will also need to collect statistics on campfires and compare with other instruments (such as the SPICE spectrograph) to determine the significance of their heat output.

As the mission continues, Solar Orbiter will go closer to the Sun and this will increase the instrument's resolving power by a factor of two at closest approach, allowing it to see small features of only a few hundred km in size. The whole team is looking forward to this new data. However, contrary to previous missions in which the EUI team members have participated, the distance between the Sun and the spacecraft is continuously changing. They will have to get used to the fact that the images that EUI makes are continually changing, as EUI takes pictures of the Sun from a different angle and distance day after day. The EUI team is excited to calibrate, analyse and interpret the new images. New science is on the way!

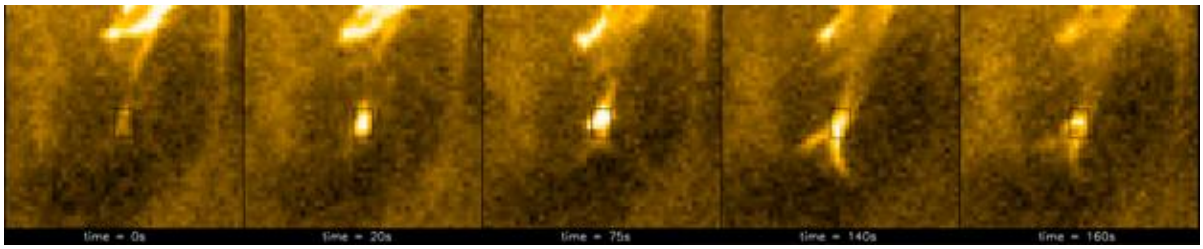

Figure 13: A zoom-in on a campfire lasting less than 3 minutes. The campfire appearance suggests the interaction of two small coronal loops. The interaction region (the black square) is roughly 800x1200km.

A modern reconstruction of Richard Carrington's observations (1853-1861)

In the framework of the ongoing re-calibration of the 400-year long sunspot number series undertaken in 2015 by the World Data Center SILSO, in 2020, the focus has shifted to the 19th century. Indeed, SILSO researchers are now revisiting original data that were under-exploited in a period when sunspot data were much sparser than in the 20th and 21st centuries. The ultimate goal of their work is to ensure the homogeneity of our longest record of solar activity over multiple past centuries. A key observer over the years 1853-1861 was Richard Carrington, a prominent solar scientist who measured the solar differential rotation and defined the heliographic coordinate system that is still in use nowadays.

Figure 14: Carrington's original drawing for 7 July 1860

With the help of an active observer from the SILSO worldwide sunspot network, Thomas Teague (UK), a full recounting from the original historical drawings and logbooks was carried out. These are preserved at the Royal Astronomical Society in England (see Figure 14). This recount was necessary because, until now, the only numbers available came from Rudolf Wolf, the initiator of the sunspot number in the 19th century. However, the way Wolf derived those numbers was indirect and poorly documented. With the new recounting, the scientists could now fully assess Wolf's counting method and shed light on the quality of the sunspot number series over that period.

The study shows that the new recounts by T. Teague closely match the counts by R. Wolf on their overlapping days of observation (see Figure 15), which means that the observers from the SILSO network today indeed have a similar way of counting as the creator of the sunspot number series. This testifies to its homogeneity over the past 200 years. From our analysis, we can now tell with confidence that Wolf himself counted sunspots directly from Carrington's original drawings over 1859-1860, but that afterwards, he used instead an indirect conversion from lists of sunspot areas provided by Carrington in his correspondence.

Moreover, the cause of a previously reported but unexplained constant 7° longitude shift of the sunspot positions in Carrington's tables was identified. As it turns out, Carrington simply adopted slightly different coordinate references in his groundbreaking work than those used nowadays. As such, the very high accuracy of his work has now been confirmed.

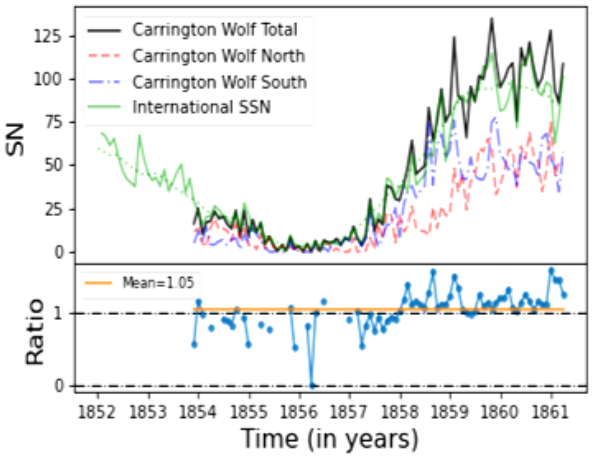

Figure 15: Comparison of recounts by Teague and Wolf's observations on overlapping days.

The resulting recounted 1853-1861 Carrington sunspot number series have now been added to the data accessible on the SILSO Web portal. The corresponding article was submitted to Solar Physics in early 2021 and has meanwhile been published (Bhattacharya et al., 2021).

Helmet streamers in the solar corona and their oscillations

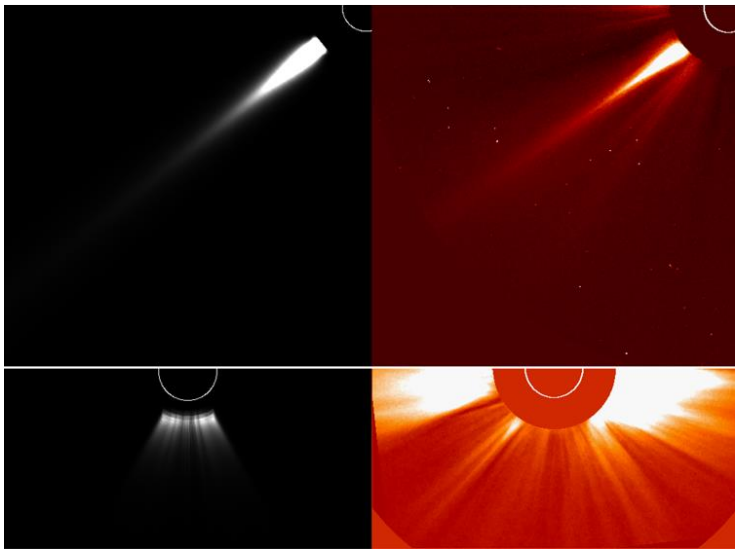

Figure 16: Two views of the same coronal streamer. The left panels show the modeled corona. These are compared with the observed corona as shown in the right panels, with images resp. from STEREO A COR2 (top) and SOHO/LASCO (bottom).

Bieke Decraemer started her PhD in 2016, when she was awarded a ROB PhD grant. Her PhD project was made jointly at ROB and at KU Leuven. Bieke's thesis is dedicated to the study of coronal helmet streamers. Streamers are the largest structures observed in the corona, and they are its true building blocks, especially during solar maximum. In the lower solar corona, helmet streamers consist of closed magnetic loop-like arcades connecting to the solar surface. In the outer solar corona, they extend to a radial stalk connecting to the out-flowing solar wind. The radial stalk is actually a plasma sheet seen edge-on.

One of the best ways to study coronal structure is to observe it with two widely separated telescopes, like LASCO onboard the SOHO spacecraft and COR2 onboard the STEREO A spacecraft. This works like the human vision with two eyes providing a better idea about the three-dimensional structure of an object than the information given by one eye only. Bieke combined the data taken by two coronagraphs to derive the first quantitative three-dimensional streamer density model consistent not with one but with both COR2 and LASCO images (see Figure 16).

Sometimes, streamers are perturbed by coronal mass ejections (CMEs) propagating in the corona. They may start to oscillate, with the oscillations propagating outwards like waves (Figure 17). These waves are important as they allow us to derive the plasma parameters in the solar corona, similarly to seismic waves used to derive the properties of Earth's interior. This technique is called "coronal seismology". It allowed Bieke to determine the solar wind speed in streamers, a quantity notoriously difficult to measure.

In Figure 18, the blue dots with error bars show the streamer wave speeds derived by two independent methods (shown along the

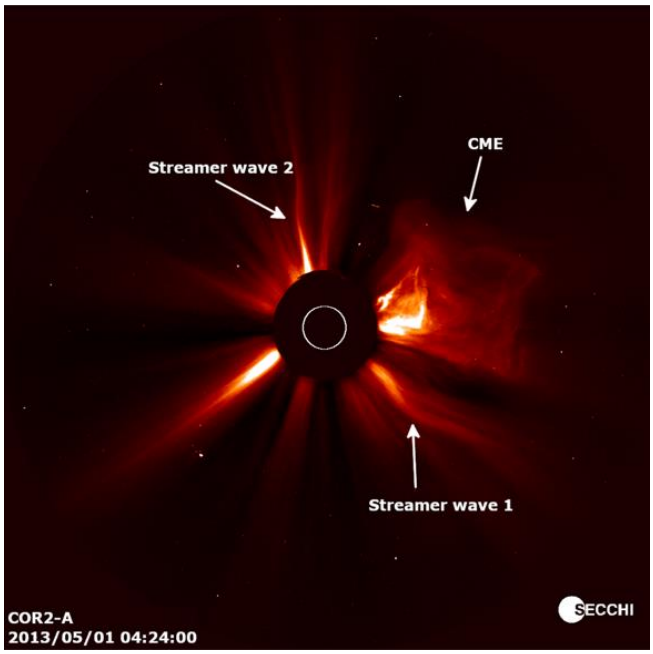

Figure 17: A coronal mass ejection (CME) going towards the right of the image perturbs two streamers and triggers their oscillations that start propagating radially outwards as waves.

horizontal and vertical axes). For comparison, the green line is derived from a theory that does not take into account the solar wind propagation in streamers. It is clear that it does not describe well the observed data points. The dashed black line represents the same theoretical fit, but corrected for the solar wind speed of around 300 km/s. This line approximates the observed data points much better.

After having successfully defended her PhD in October 2020, Bieke decided to leave science and start a new job in industry, for which we wish her all the best of luck. We will miss you Bieke!

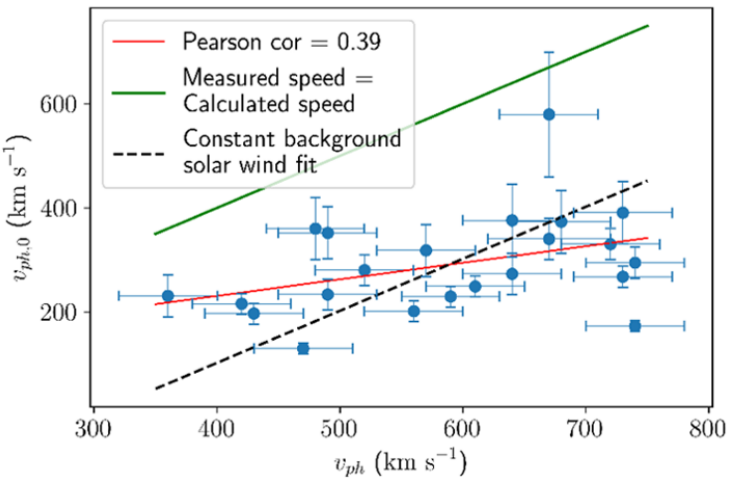

Figure 18: The blue dots with error bars show the streamer wave speeds derived by two independent methods. The green line does not take into account solar wind propagation in streamers, whereas the dashed black line contains a correction for the solar wind speed of around 300 km/s. This line approximates the observed data points much better.

Evolution of coronal mass ejections in the heliosphere

Camilla Scolini started her PhD in 2016, when she was awarded a ROB PhD grant. She executed her job jointly at ROB and at KU Leuven (KUL). Her thesis is based on a very relevant and lively topic in space weather and solar physics: the propagation of Coronal Mass Ejections (CMEs) in the heliosphere and their geoeffectiveness upon arrival at the Earth. Furthermore, she also studied how they affected other locations of the heliosphere. In this way, the term geoeffectiveness had to be broadened, and thus helioeffectiveness came to life. So, Camilla's PhD work, apart from interesting scientific results, also created new words! The main tool Camilla used was a newly developed 3D heliospheric magnetohydrodynamic (MHD) model: the EUropean Heliospheric FORecasting Information Asset, EUHFORIA. Snapshots of an EUHFORIA run can be found in the STCE Annual report of 2016 (Figures 41-42).

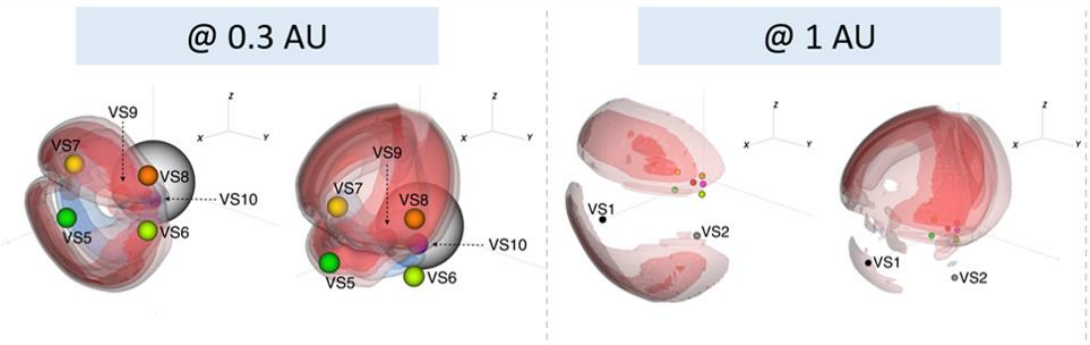

Figure 19: 3D contour plots showing the difference in radial velocity of a CME between run pairs, at different times in the simulations, at different locations in the heliosphere, and for various virtual spacecraft (VSx). From Scolini et al. (2020).

Camilla developed innovative techniques that are now being used by other researchers. For example, she included the possibility to simulate data at the locations of all the current and new space missions (e.g. Parker Solar Probe and Solar Orbiter) and, more generally, at any location in the heliosphere with the use of virtual spacecraft (Figure 19). She also implemented a clever way to separate the radial and expansion speed of CMEs (a long-standing problem in CME research) in order to be used directly by the model.

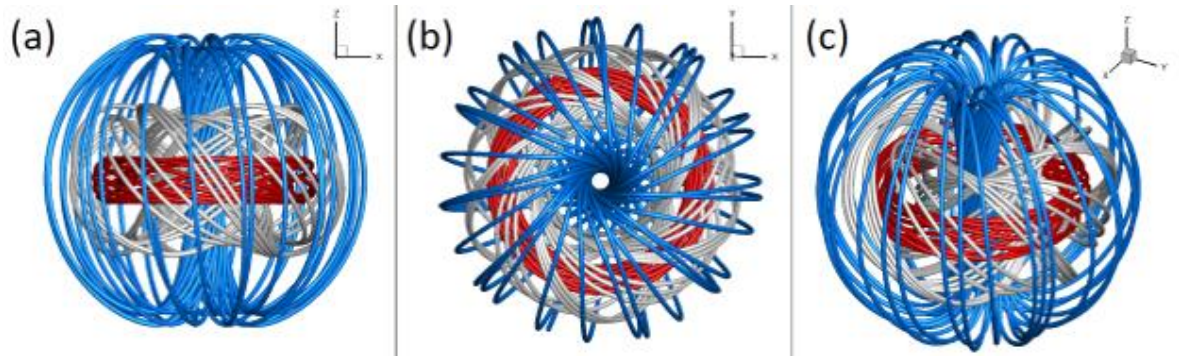

Figure 20: The internal magnetic field configuration of CMEs. Based on a 3D linear force-free spheromak. Different colours mark field lines characterized by different morphologies. (a): side view. (b): top view. (c): angled view.

She also made critical updates to the model, including the propagation of CMEs with internal magnetic field configuration (see Figure 20), which is now the state-of-the-art model for CMEs. Camilla helped with the inclusion of EUHFORIA into the space weather Regional Warning Centre in Brussels, where it is currently being validated in order to be used as a forecasting tool. She also coupled EUHFORIA with magnetospheric models, some of these couplings are currently being used in the Virtual Space Weather Modelling Centre (VSWMC), an ESA project currently being developed by a consortium led by KU Leuven, with the participation of ROB.

For her work, in 2021, the European Solar Physics Division (ESPD) awarded her their "PhD Thesis Prize", for significant contributions on numerical modelling and observational analyses of the propagation of coronal mass ejections (see page 13 of this Annual Report).

Turbulence at small scales in the solar wind

The solar wind - the steady stream of charged particles blown away by the Sun in all directions - is known to possess properties that are typical of "turbulent" flow. "Turbulence" is a term that stems from fluid research and plays a role in the aerodynamics of a car or an airplane. The underlying idea is the following: Fluids (like the air) flow around an object (an airplane) in a flow pattern that is characterized by the size of the object (e.g. as the air is pushed aside and flows over and under the wings). Large-scale motion of air represents a certain energy (e.g. which is used by a windmill to produce electricity). Now in most practical situations such a flow creates "eddies" - small-scale, local whirlwinds. This is a process that takes some of the energy from the large-scale flow and uses it to create eddies at a smaller scale. In fact, this is a recursive process, as eddies create even smaller eddies, and so on, up to the molecular scale, where this sort of random motion is what we call "heat". This recursive process is called "the turbulent cascade": Energy inherent in large-scale motions is progressively transported to ever smaller small-scale motions.

The situation in the solar wind is similar, in that it also exhibits a turbulent cascade, but there are two fundamental differences - which is why turbulence in the solar wind is not very well understood at present. The first difference is that the solar wind is so diluted that particles hardly collide with each other, as opposed to the air that we breathe. This makes it hard to understand how energy can be transferred between them. The second difference is that the particles are electrically charged (there are ions and electrons, positively and negatively charged particles). These particles cannot move freely because they feel the electric and magnetic forces in the solar wind. In general, they can move easily along the solar wind magnetic field lines, but much less so in directions perpendicular to those field lines. According to the laws of electromagnetism, the motion of the particles generates an electric current and creates a magnetic field fluctuation. So, the fundamental question of solar wind turbulence can be formulated as: How is energy from the large scales (the scale of the Sun, responsible for differences in solar wind flow speeds) transported to small scales (small velocity and density fluctuations that have been observed by spacecraft)?

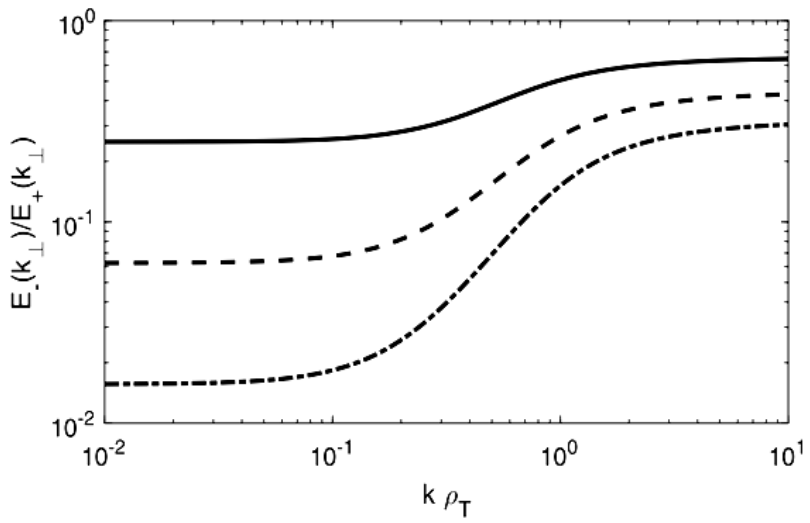

Figure 21: Evolution of the spectral power ratio E_-/E_+ between sunward and anti-sunward Alfvén waves in the solar wind from large spatial scales (small $k\,\rho_T$) to small spatial scales (large $k\,\rho_T$). The curves correspond to three different situations.

The most common type of solar wind magnetic field and particle fluctuations is known as "Alfvén" waves. They bear a certain resemblance to radio waves, but they propagate only along the magnetic field (while ordinary radio waves propagate easily in all directions). Thus, they propagate along the interplanetary magnetic field either toward or away from the Sun. Both types of waves are observed, but the ones moving away from the Sun are more prevalent. This is not surprising since the Sun itself is the origin of large-scale fluctuations in the solar wind, which can only propagate away from the Sun. This so-called "turbulence imbalance" (more outward waves than inward ones) is known to be the same at large spatial scales, but it is still not clear if this behaviour persists down to small scales. Solving this puzzle would tell us something about how the turbulent energy cascade actually works.

We developed a theoretical model of the interactions between inward and outward propagating Alfvén waves (Gogoberidze and Voitenko, 2020a and 2020b). This model predicts that there should be less differences between outward and inward propagating Alfvén waves at very small spatial scales in the solar wind (then we're talking about a few hundred kilometers or so). For the specialists: When the wave scales approach the ion gyroradius scale (~100 km), kinetic effects become significant and lead to efficient energy exchange between counter-propagating waves.

Figure 21 shows the ratio E_-/E_+ between the energies in sunward and anti-sunward waves as a function of the spatial scale (the inverse of the wavenumber k normalized by the ion gyroradius ρ_T). At large spatial scales (small k ρ_T, comparable to the size of the Sun) the proportion E_-/E_+ is small: There are much more outward waves. At small spatial scales (~100 km) the proportion is closer to 1, although there are still more outward waves than inward ones.

These findings are in agreement with observations of the solar wind. We hope that the observations from the Parker Solar Probe and Solar Orbiter spacecraft, dedicated to the study of the solar wind, will provide much more detailed observations of these fluctuations - and that our theoretical results would match with them. If so, we can be certain that our model of the interactions between Alfvén waves correctly explains the behaviour of solar wind turbulence.

Research on the Earth's radiation belts

Variations during geomagnetic storms - The Energetic Particle Telescope (EPT), launched on the satellite PROBA-V in May 2013, has been providing flux measurements at an altitude of 820 km for more than 7 years. This detector was designed to provide uncontaminated spectra of electrons, protons and alpha particles. We have investigated the strong electron flux variations for energies E > 500 keV associated with the geomagnetic storms observed since 2013.

Electron flux dropout events are observed during the main phase of each storm and even during substorms. A rapid reduction of the electron flux is noted throughout the outer electron radiation belt at all energies above about 0.5 MeV on timescales of a few hours. The electron spectrograms measured by the EPT between 2013 and 2019 show that after each geomagnetic storm, dropout events are followed by a flux enhancement starting first at low L values (L is approximately the distance from the centre of the Earth, expressed in Earth radii, of the farthest point on a magnetic field line), and reaching the slot region or even the inner radiation belt for the strongest storms. Dropouts appear at all energies as measured by EPT and penetrate down to L~3.5 for the strongest events. Dropouts are observed at low Earth orbit (LEO) each time the Dst index (Disturbance storm time index, a geomagnetic index for severe space weather perturbations) has an inverted peak < -40 nT.

We also determined the link between the Dst index and the minimum value of the L-shell where the dropouts deplete the outer belt, as well as the non-linear relation between Dst and the minimum L-shell where the flux penetrates in the slot region or even the inner belt during the storms.

We showed that flux enhancements appear at lower L only for big storm events with Dst < -50 nT. They penetrate down to an impenetrable barrier with a minimum L-shell related to Dst and to the energy. For E > 1 MeV, this limit is also linked to the plasmapause position (the sharp limit of cold plasma originating from the ionosphere). The mechanism of formation of the plasmapause was investigated to determine the circumstances for the generation of plumes, shoulders or other structures (Bandic et al., 2020).

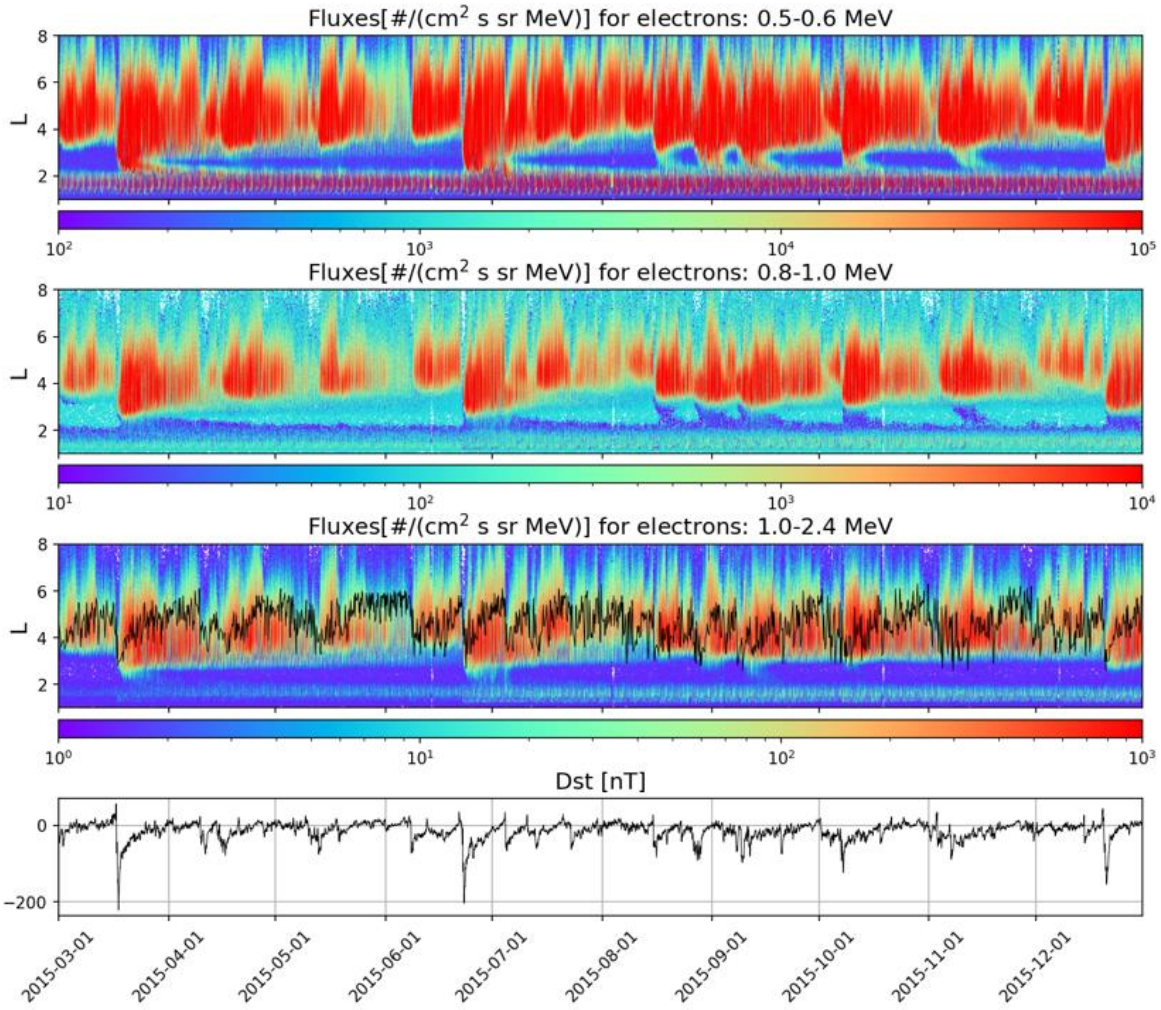

*Figure 22: Electron flux measured by EPT in Channel 1 (500-600 keV, upper panel), Channel 4 (0.8-1.0 MeV, second panel) and Channel 5 (1.0-2.4 MeV, third panel) from 1 March till 31 December 2015. In the third panel, the black line corresponds to the plasmapause position measured by two instruments onboard the Van Allen Probes. Bottom panel: Dst index measured during the same period (Pierrard et al., **2020**).*

Loss due to ground-based transmitters - Human activity also influences electron fluxes of the radiation belts. We demonstrated that the ground-based transmitter in northwest Australia scatters electrons and make them lost from the radiation belts (Cunningham et al., 2020). Radio waves with a low enough frequency can reflect off Earth's surface as well as the ionosphere. These waves bounce back and forth in the Earth-ionosphere waveguide, enabling AM (Amplitude Modulation) radio to be heard at large distances. The ionosphere is not a perfect reflector though, and some of the transmitter wave power escapes into Earth's magnetosphere, a region where charged particles like electrons can be trapped for many months on magnetic field lines. The radio waves can scatter the trapped electrons into Earth's atmosphere, where they rapidly lose energy and no longer pose a threat to space-based assets. Understanding how naval transmitters scatter trapped electrons is needed to help us explain why electrons stay trapped for as long as they do, and enable us to predict radiation damage to the growing number of satellites that orbit Earth with low altitudes, which limits the satellite's useful lifetime.

The very low frequency (VLF) transmitter in the Northwest Cape of Australia (NWC) has previously been observed to pitch-angle scatter electrons with energies from 30-400 keV, creating enhanced fluxes measured by LEO satellites. In our work, we used observations from the EPT on PROBA-V. At low altitude (820 km), the electrons trapped in the inner radiation belt form a region of high fluxes above the South Atlantic and South America, called the South Atlantic Anomaly (SAA). We compared the measured flux, as a function of local magnetic field strength, when the NWC transmitter is "on" versus "off", and found enhanced fluxes only when NWC is "on" and located on the night side. The enhanced fluxes occur in the population gradually transitioning from "permanently trapped" to "quasi-trapped". We showed that electrons up to 800 keV (substantially higher energy than previously studied) are scattered by resonant interactions with NWC to produce enhanced fluxes. The enhanced fluxes appear at multiple L-shells for each energy channel.

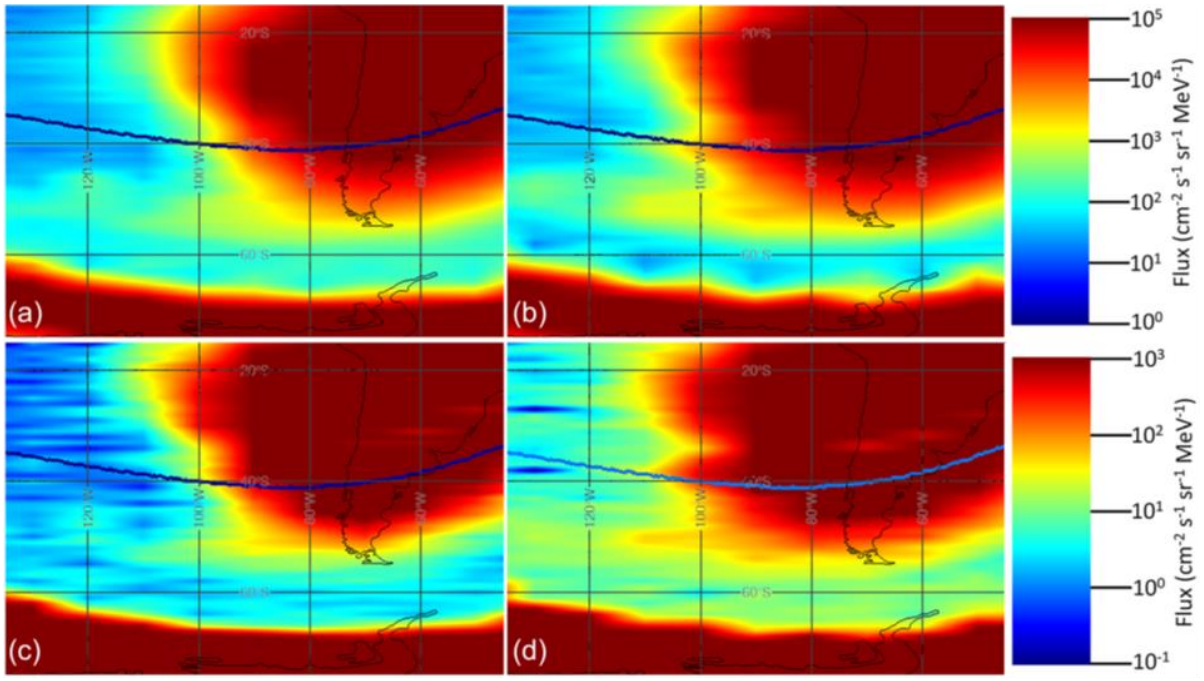

Figure 23: (top) Logarithm of the average flux in the [500-600] keV channel (spanning 1-10^5 electrons/cm² s sr MeV) as a function of geographic longitude (horizontal) and latitude (vertical) when NWC is on the night side and the transmitter is a) off, and b) on. (bottom) Same as above but for the average flux in the [600-700] keV channel (spanning 0.1-10^3 electrons/cm² s sr MeV) when the transmitter is c) off, and d) on. The outer radiation belt is the dark red band at the bottom of each image. The SAA is the dark area of red encompassing the bottom half of South-America. The curved broken line is L=1.54. (Cunningham et al., 2020)

Homogenizing GPS integrated water vapour time series

Water vapour is a key component for the Earth's climate as it is the most important natural greenhouse gas and responsible for the largest known feedback mechanism for amplifying climate change (the so-called water vapour feedback). However, due to its high variability, both temporally and spatially, water vapour is one of the most difficult quantities to measure and to predict with Numerical Weather Prediction (NWP) models. The Zenith Total Delay (ZTD) estimated from Global Navigation Satellite System

(GNSS) observations, provided world-wide at high a temporal resolution (e.g., every 5 minutes) and under all weather conditions, can be converted to Integrated Water Vapour (IWV) measurements, providing time series of this essential climate variable since the mid-nineties.

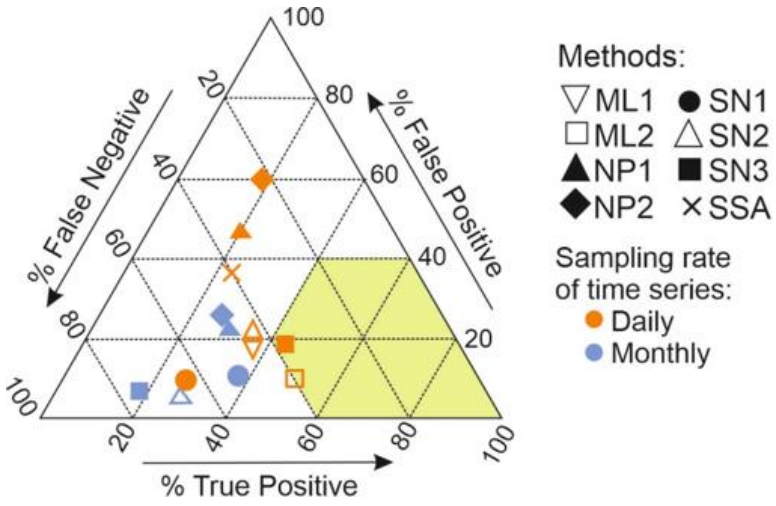

*Figure 24: Ternary graph visualizing the break identification performance of the different methods for the "moderate" data set. The performance of a method increases with decreasing number of false negatives ("misses") and false positives ("false alarms") and with increasing number of true positives ("hits"). The perfect solution would be located in the lower right corner of the triangle. Following Gazeaux et al. (**2013**), a green zone is delimited, which represents the zone of "good performance". The different break detection methods are represented by different symbols, and the colours indicate the time resolution (daily or monthly) applied in the detection procedure. The different classes of methods used are maximum likelihood (ML), nonparametric tests (NP), standard normal homogenization tests (SN), and singular spectrum analysis (SSA).*

Unfortunately, inconsistencies introduced into these long-term time series due to e.g. instrumental and/or environmental changes at GNSS stations, make climate trend analyses from these data challenging. These inconsistencies should be removed from the time series by homogenization, which is a multistep process including one or more cycles of inhomogeneity detection and bias adjustments. Detection involves analysing the climate series to locate abrupt or gradual inhomogeneities by using statistical tests and visual inspection tools and preferably supported by metadata (i.e., documentary information on known changes in the instrumentation). Adjustment is the process of using statistical approaches to reduce the bias introduced by the inhomogeneities. Both detection and adjustment should be made by comparing the series with reference time series.

In a study published in the journal Earth and Space Science (Van Malderen, Pottiaux et al., 2020), we assessed the performance of eight different break detection methods on three synthetic benchmark data sets, each consisting of 120 time series of daily IWV differences. These synthetic differences were generated from the characteristics of real GNSS IWV time series at 120 sites worldwide, and from IWV time series output by NWP model reanalysis (ERA-Interim), which served as the reference series. Each benchmark data set, includes homogeneous and inhomogeneous series with added non-climatic shifts (breaks) in the latter. Three different variants ("easy" - "moderate" - "complex") of the benchmark time series were produced, with increasing complexity, by adding autoregressive noise of the first order ("moderate") to the white noise model and the periodic behaviour ("easy"), and consecutively by adding gaps and allowing non-climatic trends ("complex"). The purpose of the three complexity levels was to study the sensitivity of each break detection methods to the various introduced aspects, ending with the "complex experiment" aiming to examine the performance in a more realistic case when the reference series are themselves not homogeneous.

We evaluated the performance of break detection methods with skill scores, Centred Root Mean Square Errors (CRMSE) between the adjusted and original homogeneous data (i.e., without the introduced non-climatic shifts), and trend differences relative to the trends of the homogeneous series. We found that most methods underestimate the number of breaks and have a significant number of false detections (see Figure 24). Despite this, the degree of CRMSE reduction is significant (roughly between 40% and 80%) in the easy to moderate experiments, with the ratio of trend bias reduction even exceeding the 90% of the raw data error (the latter being visualized by the dark bars in Figure 25).

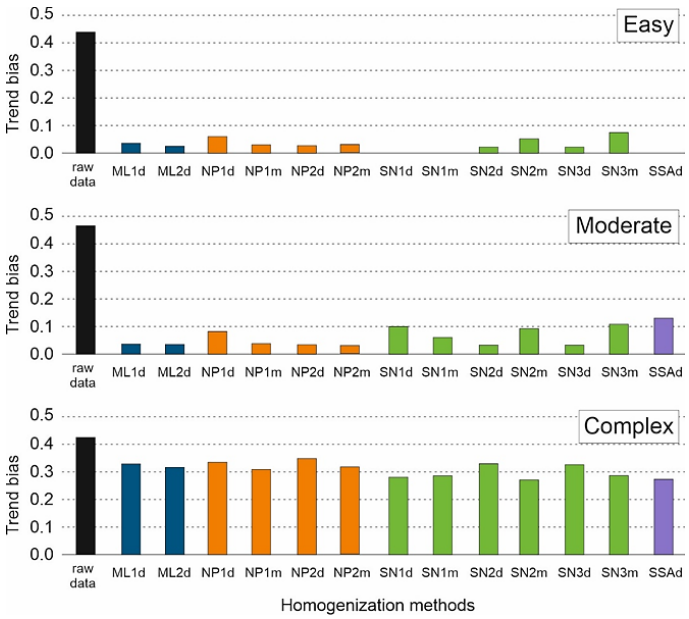

Figure 25: Mean absolute trend biases between the adjusted and homogenous synthetic IWV difference time series, for the different break identification methods. The different colours denote the different classes of the break detection methods (see also Figure 23). The time resolution is denoted by d (daily) and m (monthly) after the homogenization method name. The different panels show the trend biases for the different variants of the benchmark time series.

For the complex experiment, the improvement ranges between 15% and 35% with respect to the raw data, both in terms of RMSE and trend estimations (see again Figure 25 for the mean absolute trend bias). These results are very encouraging, and demonstrate the great potential of in particular two break detection methods for homogenizing real GNSS time series of IWV retrievals.

Life during COVID-19 - Credits: El Arroyo

Instrumentation and experiments

The Extreme Ultraviolet Imager (EUI) is off to space onboard Solar Orbiter

On 10 February 2020, the Solar Orbiter satellite was launched on an Atlas V rocket from Cape Canaveral in Florida. Solar Orbiter's mission is to take the closest ever images of the Sun, to observe the solar wind and the Sun's polar regions and to unravel the mysteries of the solar cycle. The Solar Orbiter mission is led by ESA, but has a strong participation from NASA.

Figure 26: Several EUI key consortium members pointing to what they have been working on for nearly a decade.

One of the main instruments onboard is the Extreme Ultraviolet Imager (EUI), developed by an international consortium led by the "Centre Spatial de Liège" and including the Royal Observatory of Belgium. Both institutes have a longstanding collaboration in the development of solar imagers, including EIT on the SOHO satellite and SWAP on the PROBA2 satellite. EUI consists of 3 telescopes, a Full Sun Imager and two High Resolution Imagers, that are optimized to image in the Lyman-α spectral line and in EUV. The 3 telescopes will provide coverage from the solar chromosphere up to the corona. EUI is designed to cope with the strong constraints imposed by the Solar Orbiter mission characteristics. Limited telemetry availability is, for example, compensated by state-of-the-art image compression, on board image processing and event selection.

Solar Orbiter's science mission (nominal + extended phase) is expected to last a decade. By making several Venus flybys in the coming years, the Solar Orbiter spacecraft will use the gravity of the planet to approach the Sun. The EUI high resolution telescopes are designed for a state-of-the-art spatial resolution, but by approaching the Sun, another factor 4 in sharpness increase will be achieved. It will then be possible to study details of only a few hundred kilometers in the solar atmosphere.

Later on, the gravity of Venus will be used to tilt the satellite's orbit and to enable EUI to take images from a polar perspective, something that has never been done before (see Figure 27). Studying the solar poles is of great scientific importance for understanding the Sun's magnetism and the solar activity cycle. The solar cycle lasts about 11 years and takes us from a "low solar season" with few solar storms to a "high solar season" with more frequent solar storms. Technology on Earth can be seriously disrupted by these solar storms, which are studied in the context of "space weather". By visualizing the poles and magnetic forces, the EUI instrument will contribute to unravelling the secrets of the solar cycle.

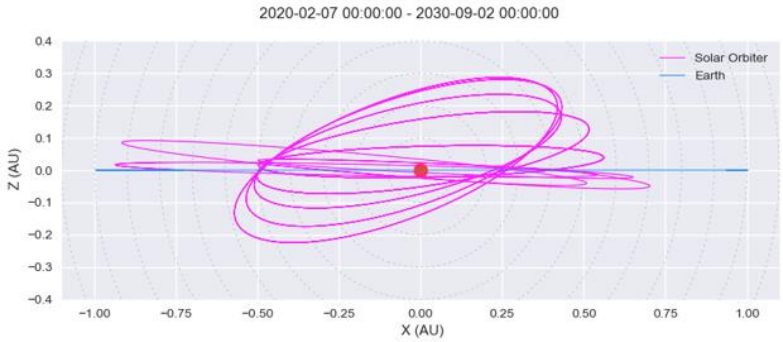

Figure 27: View of the Solar Orbiter trajectory in the X-Z plane close to the end of the extended mission timeframe. By then, Solar Orbiter will have an unprecedented view on the Sun with an inclination of 33°.

Solar Orbiter carries 10 scientific instruments. After launch, the instrument teams prepared to test their instruments, but suddenly there was the outbreak of the COVID-19 pandemic. Access to the control room in Darmstadt, Germany, had to be restricted and all testing of the instruments was interrupted. But after one week, it was decided to restart operation, with a minimal staff and in a fully COVID-19 proof way.

The rest of the commissioning work was performed from people's homes by non-stop teleconferences. Commands to operate EUI were given from living rooms, home offices, bedrooms,... Nobody would have dared to plan the commissioning with the instrument experts spread over several continents. Nevertheless, an unexpected advantage was that everybody was only a mouse click away and always immediately available.

Figure 28: The last physical meeting of the Solar Orbiter instrument teams, days before the launch and the start of the COVID-19 pandemic.

The test phase ended successfully on 25 June during an official online "Mission Commissioning Results Review" meeting with more than 50 participants. The EUI team could look back on a very intense but efficient test period. The EUI instrument was officially cleared for scientific operations.

SIMBA: Launch and follow-on mission

SIMBA CubeSat launched - On 3 September 2020, the SIMBA CubeSat (RMI) was launched alongside the PICASSO CubeSat (BISA) using an Arianespace Vega rocket. CubeSats are very small satellites built using cubes of 10 cm as building blocks and offer a (relatively) low-cost possibility to do research in space. SIMBA is a small satellite (three cubes big) with a big ambition: to measure one of the fundamental drivers of climate change. Based on measurements from the 30 cm long satellite, the aim is to calculate the total energy budget of our planet.

SIMBA stands for "Sun-earth IMBAlance", which means the difference in the amount of incoming and outgoing radiation at the top of the atmosphere. To measure the radiation, the satellite is equipped with a radiometer. The aim is to determine whether it is possible to measure both the incoming radiation from the Sun and the outgoing radiation from the Earth with the same instrument, which has never been done before. By subtracting the outgoing radiation from the incoming solar radiation, we get a figure for the Earth's radiation balance - the amount of energy our planet retains rather than reflects or radiates away.

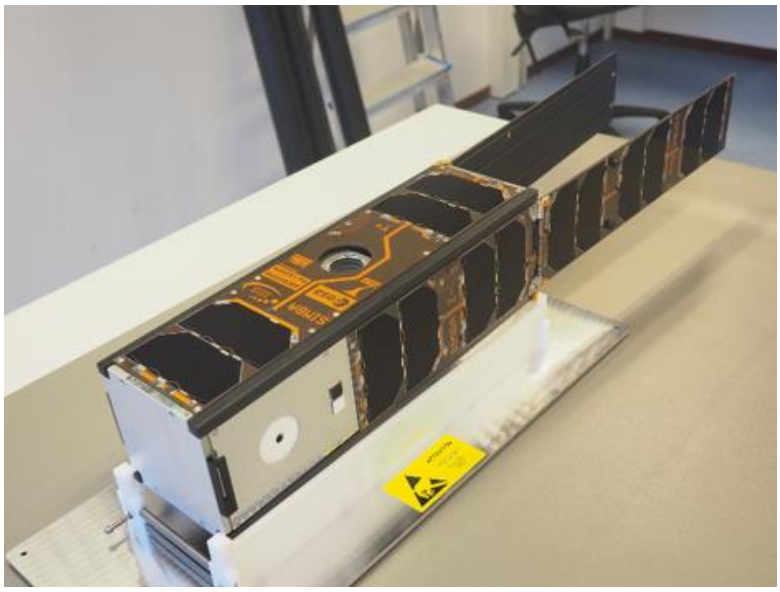

Figure 29: The finished satellite with open solar panels as it will look in space. Only the antennas are stowed away.

The radiometer was built by the same team that built various radiometers measuring the Total Solar Irradiance from ground and space. The DIARAD VIRGO instrument aboard the Solar & Heliospheric Observatory (SOHO) is such an instrument that has celebrated its 25 years in space in 2020.

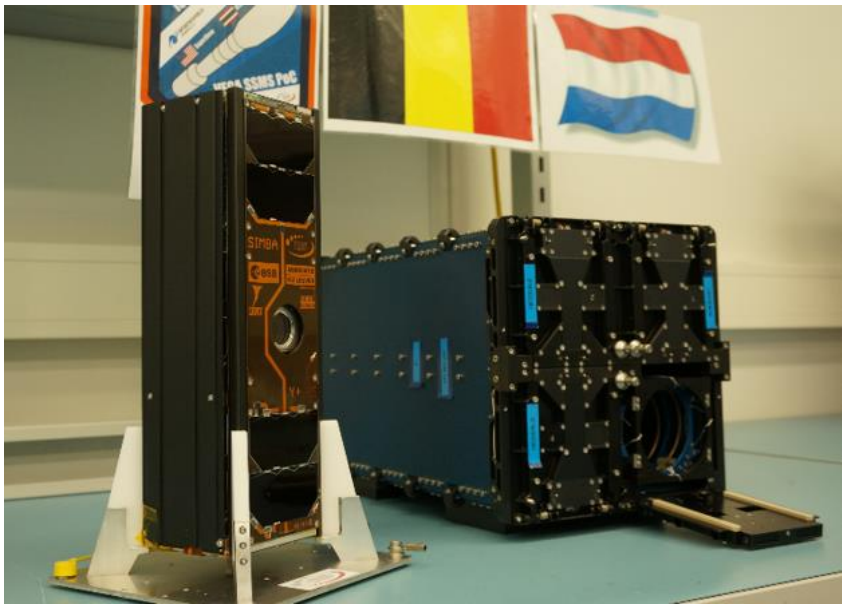

Figure 30: SIMBA just after the final preparations for launch. To the right, we see t a launch container with room for 4 satellites, one of which will serve for SIMBA. The door is open for integration of SIMBA.

The SIMBA mission will hopefully demonstrate that CubeSats can be used as full-fledged scientific instruments. The cost reduction compared to full-size satellite platforms would allow for multiple versions of these instruments to be built and flown in the future, gaining unprecedented ground coverage. This would be a huge step forward in measuring the radiation balance - one of the most important parameters of climate change.

SIMBA follow-on mission to retrieve the Earth's energy imbalance from space - Next to the launch of the SIMBA CubeSat in September 2020, a possible follow-on mission has also started to be investigated. Like SIMBA, the goal of this mission will be to retrieve the Earth's energy imbalance.

A 6U (6 units) CubeSat is the baseline with one unit allocated to each instrument. The first instrument is an improved version of SIMBA's radiometer. This radiometer will observe both the incoming Solar radiation and the Earth's total outgoing radiation, featuring a wide field of view (WFOV) of 135° to observe the Earth from limb to limb. To increase its accuracy with respect to SIMBA's radiometer, the new instrument will feature a shutter to avoid the so-called thermal drift that occurs in space-based WFOV radiometers. Moreover, the CubeSat will carry two identical radiometers, the second being used to characterize the ageing of the first radiometer.

To increase the spatial resolution up to a few kilometers, enabling scene identification as well as the distinction between the reflected solar radiation (shortwave) and the Earth's emitted thermal radiation (longwave), the radiometer will be supplemented by two WFOV (140°) imagers: the shortwave camera, operating between 400 and 1100 nm, and the longwave camera, with a spectral range in the thermal infrared between 8 and 14 µm (Figure 31).

This work is the topic of a PhD thesis in collaboration with the Department of Applied Physics and Photonics of the Vrije Universiteit Brussel. This research led to several publications and oral presentations in 2020.

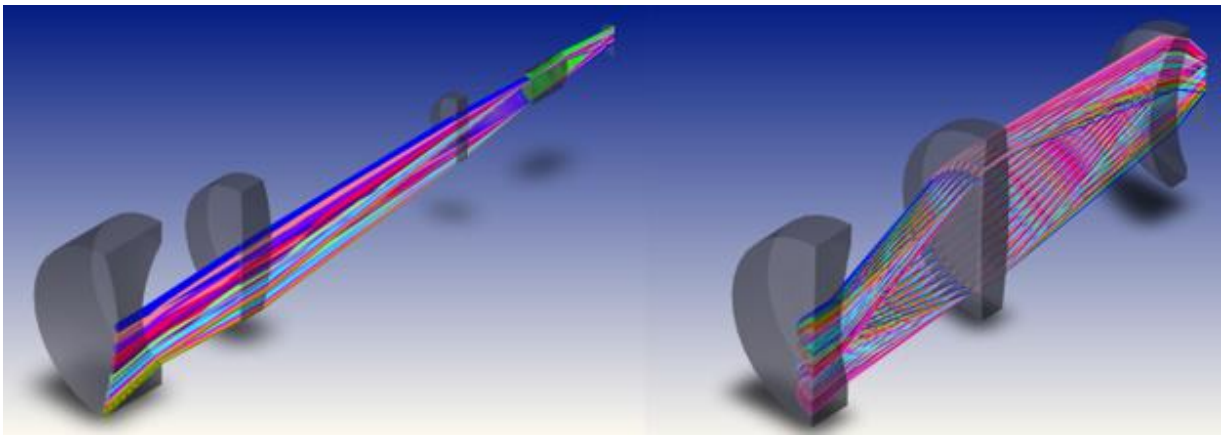

Figure 31: Half-views of the optical designs of the shortwave (left) and longwave (right) cameras.

First results of the SLP instrument on board PICASSO

The Sweeping Langmuir Probe (SLP) instrument on board the Pico-Satellite for Atmospheric and Space Science Observations (PICASSO) has been fully developed at BISA with substantial STCE support. PICASSO, an ESA in-orbit demonstrator launched in September 2020, is a triple unit CubeSat orbiting at about 540 km altitude with 97 degrees inclination. SLP comprises four small cylindrical probes mounted at the tip of the solar panels. The measurement principle is based on the conventional Langmuir probe theory, i.e. by sweeping the potential of one probe with respect to the plasma potential and measuring the current collected, the instrument acquires a current-voltage (I-V) characteristic from which several plasma parameters are retrieved: the electron density and temperature, the ion density, and the S/C (spacecraft) potential.

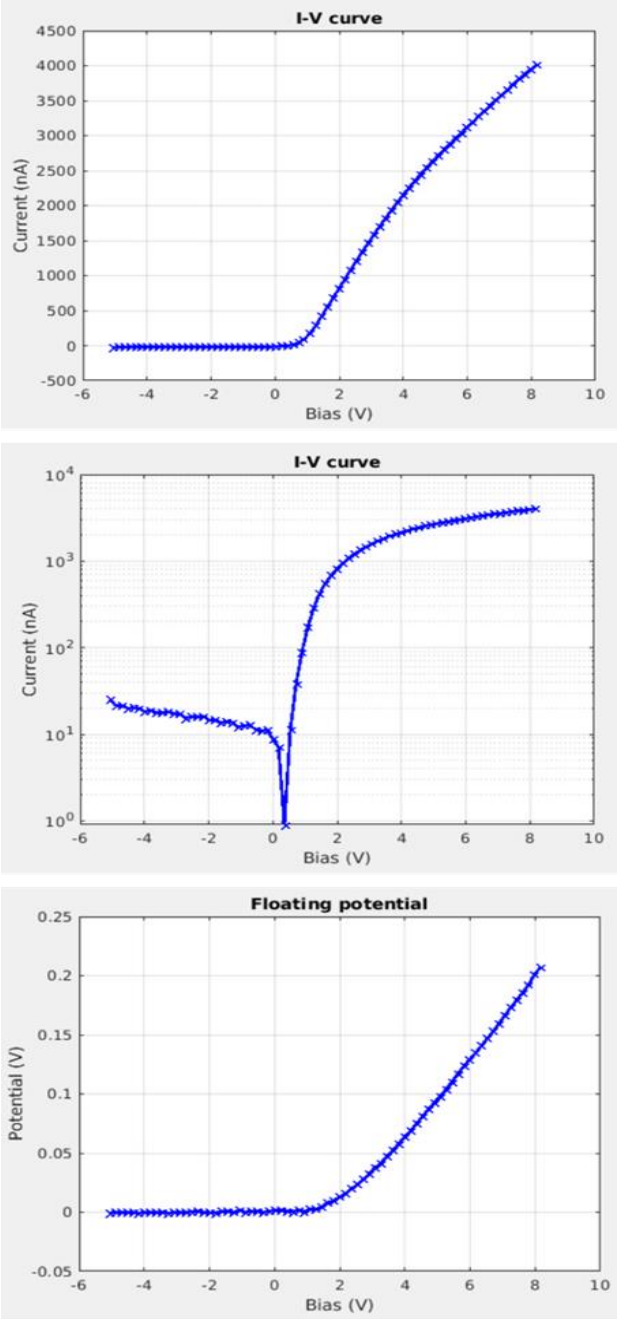

Figure 32: The current-voltage characteristic on resp. a linear (top) and semi-log scale (middle) as measured with SLP during commissioning. The graph at the bottom represents the floating potential with respect to the S/C potential, again as measured with SLP during commissioning.

The measurement principle of Langmuir probe instruments is relatively simple but the accurate computation of the plasma parameters is a much more challenging task because of many possible biases. Those biases are not only due to the imperfections of the instrument, but also arise from the complex coupling between the probes, the plasma and the spacecraft. Since for PICASSO the spacecraft surface area to probe area ratio is smaller than 1000, the potential of the spacecraft will be affected by the operation of SLP. When the probes are biased positively with respect to the plasma potential, the current of electrons collected by the probe cannot be fully compensated for by the collection of positive ions on the spacecraft surface. Therefore, the potential of the spacecraft decreases as the probe bias increases, which can lead to inaccurate results if not taken into account. For this reason, while the bias of one probe is swept to acquire the I-V characteristic, another probe measures the floating potential with respect to the spacecraft potential. This way, the charging of the spacecraft can be quantified and accounted for in the data processing.

The I-V (current-voltage) characteristic depicted in Figure 32 (linear scale ; top - semi-log scale ; middle) is one of the first sweeps measured by SLP in space during the commissioning of the instrument. The data are clean and the curve shapes are as expected for this plasma environment, which is very promising.

It can be seen in the bottom graph of Figure 32 that the spacecraft potential is affected by the operation of SLP when the probe is biased positively, as expected. The very low noise level on the potential measurement shown in this figure is very encouraging.

A space anemometer for the lower thermosphere: the Cross-track Wind Sensor

The upper atmosphere of the Earth (including the lower thermosphere and ionosphere region or "LTI" between about 100 and 200 km altitude) is the gate towards space. The LTI is the interface between the rarefied partially ionized layers of the atmosphere, which is still gravitationally bound to the Earth, and the inner layers of the magnetosphere, which makes up the mainly ionized environment of Earth in space and is dominated by the interplay between the Earth's magnetic field and the interplanetary magnetic field.

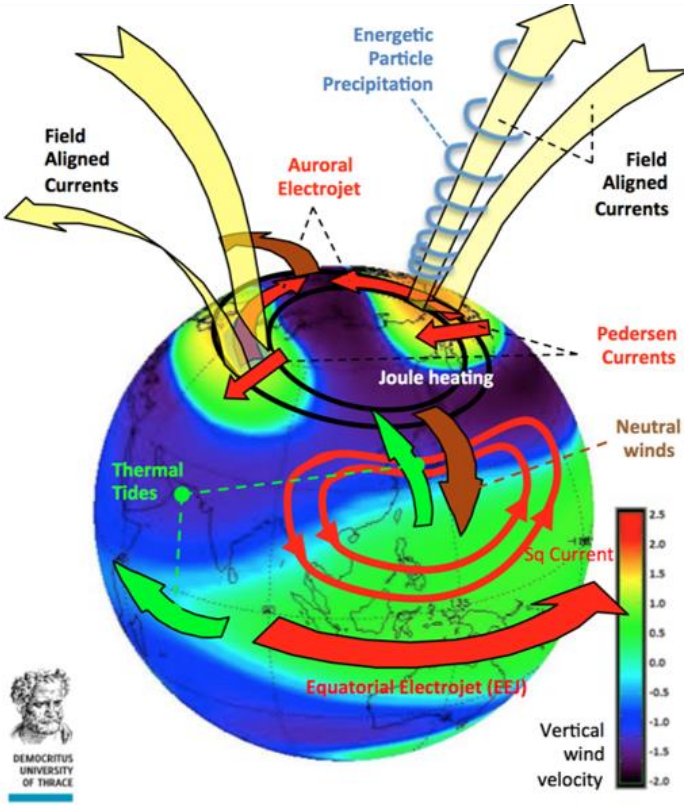

Figure 33: A summary sketch of the main physical processes in the lower thermosphere and ionosphere (from Sarris et al., 2020).

This interface region is subject to a continuous and intense forcing from above and below, as illustrated in Figure 33. The forcing from above is mainly due to phenomena driven by the Sun and the solar wind, while the forcing from below is mainly due to atmospheric gravity waves, planetary waves and tides (Sarris et al., 2020). Although not too high above the Earth, the LTI is one of the least understood regions, and therefore sometimes jokingly called the "ignorosphere". Nevertheless, it is at the heart of many space weather phenomena. This lack of knowledge is mainly due to the virtual inaccessibility of the region for in-situ investigation. Indeed, on the one hand, it is too low for systematic research by satellites because the atmospheric drag is too high so any spacecraft there would fall down rapidly, and on the other hand it is too high for study by balloons. The sparse data available come from occasional (suborbital) rocket campaigns.

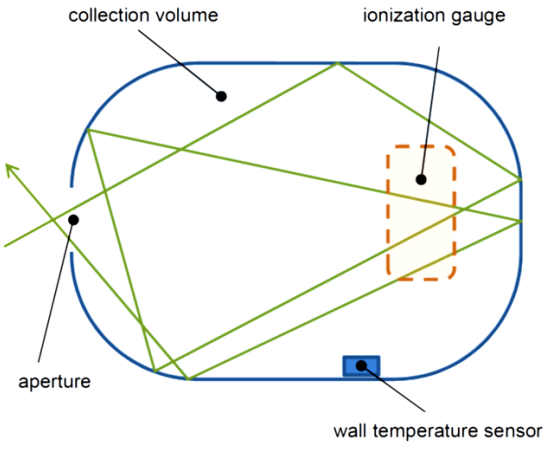

Figure 34: The CWS instrument concept.

Recently, the European Space Agency renewed its interest in this region and investigated the possibility to build a spacecraft mission to this region based on the concept of repeatedly diving down into the LTI rather than trying to stay in the LTI continuously for an extended time. The project, titled Daedalus, although not yet selected for launch, raised interesting scientific questions and challenges. The STCE and the Royal Belgian Institute for Space Aeronomy (BISA) took part in this project and looked

into providing a conceptual design of a space anemometer, an instrument able to measure the velocity of the neutral wind in the LTI.

The development of a Cross-track Wind Sensor (CWS) to measure cross-track neutral wind speeds at atmospheric altitudes going down to about 120 km in the Earth's atmosphere on board the Daedalus spacecraft, was part of a Phase 0 study coordinated by Thales Alenia Espace with BISA as a subcontractor. Another instrument would measure the ram neutral wind speed. The design allows measurement of the cross-track velocity in the range ± 2000 m/s, with a cadence of 1 Hz. The operating principle is based on the concept of pressure equilibrium between two media, one that is moving and thus has thermal and ram pressure, and one that is not moving and thus has only static pressure. The particular merit of the concept is that it works with collisionless or slightly collisional media. The concept is illustrated in Figure 34.

The first component is a measurement volume, which has a given opening or aperture as illustrated in Figure 34. A neutral gas particle that enters the volume through the aperture hits the walls repeatedly. Upon collision with the walls, the particle loses energy until it has acquired a kinetic energy that corresponds to the wall temperature or until it leaves the volume through the opening again. The thermal + ram pressure of the incoming gas is thus converted to a purely thermal static pressure inside the collector volume. The second component is an ionization gauge that is able to measure the density inside the collector volume. The third component is a temperature sensor that determines the temperature of the inner wall of the collector volume.

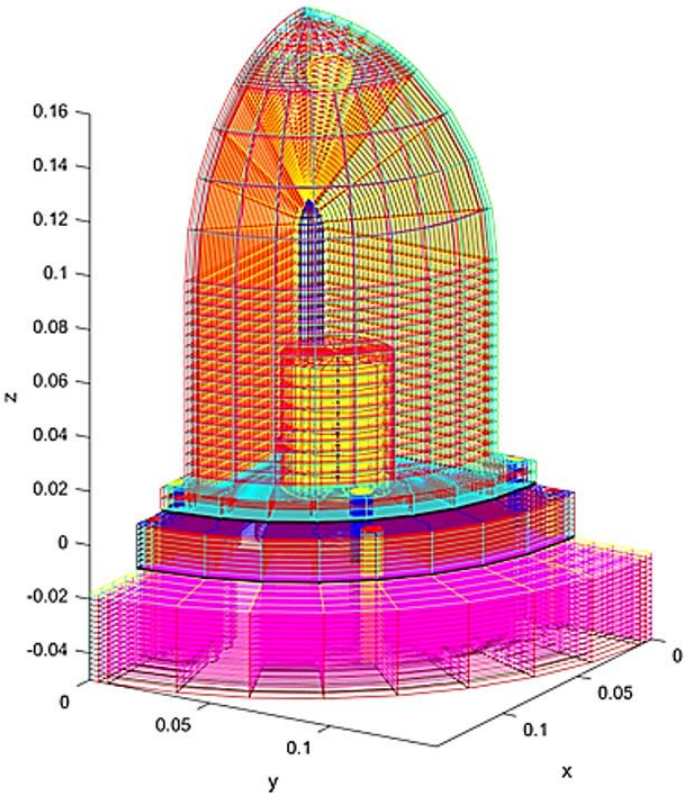

Figure 35: Wire frame model of (a quarter of) the CWS detector unit including outer wall, aperture, base plate, gauge, attachment screws, and part of the spacecraft chassis .

The CWS instrument consists of four collection volumes as the one illustrated in Figure 35, with tilted openings, arranged symmetrically in two perpendicular pairs on the front face of the spacecraft. By analysis of the pressure or density differences between each pair, it is then possible to compute the cross-track components of the neutral wind. This concept is akin to that of the Coupled Ion-Neutral Dynamics Investigation (CINDI) instrument (Hanson et al., 1992) on board NASA's C/NOFS spacecraft (Communications/Navigation Outage Forecasting System). However, C/NOFS operated above 400 km altitude, thus avoiding the challenges of the interaction with the denser LTI below 150 km.

The conceptual design included the building of a model for the measurement and data analysis logic. It was also necessary to demonstrate that the instrument could work in the harsh conditions encountered

at low altitudes, below 150 km where the friction with the upper atmospheric layers heats the instrument. A numerical model of CWS was constructed and "launched" into the anticipated Daedalus orbit, thus periodically experiencing heating near perigee (at 125 km). The thermal model confirmed that, with some specific precaution measures, the CWS can perform as intended. At the same time, laboratory tests were performed to investigate different solutions for the ion gauge necessary to measure the static pressure inside the instrument.

This activity opened a new field of research for the BISA team, unique in its kind in Europe. Unfortunately, in February 2021, ESA selected another mission to go forward to Phase-A for further design consolidation and feasibility assessment, and so the Daedalus mission was not selected. The science team is now looking into alternatives.

Establishing the radiation pattern of the BRAMS transmitter using a weather balloon

Measuring the radiation pattern of the BRAMS transmitter - In support of our BRAMS (Belgian RAdio Meteor Stations) network to detect meteors above Belgium using radio waves, the transmitter located in Dourbes has been emitting a pure continuous sine wave towards the zenith at a frequency of 49.97 MHz since 2010. The antenna is made of 2 crossed dipoles and a ground plane made of an 8m × 8m metallic grid with the aim of emitting a circularly polarized wave in an isotropic way around the zenith. Due to inadequate adaptation of the two antennas, the radiation pattern was unfortunately very different from the theoretically expected one and in-situ measurements were necessary to determine the exact amount of power transmitted in each direction. Knowing this radiation pattern is essential for many studies using BRAMS data.

Figure 36: (left) Experiment carried out in December 2019 with the captive weather balloon above the 8m x 8m BRAMS transmitter in Dourbes. (right) The payload platform connected to the two short dipole antennas located below the helium-filled weather balloon. Three ropes are used to keep the balloon in its intended position.

A captive weather balloon with a payload platform - In the course of 2019, a payload was designed to measure in-situ the radiation pattern of the transmitter. It comprises a pair of SDR (Software Defined Radio) receivers located on a platform and connected to two short dipole antennas in order to measure

both polarized components. The non-conducting platform was hung below a captive weather balloon filled with helium. Due to the proximity of the platform, the transmitter was only operating at a small fraction of its nominal power. The platform hosted a webcam, a three-axis accelerometer, and a three-axis magnetometer to determine its position and attitude with sufficient accuracy. A battery and a Raspberry Pi (mini-computer) controlled remotely from the ground completed the payload.

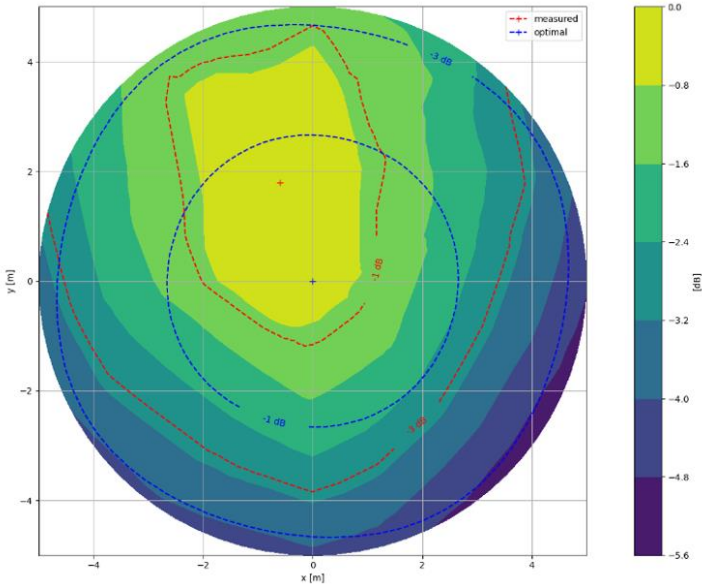

Figure 37: This gain map (relative to peak gain) shows the total gain of the BRAMS transmitter before it was modified. The blue dotted circles show the expected contours for the optimal situation with perfect adaptation and a fully circularly polarized signal. The red dotted curves are the real measurements. The beam maximum is off-centre with a tilt of 11.5° down from zenith and towards an azimuth of 339°. It is more elongated in the direction of the tilt.

Discrepancies between the expected and measured radiation patterns - In December 2019, the radiation pattern was sampled in a single horizontal plane, 10 meters above the transmitter. Images taken by the on-board camera had to be used to determine the platform's position. The orientation of the platform was calculated using data from the accelerometer, magnetometer and camera images.

The radiation power pattern of the transmitter for elevations greater than 60° was computed and compared to the optimal radiation pattern of the transmitter (assuming ideal match and 90° phase difference at the feed points). The discrepancies between the two patterns are significant, most notably with a maximum pointing 10° westwards and a severe departure from the intended circular polarization. Figure 37 shows the measured total antenna gain.

Upgrade of the BRAMS transmitter - The transmitter was upgraded in June 2020 to correct this behaviour. The old antenna and the splitter have been replaced. The power amplifier has also been increased to 130 W. The new radiation pattern will be measured again to confirm the circular polarization. Some improvements for the balloon-borne payload are planned to reduce the dwell time at each position, allowing more measurements to be performed, even if there is some wind.

Laboratory facilities for matrix detectors characterization

BISA has a long-standing experience in the development and the characterization of payloads for space projects, namely for solar physics, planetology and atmospheric studies (SOLAR/SOLSPEC, SOIR, NOMAD, ALTIUS). Spectroradiometers and spectro-imagers are used to study solar disk features or to investigate the composition of planetary atmospheres and their trace constituents. Apart from the design and the integration of a space experiment, there are mandatory steps for the characterization of sub-systems and at the end, for the whole instrument. Indeed, there is a need to validate the opto-mechanical concept by testing, or to space qualify sub-systems, and characterize the instrument radiometrically, and finally to perform environmental qualification tests. At the instrument and detector level, measurement equations

and transfer functions are used to convert raw electronic signals into meaningful and useful scientific data. Typical parameters for an array detector that figure in these equations, such as QE (Quantum Efficiency), latency effects, temperature dependencies or inter-pixel response variability, must be derived.

The radiometric laboratory of BISA has been involved in 2020 in the electro-optical characterization of matrix detectors for two space projects: MAJIS/JUICE and ALTIUS. For that purpose, dedicated facilities were developed to cover the required spectral range, temperature, and space environment conditions. An overview of these campaigns is presented here.

Figure 38: General view of the MAJIS VIS-NIR thermal-vacuum facility.

MAJIS (Moons And Jupiter Imaging Spectrometer) is part of the science payload of the ESA L-Class mission JUICE (Jupiter ICy Moons Explorer) to be launched in 2022 with an arrival at Jupiter in 2031. JUICE will perform, for at least three years, detailed observations of the Jovian system that includes Jupiter itself and three of its four Galilean moons, i.e. Europa, Ganymede and Callisto. MAJIS uses two channels (VIS-NIR and IR: visual - near-infrared and infrared) for spectral imaging of atmospheric and surface features. BISA and ROB received the responsibility to characterize the valuable FM (Flight Model) array detector of the MAJIS VIS-NIR channel, under the supervision of the CNES (Centre National d'Etudes Spatiales, France), IAS (Institut d'Astrophysique Spatiale, France) and with the support of BELSPO and ESA (PRODEX Office). BISA developed the VIS-NIR thermal-vacuum facility (vacuum chamber, cryo-cooling system), including the high-level security system to protect the detector, the software for operations and the optical equipment to deliver calibrated photon flux on the detector. The full FM characterization campaign took place during the summer of 2020. The facility met the requirements for the high level of cleanliness

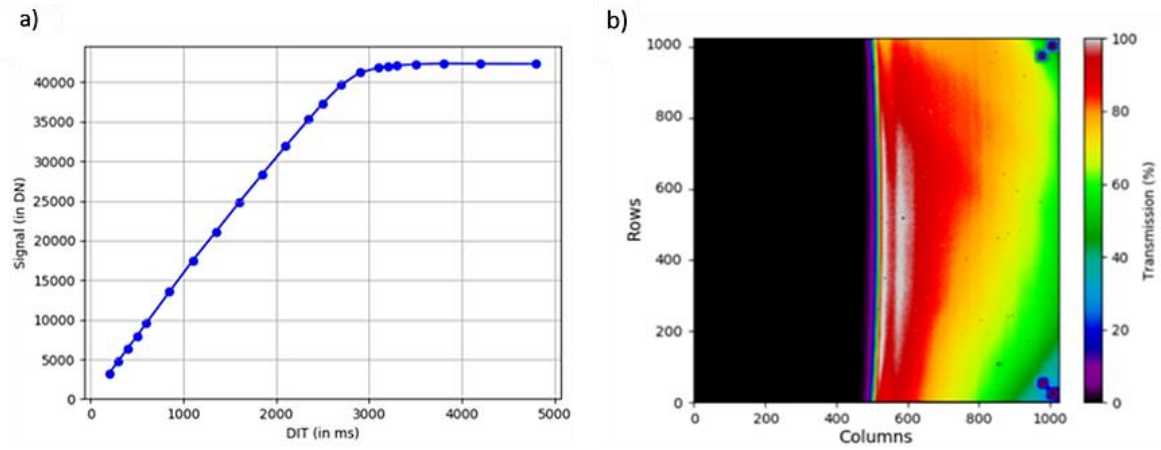

Figure 39: MAJIS VIS-NIR detector. Example of characterization results: a) for linearity, b) LVF (Linear Variable Filter) alignment verification.

and the temperature range (between -157 °C to -120 °C). Figure 39 shows an example of results for linearity measurements and a linear (high-pass) filter alignment verification in front of the detector.

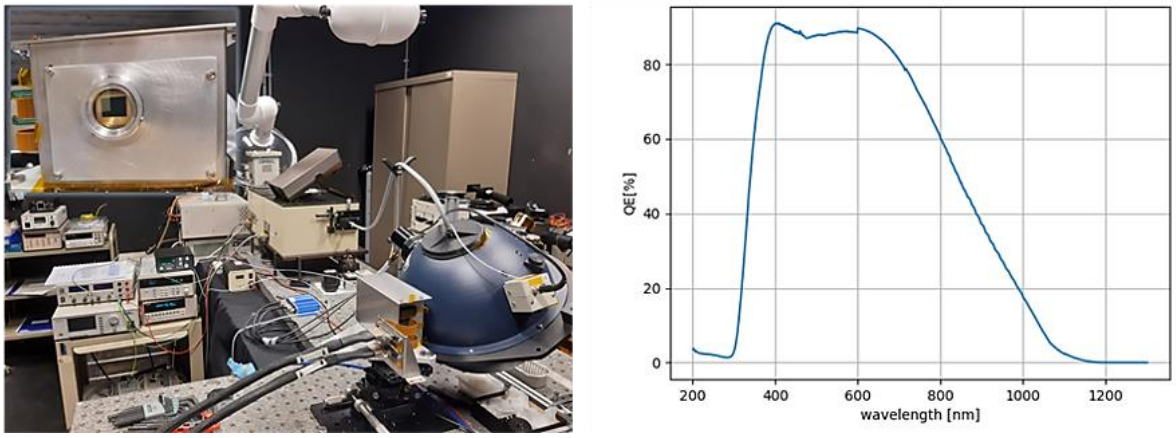

Figure 40: (left) General view of the facility used for QE measurements for the UV and VIS detectors of ALTIUS; a detail of the VIS detector is seen on the insert. (right) Result of the QE measured for the VIS detector.

ALTIUS (Atmospheric Limb Tracker for Investigation of the Upcoming Stratosphere) is an Earth observation mission for atmospheric sounding, for which the objective is the high-resolution monitoring of the ozone distribution and other trace gases in the upper atmosphere. The ALTIUS instrument is composed of three spectral channels, UV (ultraviolet), VIS and NIR. BISA had to verify the QE of the prototype array detectors for the UV and VIS channels. It was performed using a facility similar to MAJIS, although at standard laboratory conditions, composed of a tunable monochromatic light beam, integrating sphere and absolute calibrated photodiodes. Figure 40 shows an ensemble picture of the facility as well as the results of the experimentally derived QE curve of the VIS detector.

Thanks to the success of the MAJIS project and the new facilities set up for ALTIUS, plans are to further develop the laboratory for extended activities regarding the characterization of ground-based and space instruments and detectors over a wide range of radiometric parameters. The spectral range will cover the vacuum UV to NIR.

Life during COVID-19 - Credits: El Arroyo

Applications, modeling and services

PROBA 2 data for the complete mission updated

In June 2020, the PROBA2 team reached another milestone in the mission's lifetime. After having celebrated the 10th anniversary of the launch of the satellite in 2019, we completed a full reprocessing of all data from this successful mission in 2020. PROBA2 is a micro-satellite that was launched in 2009 and

	Number of files	Amount of data
SWAP level 0 files	> 2 662 000	> 5.2 T
SWAP level 1 files	> 2 411 000	> 4.7 T
SWAP movies	> 11 000	> 245 G
LYRA level 1 files	> 26 000	> 335 G
LYRA level 2&3 files	> 8000	> 305 G

Figure 41: Table showing the amount of data collected by the LYRA and SWAP instruments onboard PROBA2, as well as the derived products, measured at the time of writing, in April 2021.

that carries 2 solar instruments for which the Royal Observatory of Belgium holds the principal investigator responsibility: LYRA, the Large Yield Radiometer measures the solar ultraviolet irradiance in 4 wavelengths, and SWAP, the Sun Watcher using Active Pixel System detector and Image Processing, takes pictures of the solar corona in ultraviolet. Both instruments are important assets for the space weather services of the Royal Observatory: They keep a close and continuous eye on the solar activity.

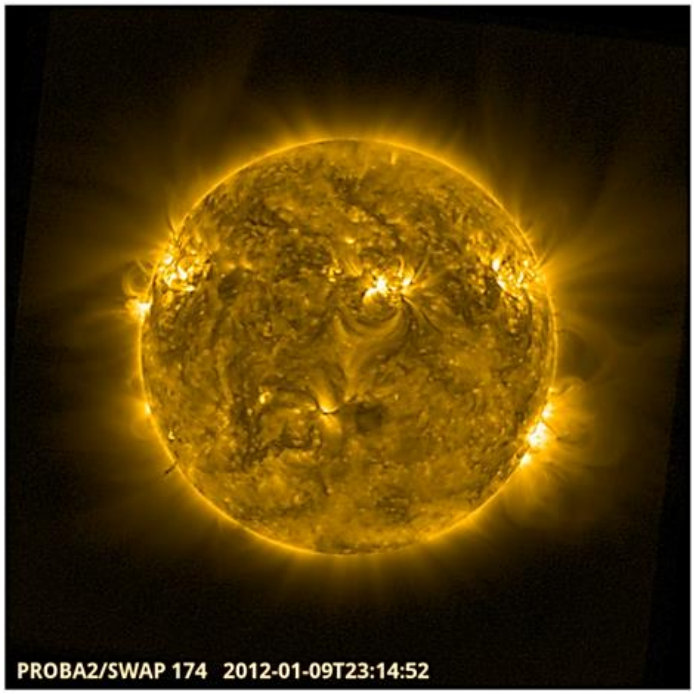

Figure 42: A reprocessed and stacked SWAP image picturing the active solar corona at 174 nm. The stacking of several SWAP images, taken closely together in time, allows us to bring out the faint features in the outer corona.

In 2017, we embarked on the massive project of reprocessing our complete data set, which contains over 10 years of SWAP images and LYRA measurements (Figure 41). This reprocessing served two purposes. First of all, it allowed us to update all data files to the latest calibration. Indeed, our understanding of the instruments evolves continuously and also the performance of the instruments themselves changes over time (for example due to degradation or faulty pixels). The PROBA2 team therefore continuously works on improving the LYRA and SWAP data: The calibration routines for both instruments are updated regularly, and the latest version

is always available, for example through IDL SolarSoft. However, the higher-level data provided through our website and through the SolarSoft IDL routines has been processed with the version of the calibration software that was available at the time of acquisition or processing. Therefore, the most recent improvements were not included in older files. The newly reprocessed data is now calibrated according to our most recent understanding of the instruments. An example image taken by SWAP is shown in Figure 42.

The second purpose of the reprocessing was a major update of the hardware and software that is used to produce all types of PROBA2 data (various levels of fits files, quicklook images, movies, etc.). One of the main goals was to get rid of deprecated functions used in the software. The core of the PROBA2 software was written before the launch of the satellite and is thus over 10 years old. Updating the software while at the same time keeping the system running to process incoming data is not always evident. So, for the reprocessing we recreated the complete PROBA2 system on new servers (shown in Figure 43), updated all software there, and first ran thorough tests. We then performed the reprocessing on the new hardware and once that was finished, we migrated also the operational tasks to this new server and continued from there.

Figure 43: The old servers used for the PROBA2 pipeline. After 10 years of continuous use, this hardware needed to be replaced by newer servers.

This transfer to the new servers was performed in June 2020. Due to the measures taken to manage the COVID-19 pandemic, this was not easy to coordinate. Only a few of the PROBA2 colleagues were allowed on site together, but after a very long working day the migration was complete and the PROBA2 pipelines were up and running again, with the newly calibrated data online. Afterwards also the remote archive at the ESAC facility in Spain was updated with the newest data.

Horizon 2020 project concluded: TechTIDE - Warning and Mitigation Technologies for Travelling Ionospheric Disturbances Effects

Travelling Ionospheric Disturbances (TIDs) are waves in the ionospheric plasma, exhibiting a wide range of amplitudes, periods, and propagation velocities. These disturbances pose a threat to the various technologies that are using radio signals propagating through the ionosphere, as such signals might experience unexpected dispersion, reflection, absorption, or Doppler shift. Affected systems include for instance satellite navigation, HF communication and direction finding, and radio astronomical observations.

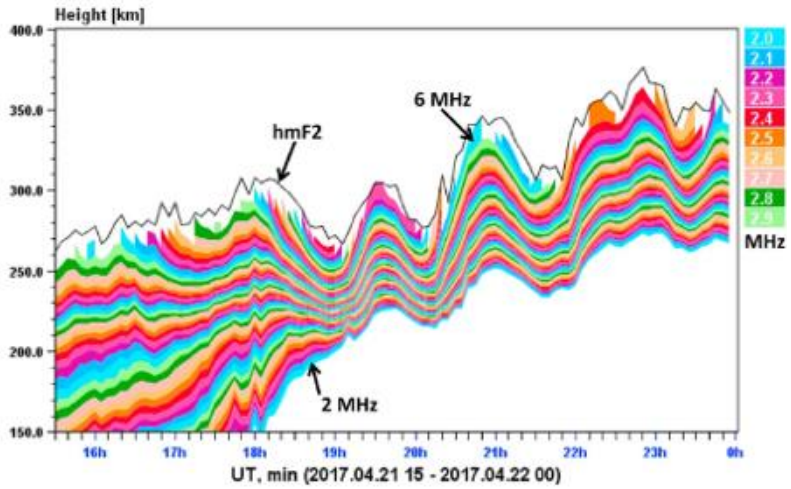

Figure 44: Wave-like disturbance in the ionospheric plasma density contours, here detected by the ionosonde in Roquetes, Spain. Note that the contours indicate plasma frequency, which is directly related to electron density. Note that there are many more measured frequencies than that there are colours, so the colour codes repeat themselves after several values of the frequencies.

Small-scale TIDs are almost permanently present in the ionosphere, while more significant disturbances are occasionally produced from different sources. Causes for the medium-scale TIDs include tropospheric and stratospheric phenomena, as well as seismic and volcanic events or even large anthropogenic explosions. The largest TIDs originate usually from the auroral regions as a result of external disturbances, which are ultimately driven by solar events such as CMEs.

Because of their impact on the various technologies, monitoring the TID activity in real-time is highly sought after, but due to the wide range of periods, amplitudes etc. this is difficult to achieve. Various monitoring techniques exists, and each method has a certain range in which it can detect TIDs and determine their characteristics. But no single method exists that can detect the whole range of important disturbances. For this reason, the Horizon 2020 project TechTIDE combines various observational methods and associated models together in order to comprehensively monitor the full spectrum of TIDs over Europe. This project started in 2017 and finished in July 2020, with the final release of both a web-portal user interface and an open access API (application programming interface) providing access to the monitoring and warning system (available via the project website http://www.tech-tide.eu/).

Within the framework of this project, the large-scale TIDs are detected using GNSS receiver data, medium scale disturbances are monitored using vertical and oblique ionosonde soundings, and at the smallest detectable scales data are provided by continuous Doppler sounding systems. Our main contribution to this project is based on the exploitation of the Dourbes ionosonde data (https://digisonde.oma.be/).

Besides the use of routine, vertical incidence ionosonde observations, it has been demonstrated in earlier work that the oblique sounding mode -in which one ionosonde receives transmissions from a distant, synchronized one- provides a good way of detecting TIDs. However, this requires ionosondes to be synchronized using suitable sounding schedules and a well-designed network topology of transmitters and receivers. For this purpose, the

Figure 45: The final operational network of oblique ionosonde soundings for TID detections in western Europe. Thicker arrows indicate higher cadence of transmissions.

ionosonde in Dourbes is ideally situated, as its central location in Europe allows simultaneous transmissions to receivers located throughout the continent. During this project, it has been demonstrated that the oblique sounding network that was set up can indeed be used to detect TIDs and determine various characteristics such as amplitude, period, speed and direction of propagations, in near real time.

Although the project has formally ended, the consortium members have agreed to continue the operational monitoring of TIDs over Europe on a best effort basis. The hope is to transition from the pilot system developed during the project to a permanent, operational TID warning service.

Algorithms improvement on Automatic Lidar and Ceilometer (ALC) data for weather forecasting support

Fog forecasting improvement - Radiation fog is the most frequent cause of surface visibility below 1 km, and is one of the most common and persistent weather hazards encountered in aviation and to nearly all forms of surface transport. Forecasting radiation fog can be difficult, a number of approaches have been used to integrate the satellite data, numerical modeling and standard surface observations. These approaches lack generally the vertical and temporal resolution, representation of boundary layer and microphysical processes. They typically do not represent accurately the activation processes of fog droplets that depend on the chemical and physical properties of the aerosols.

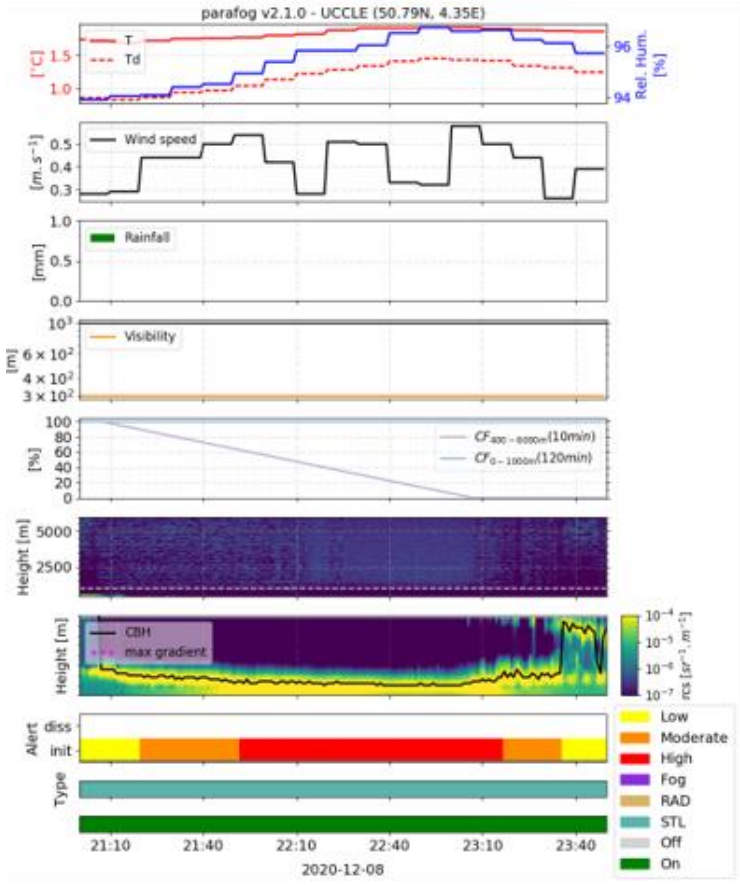

Figure 46: View interface of the new PARAFOG version applied on the ALC data of Uccle.

In 2016, a forward stepwise screening algorithm (PARAFOG) was developed (Haeffelin et al., 2016) based on the monitoring of the hydroscopic growth process (inducing fog formation) through the attenuated backscatter signal measured by ALC. This algorithm was developed under a collaboration between RMI and the Site Instrumental de Recherche par Télédéction Atmosphérique (IPSL, Institut Pierre-Simon Laplace) with the ALC dataset of RMI. It is experimentally used at Roisy-Charles de Gaulle and Orly airports where it provides valuable information supporting the decision making of both weather forecasters and air traffic controllers that affect scheduling of airplanes. Several years of experience with PARAFOG have highlighted some limitations, such as

the monitoring of stratus lowering fogs, its capabilities to monitor the entire fog life cycle, or even its anticipation for shallow radiation fog events near the surface.

In 2020, a new version of PARAFOG (Figure 46) which is an improved and extended version (by IPSL) of the first version allowing to discriminate between radiation and stratus-lowering fog formation was implemented on the ALC of RMI in real-time to support its evaluation.

MLH retrieval algorithm improvement - The ALC also offers the opportunity to monitor the vertical profile of aerosols and the mixing layer height (MLH) on a continuous temporal scale. The knowledge of MLH can improve the forecasting of the dispersion of trace gases and aerosols in the lowest layers of the atmosphere and can also improve the accuracy of the greenhouse gas concentration budgets highly depending on MLH.

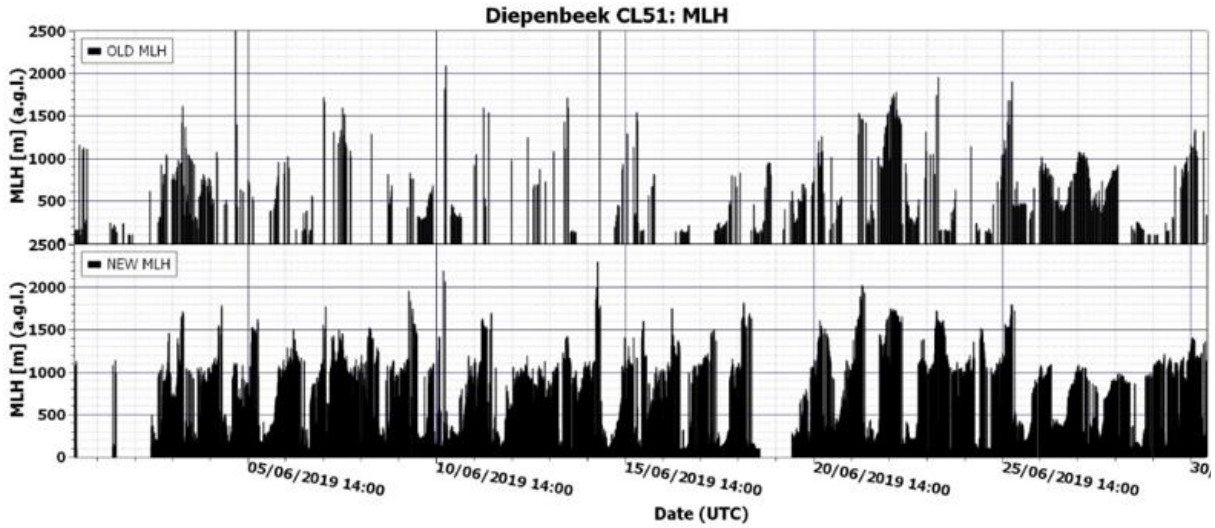

Figure 47: MLH comparison between the old and the new algorithm on June 2019 with the ALC dataset of Diepenbeek.

In 2012, RMI developed an algorithm to retrieve the MLH from the ALC measurements. Unfortunately, if some criteria were not met, the algorithm did not calculate any MLH which created temporal discontinuities in the dataset. In 2020, a new algorithm was developed incorporating the latest developments in the field in order to obtain a continuous temporal series essential for data assimilation. Figure 47 shows an example of a comparison between the old and the new algorithm which better highlights the diurnal cycle of the MLH.

Life during COVID-19 - Credits: El Arroyo

Publications

This overview of publications consists of three lists: the peer-reviewed articles, the presentations and posters at conferences, and the public outreach talks and publications for the general public. It does not include non-refereed articles, press releases, the daily, weekly and monthly bulletins that are part of our public services,… These data are available at the STCE-website or upon request.

Authors belonging to the STCE have been highlighted in the list of peer reviewed articles.

Peer reviewed articles

1. Aminalragia-Giamini, S.; Jiggens, P.; Anastasiadis, A.; Sandberg, I.; Aran, A.; Vainio, R.; Papadimitriou, C.; Papaioannou, A.; Tsigkanos, A.; Paouris, E.; Vasalos, G.; Paassilta, M.; **Dierckxsens, M.**
Prediction of Solar Proton Event Fluence spectra from their Peak flux spectra
Journal of Space Weather and Space Climate, 10, 1, 2020, DOI: 10.1051/swsc/2019043

2. Auchère, F.; Andretta, V.; Antonucci, E.; … ; **Berghmans, D.; Mampaey, B.; Parenti, S.; Verbeeck, C.; Zhukov, A.N.**; … and 65 co-authors
Coordination Within the Remote Sensing Payload on the Solar Orbiter Mission
Astronomy & Astrophysics, 642, A6, 2020, DOI: 10.1051/0004-6361/201937032

3. Aun, M.; Lakkala, K.; Sanchez, R.; Asmi, E.; Nollas, F.; Meinander, O.; Sogacheva, L.; **De Bock, V.**; Arola, A.; de Leeuw, G.; Aaltonen, V.; **Bolsée, D.**; Cizkova, K.; **Mangold, A.**; Metelka, L.; Jakobson, E.; Svendby, T.; **Gillotay, D.; Van Opstal, B.**
Solar UV radiation measurements in Marambio, Antarctica, during years 2017–2019
Atmospheric Chemistry and Physics, 20, 6037-6054, 2020, DOI: 10.5194/acp-20-6037-2020

4. Bandic, M.; Verbanac, G.; **Pierrard, V.**
Relationship between global plasmapause characteristics and plasmapause structures in the frame of interchange instability mechanism
Journal of Geophysical Research: Space Physics, 125, 2, 2020, DOI: 10.1029/2019JA026768

5. Barnes, D.; Davies, J.; Harrison, R.; Byrne, J.; Perry, C.; Bothmer, V.; Eastwood, J.; Gallagher, P.; Kilpua, E.; Moestl, C.; **Rodriguez, L.**; Rouillard, A.; Odstrcil, D.
CMEs in the Heliosphere: III. A Statistical Analysis of the Kinematic Properties Derived from *Stereoscopic Geometrical Modelling Techniques Applied to CMEs Detected in the Heliosphere from 2008 to 2014 by STEREO/HI-1*
Solar Physics, 295, 11, 150, 2020, DOI: 10.1007/s11207-020-01717-w

6. Belehaki, A.; Tsagouri, I.; Altadill, D.; Blanch, E.; Borries, C.; Buresova, D.; Chum, J.; Galkin, I.; Juan, J.M.; Segarra, A.; Timoté, C.C.; Tziotziou, K.; **Verhulst, T.G.W.**; Watermann, J.
An overview of methodologies for real-time detection, characterisation and tracking of traveling ionospheric disturbances developed in the TechTIDE project
Journal of Space Weather and Space Climate, 10, A42, 2020, DOI: 10.1051/swsc/2020043

7. **Bertrand, B.; Defraigne, P.**
Fundamental physics tests using the propagation of GNSS signals
Advances in Space Reasearch, 66, 12, 2764-2772, 2020, DOI: 10.1016/j.asr.2020.06.033

8. **Bolsée, D.; Van Laeken, L.;** Cisneros-González, M.E.; **Pereira, N.; Depiesse, C.; Jacobs, L.; Vandaele, A.C.; Ritter, B.; Gissot, S.; Karatekin, O.**; Poulet, F.; Langevin, Y.; Dumesnil, C.; Dubois, J.-P.; Arondel, A.; Haffoud, P.; Ketchazo, C.; Hervier, V.
Characterization facility for the MAJIS/JUICE VIS-NIR FM and SM detectors
SPIE 2020, Space Telescopes and Instrumentation 2020: Optical, Infrared, and Millimeter Wave, Proceedings Volume 11443, 114437H, 2020, DOI: 10.1117/12.2576319

9. **Brenot, H.**; Rohm, W.; Kačmařík, M.; Möller, G.; Sá, A.; Tondaś, D.; Rapant, L.; Biondi, R.; Manning, T.; Champollion, C.
Cross-Comparison and Methodological Improvement in GPS Tomography
Remote Sensing, 12, 30, 2020, DOI: https://doi.org/10.3390/rs12010030

10. Caspi, A.; Seaton, D.B.; Tsang, C.C.C.; … ; **West, M.J.**; … ; **Zhukov, A.N.** and 25 co-authors
A New Facility for Airborne Solar Astronomy: NASA's WB-57 at the 2017 Total Solar Eclipse
The Astrophysical Journal, 895, 2, 131, 2020, DOI: 10.3847/1538-4357/ab89a8

11. Cécere, M.; Sieyra, M.V.; Cremades, H.; **Mierla, M.**; Sahade, A.; Stenborg, G.; Costa, A.; **West, M.J.; D'Huys, E.**
Large non-radial propagation of a coronal mass ejection on 2011 January 24
Advances in Space Research, 65, 6, 1654-1662, 2020, DOI: 10.1016/j.asr.2019.08.043

12. Cisneros-González, M.E.; **Bolsée, D.; Pereira, N.; Van Laeken, L.; Depiesse, C.; Jacobs, L.; Robert, S.; Vandaele, A.C.; Gissot, S.; Karatekin, O.**; … and 9 co-authors
MAJIS/JUICE VIS-NIR FM and SM detectors characterization
SPIE 2020, Space Telescopes and Instrumentation 2020: Optical, Infrared, and Millimeter Wave, Proceedings Volume 11443, 114431L, 2020, DOI: 10.1117/12.2562063

13. Cisneros-González, M.E.; **Bolsée, D.; Van Laeken, L.; Pereira, N.; Gérard P.; Robert, S.; Vandaele, A.C.; Karatekin, O.**; Poulet, F.; Dumesnil, C.; Dubois, J.-P.; Hansotte, J.; Le Du, M.; Picot, L.
Thermal-vacuum and security system of the characterization facility for MAJIS/JUICE VIS-NIR FM and SM detectors
SPIE 2020, Space Telescopes and Instrumentation 2020: Optical, Infrared, and Millimeter Wave, Proceedings Volume 11443, 114437G, 2020, DOI: 10.1117/12.2576308

14. Cunningham, G.S.; **Botek, E.; Pierrard, V.**; Cully, C.; Ripoll, J.-F.
Observation of High-Energy Electrons Precipitated by NWC Transmitter from PROBA-V Low-Earth Orbit Satellite
Geophysical Research Letters, 47, 16, 2020, DOI: 10.1029/2020GL089077

15. **Decraemer, B.; Zhukov, A.N.**; Van Doorsselaere, T.
Properties of Streamer Wave Events Observed during the STEREO Era
The Astrophysical Journal, 893, 1, 78, 2020, DOI: 10.3847/1538-4357/ab8194

16. Dimitropoulou, E.; Hendrick, F.; Pinardi, G.; Friedrich, M.M.; Merlaud, A.; Tack, F.; De Longueville, H.**; Fayt, C.; Hermans, C.; Laffineur, Q.;** Fierens, F.**; Van Roozendael, M.**
Validation of TROPOMI tropospheric NO_2 columns using dual-scan multi-axis differential optical absorption spectroscopy (MAX-DOAS) measurements in Uccle, Brussels
Atmospheric Measurement Techniques, 13, 5165-5191, DOI: 10.5194/amt-13-5165-2020

17. Gogoberidze, G.; **Voitenko, Y.**
Model of Imbalanced Kinetic Alfvén Turbulence With Energy Exchange Between Dominant and Subdominant Components
Monthly Notices of the Royal Astronomical Society, 497, 3, 3472-3476, 2020, DOI: 10.1093/mnras/staa2146

18. Gogoberidze, G.; **Voitenko, Y.**
Spectrum of imbalanced Alfvénic turbulence at ion-kinetic scales in the solar wind
Astrophysics and Space Science, 365, 9, 149, 2020, DOI:10.1007/s10509-020-03865-8

19. Hayakawa, H.; **Clette, F.**; Horaguchi, T.; Iju, T.; Knipp, D.J.; Liu, H.; Nakajima, T.
Sunspot observations by Hisako Koyama: 1945-1996
Monthly Notices of the Royal Astronomical Society, 492, 3, 4513-4527, 2020, DOI: 10.1093/mnras/stz3345

20. Hofmeister, S.J.; Veronig, A.M.; Poedts, S.; **Samara, E.; Magdalenic, J.**
On the Dependency between the Peak Velocity of High-speed Solar Wind Streams near Earth and the Area of Their Solar Source Coronal Holes
The Astrophysical Journal Letters, 897, 1, L17, 2020, DOI: 10.3847/2041-8213/ab9d19

21. Hülsen, G.; Gröbner, J.; Bais, A.; Blumthaler, M.; Diemoz, H.; **Bolsée, D.**; Diaz, A.; Fountoulakis, I.; Naranen, E.; Schreder, J.; Stefania, F.; Vilaplana Guerrero, J.M.
Second solar ultraviolet radiometer comparison campaign UVC-II
Metrologia, 57, 035001, 2020, DOI: 10.1088/1681-7575/ab74e5

22. **Jebaraj, I.C.; Magdalenic, J.**; Podladchikova, T.; **Scolini, C.**; Pomoell, J.; Veronig, A.; Dissauer, K.; Krupar, V.; Kilpua, E. K. J.; Poedts, S.
Using radio triangulation to understand the origin of two subsequent type II radio bursts
Astronomy & Astrophysics, 639, A56, 2020, DOI: 10.1051/0004-6361/201937273

23. **Koukras, A.; Marqué, C.**; Downs, C.; **Dolla, L.**
Analyzing the propagation of EUV waves and their connection with type II radio bursts by combining numerical simulations and multi-instrument observations
Astronomy & Astrophysics, 644, A90, 2020, DOI: 10.1051/0004-6361/202038699

24. Lanabere, V.; Dasso, S.; Démoulin, P.; Janvier, M.; **Rodriguez, L.**; Masías-Meza, J.J.
Magnetic twist profile inside magnetic clouds derived with a superposed epoch analysis
Astronomy & Astrophysics, 635, A85, 2020, DOI: 10.1051/0004-6361/201937404

25. Lapenta, G.; **Zhukov, A.N.**; van Driel-Gesztelyi, L.
Editorial: Solar Wind at the Dawn of the Parker Solar Probe and Solar Orbiter Era
Solar Physics, 295, 7, 103, 2020, DOI: 10.1007/s11207-020-01670-8

26. Lazar, M.; **Pierrard, V.**; Poedts, S.; Fichtner, H.
Characteristics of solar wind suprathermal halo electrons
Astronomy & Astrophysics, 642, A130, 2020, DOI: 10.1051/0004-6361/202038830

27. Lazar, M.; Scherer, K.; Fichtner, H.; **Pierrard, V.**

Towards a realistic macroscopic parametrization of space plasmas with regularized Kappa-distribution
Astronomy & Astrophysics, 634, A20, 2020, DOI:10.1051/0004-6361/201936861

28. Lysak, R.; **Echim, M.**; Karlsson, T.; Marghitu, O.; Rankin, R.; Song, Y.; Watanabe, T.-H.
Quiet, Discrete Auroral Arcs: Acceleration Mechanisms
Space Science Reviews, 216, 5, A92, 2020, DOI: 10.1007/s11214-020-00715-5

29. **Magdalenic, J.; Marqué, C.**; Fallows, R.A.; Mann, G.; Vocks, C.; Zucca, P.; Dabrowski, B.P.; Krankowski, A.; Melnik, V.
Fine Structure of a Solar Type II Radio Burst Observed by LOFAR
The Astrophysical Journal Letters, 897, 1, L15, 2020, DOI: 10.3847/2041-8213/ab9abc

30. Meyer, K.A.; Mackay, D.H.; **Talpeanu, D.-C.**; Upton, L.A.; **West, M.J.**
Investigation of the Middle Corona with SWAP and a Data-Driven Non-Potential Coronal Magnetic Field Model
Solar Physics, 295, 7, 101, 2020, DOI: 10.1007/s11207-020-01668-2

31. **Micera, A.; Zhukov, A.N.**; López, R.A. ; Innocenti, M.E.; Lazar, M.; Boella, E.; Lapenta, G.
Particle-in-cell Simulation of Whistler Heat-flux Instabilities in the Solar Wind: Heat-flux Regulation and Electron Halo Formation
The Astrophysical Journal Letters, 903, 1, L23, 2020, DOI: 10.3847/2041-8213/abc0e8

32. **Micera, A.**; Boella, E.; **Zhukov, A.N.**; Shaaban, S.M.; Lazar, M.; Lapenta, G.
Particle-in-Cell simulations of the parallel proton firehose instability influenced by the electron temperature anisotropy in solar wind conditions
The Astrophysical Journal, 893, 2, 130, 2020, DOI: 10.3847/1538-4357/ab7faa

33. **Mierla, M.; Janssens, J.; D'Huys, E.; Wauters, L.; West, M.J.;** Seaton, D.B.**; Berghmans, D.; Podladchikova, E.**
Long-term Evolution of the Solar Corona Using PROBA2 Data
Solar Physics, 295, 5, 66, 2020, DOI: 10.1007/s11207-020-01635-x

34. Morosan, D.E.; Palmerio, E.; Rasanen, J.E.; Kilpua, E.K.J.; **Magdalenic, J.**; Lynch, B.J.; Kumari, A.; Pomoell, J.; Palmroth, M.
Electron acceleration and radio emission following the early interaction of two coronal mass ejections
Astronomy & Astrophysics, 642, A151, 2020, DOI: 10.1051/0004-6361/202038801

35. Müller, D.; St. Cyr, O.C.; Zouganelis, I.; … ; **Berghmans, D.**; … and 31 co-authors
The Solar Orbiter mission. Science overview
Astronomy & Astrophysics, 642, A1, 2020, DOI: 10.1051/0004-6361/202038467

36. Mumford, S.J.; Freij, N.; Christe, S.; … ; **De Vischer, R.**; … ; **Mampaey, B.; Verstringe, F.**; … and 120 co-authors
SunPy: A Python package for Solar Physics
Journal of Open Source Software, 5, 46, 1832, 2020, DOI: 10.21105/joss.01832

37. Park, S.-H.; Leka, K.D.; Kusano, K.; **Andries, J.**; … ; **Delouille, V.**; … and 19 co-authors
A Comparison of Flare Forecasting Methods. IV. Evaluating Consecutive-Day Forecasting Patterns
The Astrophysical Journal, 890, 2, 124, 2020, DOI: 10.3847/1538-4357/ab65f0

38. Parrish, D.D.; Derwent, R.G.; Steinbrecht, W.; Stübi, R.; **Van Malderen, R.**; Steinbacher, M.; Trickl, T.; Ries, L.; Xu, X.
Zonal Similarity of Long-term Changes and Seasonal Cycles of Baseline Ozone at Northern Mid-latitudes
Journal of Geophysical Research: Atmospheres, 125, 13, 2020, DOI: 10.1029/2019JD031908

39. Patel, R.; Pant, V.; Priyanka, I.; Banerjee, D.; **Mierla, M.; West, M.J.**
Automated Detection of Accelerating Solar Eruptions using Parabolic Hough Transform
Solar Physics, 296, 2, 31, 2020, DOI: 10.1007/s11207-021-01770-z

40. Pick, M.; **Magdalenic**, J.; Cornilleau-Wehrlin, N.; Grison, B.; Schmieder, B.; Bocchialini, K.
Role of the coronal environment in the formation of four shocks observed without coronal mass ejections at Earth's Lagrangian point L1
The Astrophysical Journal, 895, 2, 144, 2020, DOI: 10.3847/1538-4357/ab8fae

41. **Pierrard V.; Botek, E.;** Ripoll, J.-F.; Cunningham, G.S.
Electron dropout events and flux enhancements associated with geomagnetic storms observed by PROBA-V/EPT from 2013 to 2019
Journal of Geophysical Research: Space Physics, 125, 12, DOI: 10.1029/2020JA028487

42. **Pierrard, V.;** Lazar, M.; Stverak, S.
Solar wind plasma particles organized by the flow speed
Solar Physics, 295, 11, 151, 2020, DOI: 10.1007/s11207-020-01730-z

43. Poedts, S.; Kochanov, A.; Lani, A.; **Scolini, C.**; ... ; **De Keyser, J.; De Donder, E.; Crosby, N.B.; Echim, M.; Rodriguez, L.; Vansintjan, R.; Verstringe, F.; Mampaey, B.**; ... and 14 co-authors
The Virtual Space Weather Modelling Centre

Journal of Space Weather and Space Climate, 10, A14, 2020, DOI: 10.1051/swsc/2020012

44. Poedts, S.; Lani, A.; **Scolini, C.**; ... ; **Van der Linden, R.; Rodriguez, L.; Vanlommel, P.**; ... and 31 co-authors
EUropean Heliospheric FORecasting Information Asset 2.0
Journal of Space Weather and Space Climate, 10, A57, 2020, DOI: 10.1051/swsc/2020055

45. Raukunen, O.; Paassilta, M.; Vainio, R.; Rodriguez, J.V.; Eronen, T.; **Crosby, N.; Dierckxsens, M.;** Jiggens, P.; Heynderickx, D.; Sandberg, I.
Very high energy proton peak flux model
Journal of Space Weather and Space Climate, 10, A24, 2020, DOI: 10.1051/swsc/2020024

46. Rochus, P.; Auchère, F.; **Berghmans, D.**; … ; **BenMoussa, A.**; … ; **Bonte, K.**; … ; **Delouille, V.; Dolla, L.**; … ; **Giordanengo, B.; Gissot, S.**; … ; **Hochedez, J.-F.**; … ; **Kraaikamp, E.**; … ; **Mampaey, B.**; … ; **Nicula, B.; Parenti, S.**; … ; **Pylyser, E.**; … ; **Rodriguez, L.**; … ; **Seaton, D.**; … ; **Stegen, K.**; … ; **Verbeeck, C.**; … ; **West, M.**; … ; **Zhukov, A.N.** and 128 co-authors
The Solar Orbiter EUI instrument: The Extreme Ultraviolet Imager
Astronomy & Astrophysics, 642, A8, 2020, DOI: 10.1051/0004-6361/201936663

47. **Rodriguez, L.; Scolini, C.; Mierla, M.; Zhukov, A.N.; West, M.J.**
Space weather monitor at the L5 point: a case study of a CME observed with STEREO B
Space Weather, 18, 10, 2020, DOI: 10.1029/2020SW002533

48. Rouillard, A.P.; Pinto, R.F.; Vourlidas, A.; … ; **Berghmans, D.**; … ; **Nicula, B.**; … ; **Kraaikamp, E.**; … ; **Rodriguez, L.**; … ; **Verbeeck, C.**; … ; **Zhukov, A.N.** and 96 co-authors
Models and data analysis tools for the Solar Orbiter mission
Astronomy & Astrophysics, 642, A2, 2020, DOI: 10.1051/0004-6361/201935305

49. **Sapundjiev, D.; Verhulst, T.; Stankov, S.**
International Database of Neutron Monitor Measurements: Development and Applications Knowledge Discovery in Big Data from Astronomy and Earth Observation (Eds. P. Skoda and F. Adam), Elsevier Science Publishing Co., Amsterdam, 371-383, 2020, DOI: 10.1016/B978-0-12-819154-5.00032-1

50. **Schifano, L.**; Smeesters, L.; Geernaert, T.; Berghmans, F.; **Dewitte, S.**
Design and Analysis of a Next-Generation Wide Field-of-View Earth Radiation Budget Radiometer
Remote Sensing, 12, 3, 2020, DOI: 10.3390/rs12030425

51. **Schifano, L.**; Smeesters, L.; Berghmans, F.; **Dewitte, S.**
Optical System Design of a Wide Field-of-View Camera for the Characterization of Earth's Reflected Solar Radiation
Remote Sensing, 12, 16, 2020, DOI: 10.3390/rs12162556

52. **Schifano, L.**; Smeesters, L.; Meulebroeck, W.; Berghmans, F.; **Dewitte, S.**
VACNT versus Black Velvet: a coating analysis for the next-generation Earth Radiation Budget radiometer
SPIE 2020, Remote Sensing of Clouds and the Atmosphere XXV, Proceedings Volume 11531, 115310J, 2020, DOI: 10.1117/12.2573996

53. **Schifano, L.**; Smeesters, L.; Berghmans, F.; **Dewitte, S.**
Towards a next-generation Earth Radiation Budget radiometer by optimization of the cavity geometry and coating
SPIE 2020, International Conference on Space Optics - ICSO 2020, Proceedings Volume 11852, 118520O, 2020, DOI: 10.1117/12.2599171

54. **Scolini, C.**; Chané, E.; Temmer, M.; Kilpua, E.; Dissauer, K.; Veronig, A.; Palmerio, E.; Pomoell, J.; Dumbovic, M.; Guo, J.; **Rodriguez, L.**; Poedts, S.
CME-CME Interactions as Sources of CME Geo-effectiveness: The Formation of the Complex Ejecta and Intense Geomagnetic Storm in 2017 Early September
The Astrophysical Journal Supplement Series, 247, 1, 21, 2020, DOI: 10.3847/1538-4365/ab6216

55. **Scolini, C.**; Chané, E.; Pomoell, J.; **Rodriguez, L.**; Poedts, S.
Improving predictions of high-latitude Coronal Mass Ejections throughout the heliosphere
Space Weather, 18, 3, 02246, 2020, DOI: 10.1029/2019SW002246

56. **Shestov, S.V.; Bourgoignie, B.; Nicula, B.; Dolla, L.; Jean, C.; Verstringe, F.; Katsiyannis, T.;** Inhester, B.; Dalmiro, M.; Ribeiro, B.M.F.; **Zhukov, A.N.**
Scientific processing pipeline for ASPIICS coronagraph
SPIE 2020, Space Telescopes and Instrumentation 2020: Optical, Infrared, and Millimeter Wave, Proceedings Volume 11443, 114432U, 2020, DOI: 10.1117/12.2560164

57. Sieyra, M.V.; Cécere, M.; Cremades, H.; Iglesias, F.A.; Sahade, A.; **Mierla, M.**; Stenborg, G.; Costa, A.; **West, M.J.; D'Huys, E.**
Analysis of Large Deflections of Prominence-CME Events during the Rising Phase of Solar Cycle 24
Solar Physics, 295, 9, 126, 2020, DOI: 10.1007/s11207-020-01694-0

58. Stauffer, R.M.; Thompson, A.M.; Kollonige, D.E.; … ; **Van Malderen, R.**; … and 10 co-authors
A Post-2013 Drop-off in Total Ozone at a Third of Global Ozonesonde Stations: ECC Instrument Artifacts?
Geophysical Research Letters, 47, 2020, DOI: 10.1029/2019GL086791

59. **Talpeanu, D.-C.**; Chané, E.; Poedts, S.; **D'Huys, E.; Mierla, M.**; Roussev, I.; Hosteaux, S.
Numerical Simulations of Shear-Induced Consecutive Coronal Mass Ejections
Astronomy & Astrophysics, 637, A77, 2020, DOI: 10.1051/0004-6361/202037477

60. Teodorescu, E.; **Echim, M.M.**
Open-Source Software Analysis Tool to Investigate Space Plasma Turbulence and Nonlinear DYNamics (ODYN)
Earth and Space Science, 7, 4, 2020, DOI: 10.1029/2019EA001004

61. Tezari, A.; Paschalis, P.; Mavromichalaki, H.; Karaiskos, P.; **Crosby, N.; Dierckxsens, M.**
Assessing Radiation Exposure inside the Earth's Atmosphere
Radiation Protection Dosimetry, 190, 4, 427-436, 2020, DOI: 10.1093/rpd/ncaa112

62. **Van Malderen, R.; Pottiaux, E.**; … and 14 co-authors.
Homogenizing GPS Integrated Water Vapor Time Series: Benchmarking Break Detection Methods on Synthetic Data Sets
Earth and Space Science, 7, 5, 2020, DOI: 10.1029/2020EA001121

63. Velli, M.; Harra, L.K. ; Vourlidas, A.; … ; **Berghmans, D.**; … and 27 co-authors
Understanding the origins of the heliosphere: integrating observations and measurements from Parker Solar Probe, Solar Orbiter, and other space- and ground-based observatories
Astronomy & Astrophysics, 642, A4, 2020, DOI: 10.1051/0004-6361/202038245

64. **Verhulst, T.G.W.; Stankov, S.**
Height dependency of solar eclipse effects: the ionospheric perspective
Journal of Geophysical Research, 125, 7, 2020, DOI: 10.1029/2020JA028088

65. Vömel, H.; Smit, H.G.J.; Tarasick, D.; … ; **Van Malderen, R.**; … and 10 co-authors
A new method to correct the electrochemical concentration cell (ECC) ozonesonde time response and its implications for "background current" and pump efficiency
Atmospheric Measurement Techniques, 13, 10, 5667-5680, 2020, DOI: 10.5194/amt-13-5667-2020

66. **West, M.J.**; Kintziger, C.; Haberreiter, M.; Gyo, M.; **Berghmans, D.; Gissot, S.**; Büschel, V; Golub, L.; **Shestov, S.**; Davies, J.
LUCI onboard Lagrange, the Next Generation of EUV Space Weather Monitoring
Journal of Space Weather and Space Climate, 10, A49, 2020, DOI: 10.1051/swsc/2020052

67. Zhang, P.J.; Zucca, P.; Wang, C.B.; Bisi, M.M.; Dąbrowski, B.; Fallows, R.A.; Krankowski, A.; **Magdalenic, J.**; Mann, G.; Morosan, D.E.; Vocks, C.
The Frequency Drift and Fine Structures of Solar S-bursts in the High Frequency Band of LOFAR
The Astrophysical Journal, 891, 1, 89, 2020, DOI: 10.3847/1538-4357/ab7005

68. Zhang, P.J.; Zucca, P.; Sridhar, S.S.; Wang, C.B.; Bisi, M.M.; Dabrowski, B.; Krankowski, A.; Mann, G. ; **Magdalenic, J.**; Morosan, D.E.; Vocks, C.
Interferometric imaging with LOFAR remote baselines of the fine structures of a solar type-IIIb radio burst
Astronomy & Astrophysics, 639, A115, 2020, DOI: 10.1051/0004-6361/202037733

69. Zharkov, S.; Matthews, S.; Zharkova, V.; Druett, M.; Inoue, S.; **Dammasch, I.E.**; Macrae, C.
Sunquake with a second bounce, other sunquakes, and emission associated with the X9.3 flare of 6 September 2017 I. Observations
Astronomy & Astrophysics, 639, A78, 2020, DOI: 10.1051/0004-6361/201936755

70. Zouganelis, I.; De Groof, A.; Walsh, A.P.; … ; **Berghmans, D.**; … ; **Dolla, L.**; … ; **Gissot, S.**; … ; **Rodriguez, L.**; … ; **Verbeeck, C**.; … ; **Zhukov, A.N**. and 176 co-authors
The Solar Orbiter Science Activity Plan - Translating solar and heliospheric physics questions into action
Astronomy & Astrophysics, 642, A3, 2020, DOI: 10.1051/0004-6361/202038445

Presentations and posters at conference

1. Aran, A.; Pacheco, D.; Wijsen, N.; … and 17 others
The Low-Energy Ion Event on 19 June 2020 Measured by Solar Orbiter
AGU Fall Meeting, Online, 1-17 December 2020

2. Auchère, F.; Gissot, S.; Teriaca, L.; Berghmans, D.; Harra, L.; Long, D.; Rochus, P.L.; Smith, P.; Schühle, U.; Stegen, K.; Aznar Cuadrado, R.; Heerlein, K.; Kraaikamp, E.; Verbeeck, C.
First Images and Initial In-Flight Performance of the Extreme Ultraviolet Imager On-Board Solar Orbiter
AGU Fall Meeting, Online, 1-17 December 2020 (poster)

3. Aznar Cuadrado, R.; Berghmans, D.; Gissot, S.; Kraaikamp, E.; Stegen, K.; Verbeeck, C.
Very high-resolution observations of the solar atmosphere in H I Lyman alpha and Fe IX-X at 17.4 nm as seen by EUI aboard Solar Orbiter
AGU Fall Meeting, Online, 1-17 December 2020 (poster)

4. Bemporad, A.; Banerjee, D.; Berlicki, A.; … and 40 others
Modelling of CME propagation/evolution in corona and solar wind in connection with Space Weather
AGU Fall Meeting, Online, 1-17 December 2020 (poster)

5. Bergeot, N.; Habarulema, J.B.; Chevalier, J.-M.; Matamba, T.; Pinat, E.; Cilliers, P.; Burešová, D.
Inter-hemispheric comparison of the ionosphere-plasmasphere system from multi-instrumental/model approach
EGU General Assembly 2020, Online, 4-8 May 2020

6. Bolsée, D.; Cisneros, M.; Pereira, N.; Van Laeken, L.; Langevin, Y.; Poulet, F.; Haffoud, P.
VIS-NIR FPA Characterization
MAJIS Science Team Meeting, Online, 11-12 November 2020

7. Bolsée, D.; Van Laeken, L.; Cisneros-González, M.E.; … and 15 others
Characterization facility for the MAJIS/JUICE VIS-NIR FM and SM detectors
SPIE 2020, Space Telescopes and Instrumentation 2020: Optical, Infrared, and Millimeter Wave, Online, 13-18 December 2020 (poster)

8. Botek, E.; Pierrard, V.; De Keyser, J.; Calders, S.; De Donder, E.
Integration of BIRA Plasmasphere-Ionosphere Model (BPIM) at VSWMC and Discussion of Future Improvements in the Context of ESA and European Projects
ESA SWE Service Network Workshop, Online, 12-14 October 2020

9. Bruyninx, C.; Fabian, A.; Legrand, J.; Miglio, A.
GNSS Station Metadata Revisited in Response to Evolving Needs
EGU General Assembly 2020, Online, 4-8 May 2020 (poster)

10. Buchlin, E.; Teriaca, L.; Giunta, A.S.; … and 32 others
First results from the EUI and SPICE observations of Alpha Leo near Solar Orbiter first perihelion
AGU Fall Meeting, Online, 1-17 December 2020 (poster)

11. Chevalier, J.-M.; Bergeot, N.; Defraigne, P.; Marqué, C.; Pinat, E.
Solar radio burst interference index dedicated to GNSS single and double frequency users
EGU General Assembly 2020, Online, 4-8 May 2020

12. Cisneros-González, M.E.; Bolsée, D.; Pereira, N.; … and 16 others
MAJIS/JUICE VIS-NIR FM and SM detectors characterization
SPIE 2020, Space Telescopes and Instrumentation 2020: Optical, Infrared, and Millimeter Wave, Online, 13-18 December 2020

13. Cisneros-González, M.E.; Bolsée, D.; Van Laeken, L.; Pereira, N.; Gérard P.; Robert, S.; Vandaele, A.C.; Karatekin, O.; Poulet, F.; Dumesnil, C.; Dubois, J.-P.; Hansotte, J.; Le Du, M.; Picot, L.
Thermal-vacuum and security system of the characterization facility for MAJIS/JUICE VIS-NIR FM and SM detectors
SPIE 2020, Space Telescopes and Instrumentation 2020: Optical, Infrared, and Millimeter Wave, Online, 13-18 December 2020 (poster)

14. Cunningham, G.S.; Botek, E.; Pierrard, V.; Cully, C.; Ripoll, J.-F.
Observation of High-Energy Electrons Precipitated by NWC Transmitter from PROBA-V Low-Earth Orbit Satellite
AGU Fall Meeting, Online, 1-17 December 2020

15. Dandouras, I.; Devoto, P.; De Keyser, J.; ... and 17 others
SP4GATEWAY: a Space Plasma Physics Payload Package conceptual design for the Deep Space Gateway Lunar Orbital Platform
EGU General Assembly 2020, Online, 4-8 May 2020

16. Darrouzet F.; Koronczay, D.; Pierrard, V.; Bergeot, N.; De Keyser, J.; Lichtenberger, J.
Plasmaspheric studies with ground-based instruments (VLF antenna in Antarctica), satellite data (Cluster mission) and a 3D empirical model

GRAPE/RESOURCE Online Workshop, Online, 1-3 July 2020 (invited talk)

17. Dasso, S.; Lanabere, V.; Démoulin, P.; Janvier, M.; Rodriguez, L.; Masías-Meza, J.-J.
Magnetic field lines distribution inside magnetic clouds
62nd annual meeting of the Argentinian Association of Astronomy, Online, 13-16 October 2020

18. Dasso, S.; Lanabere, V.; Démoulin, P.; Janvier, M; Rodriguez, L.; Masias-Meza, J.-J.
Magnetic field lines distribution inside magnetic clouds
ESWS2020, Online, 2-6 November 2020 (poster)

19. Decraemer, B.
Helmet streamers in the solar corona and their oscillations
Thesis, Public PhD Defense, 1 October 2020

20. De Donder, E.; Calegaro, A.; Chabanski, S.; Vansintjan, R.; O'Hara, J.; Liber, C.; Glover, A.
ESA SSA SWE Service to Aviation
ESWS2020, Online, 2-6 November 2020

21. De Donder, E.
GCR Models and their Usage in SPENVIS
ESA SWE Service Network Workshop, Online, 12-14 October 2020

22. De Donder, E.
SSCC User Engagement Activities – User Support Test Campaigns
ESA SWE Service Network Workshop, Online, 12-14 October 2020

23. De Keyser, J.; Echim, M.; Ranvier, S.; Chambon, T.; Ordoubadian, B.; Lemke, N.
Thermal behaviour of ram-facing instruments during deep dives into a planetary atmosphere: The case of Daedalus/CWS
EGU General Assembly 2020, Online, 4-8 May 2020

24. Delouille, V.
Unified content descriptors (UCD) in solar physics
ESCAPE-WP4 Technology Forum 1, Strasbourg, France, 4-6 February 2020

25. Delouille, V.; Mampaey, B.
HEK database: solar events using VOEvent
ESCAPE WP4 Provenance workshop, Online, 7-8 September 2020

26. Delouille, V.
IVOA Standard for data access
ESA SWE Service Network Workshop, Online, 12-14 October 2020 (invited talk)

27. Dolla, L.; Zhukov, A.N.
The diagnostic capabilities of PROBA-3/ASPIICS
Meeting of the Metis Topical Team "Wind diagnostics", Online, 21 October 2020

28. Dolla, L.; Zhukov, A.N.
PROBA-3/ASPIICS: A giant formation-flying coronagraph to study the low and middle solar corona
Meeting of the Metis Topical Team "Plasma density fluctuations, turbulence and waves", Online, 15 October 2020

29. Dolla, L.; Zhukov, A.N.
PROBA-3/ASPIICS: A giant formation-flying coronagraph to study the low and middle solar corona
5th Asia Pacific Solar Physics Meeting, Pune, India, 3-7 February 2020

30. Fabian, A.; Bruyninx, C.; Legrand, J.; Miglio, A.
GNSS data quality check in the EPN network
EGU General Assembly 2020, Online, 4-8 May 2020 (poster)

31. Grimani, C.; Andretta, V.; Chioetto, P.; Da Deppo, V.; Fabi, M.; Gissot, S.; Naletto, G.; Plainaki, C.; Romoli, M.; Spadaro, D.; Stangalini, M.; Telloni, D.
A Radiation Environmental Study for the Metis Coronagraph on board Solar Orbiter
AGU Fall Meeting, Online, 1-17 December 2020

32. Habarulema, J.B.; Bergeot, N.; Chevalier, J.-M.; Pinat, E.; Buresova, D.; Matamba, T.; Katamzi-Joseph, Z.
Interhemispheric comparison of the ionospheric electron density response during geomagnetic storm conditions
EGU General Assembly 2020, Online, 4-8 May 2020

33. Horbury, T.; Laker, R.; Auchère, F.; Rodriguez, L.; Maksimovic, M.; Livi, S.
Solar Orbiter: Connecting remote sensing and in situ instruments
AGU Fall Meeting, Online, 1-17 December 2020

34. Ivanković L.; Bandić, M.; Verbanac, G.; Pierrard, V.
Plasmapause evolution during prolonged conditions of quiet geomagnetic activity
ESWS2020, Online, 2-6 November 2020

35. Katsiyannis, T.; Zhukov, A.N.; Berghmans, D.; Nicula, B.
EUI data exploitation and synergy with other instruments
The near-Sun solar wind at solar minimum, RAS specialist Discussion Meeting, London, London, UK, 13 March 2020

36. Lamy, H.; Anciaux, M.; Ranvier, S.; Calegaro, A.; Johannink, C.
Ionization profile of meteors from simultaneous video and radio forward scatter observations
EGU General Assembly 2020, Online, 4-8 May 2020

37. Legrand, J.; Bruyninx, C.

Quality assessment of GNSS reference stations: Criteria and Thresholds
EGU General Assembly 2020, Online, 4-8 May 2020

38. Le Maistre, S.; Bergeot, N.; Witasse, O.; Blelly, P.-L.; Kofman, W.; Peter, K.; Dehant, V.; Chevalier, J.-M.; Karatekin, Ö.
MoMo's prediction of Mars' ionosphere contribution to InSight RISE Doppler data
EGU General Assembly 2020, Online, 4-8 May 2020

39. Magdalenic, J.; Marqué, C.; Fallows, R.A.; Mann, G.; Vocks, C.; Zucca, P.; Dabrowski, B.; Krankowski, A.; Melnik, V.
Fine structures of a solar type II radio burst observed by LOFAR
AGU Fall Meeting, Online, 1-17 December 2020

40. Magdalenic, J.
Solar radio observations and their application in the space weather
AGU Fall Meeting, Online, 1-17 December 2020

41. Magdalenic, J.
Radio dynamic spectra and interplanetary scintillations for Space Weather
Thematic Workshop of ESA's Situational Awareness programme, Online, 13 October 2020 (invited talk)

42. Mampaey, B.; Vansintjan, R.
SOLARNET Virtual Observatory From prototype to operational
4th IHDEA meeting, Online, 19-22 October 2020

43. Micera, A.; Zhukov, A.N.; López, R.A.; Innocenti, M.E.; Lazar, M.; Boella, E.; Lapenta, G.
Particle-In-Cell Simulations of Whistler Heat Flux Instabilities in the Solar Wind: Heat Flux Regulation and Electron Halo Formation
AGU Fall Meeting, Online, 1-17 December 2020

44. Micera, A.; Zhukov, A.N.; López, R.A.; Innocenti, M.E.; Lazar, M.; Boella, E.; Lapenta, G.
Particle-In-Cell simulations of the oblique whistler heat flux instability. Scattering of the strahl electrons into the halo and heat flux regulation in the solar wind near the Sun
62nd Annual Meeting of the APS Division of Plasma Physics (DPP), Online, 9-13 November 2020

45. Mierla, M.; Janssens, J.; D'Huys, E.; Wauters, L.; West, M.J.; Seaton, D.B.; Berghmans, D.; Podladchikova, E.
Long-term Evolution of the Solar Corona Using PROBA2 Data
AGU Fall Meeting, Online, 1-17 December 2020 (poster)

46. Miglio, A.; Bruyninx, C.; Fabian, A.; Legrand, J.; Pottiaux, E.; Van Nieuwerburgh, I.; Moreels, D.
Towards FAIR GNSS data: challenges and open problems
EGU General Assembly 2020, Online, 4-8 May 2020 (poster)

47. Moeller, G.; Ao, C.; Adavi, Z.; Brenot, H.; Sá, A.; Hajj, G.; Hanna, N.; Kitpracha, C.; Pottiaux, E.; Rohm, W.; Shehaj, E.; Trzcina, E.; Wang, K.-N.; Wilgan, K.; Zhang, K.
Sensing small-scale structures in the troposphere with tomographic principles
EGU General Assembly 2020 (IAG working group), Online, 4-8 May 2020

48. Negrea, C.; Munteanu, C.; Echim, M.
Global Ionospheric Response to CIR/HSS Induced Geomagnetic Storms
EGU General Assembly 2020, Online, 4-8 May 2020

49. Parenti, S.; Berghmans, D.; Buchlin, E.; … and 12 others
Observation of Smallest Ever Detected Brightening Events with the Solar Orbiter EUI HRI-EUV Imager
AGU Fall Meeting, Online, 1-17 December 2020

50. Pereira, N.; Bolsée, D.; Cessateur, G.; Sperfeld, P.; Pape, S.; Sluse, D.
Near Infrared Ground-based Spectrum (results of the PYR-ILIOS campaign at Mauna Loa Observatory in 2016)
2020 Sun-Climate Symposium, Session 5: A New Reference Spectrum for Remote Sensing, Tucson, Arizona, USA, 27-31 January 2020 (invited talk)

51. Pesnell, W.D.; Clette, F.; Lefèvre, L.
The latest on the reconstruction of the Sunspot Number
American Meteorological Society: 100th Annual meeting, Boston, Massachusetts, USA, 12-16 January 2020, (poster)

52. Pierrard V.; Botek E.
Radiation belt physics from top to bottom: Combining multipoint satellite observations and data assimilative models to determine the interplay between sources and losses
ISSI, Bern, Switzerland, 27-31 January 2020 (invited talk)

53. Pierrard V.; Lazar, M.; Poedts, S.
Characteristics of the suprathermal population of electrons in the plasma of the solar wind
19th Annual International Astrophysics Conference, Santa Fe, New Mexico, USA, 9-13 March 2020 (invited talk)

54. Pierrard V.; Botek, E.; Ripoll, J.-F.; Cunningham, G.
Electron dropout events and flux enhancements associated with geomagnetic storms observed by PROBA-V/EPT from 2013 to 2019
AGU Fall Meeting, Online, 1-17 December 2020

55. Podladchikova, E.; Harra, L.; Barczynski, K.; Mandrini, C.; Auchère, F.; Buchlin, E.; Dolla, L.; Mierla, M.; Parenti, S.; Rodriguez, L.
Stereoscopic Measurements of Coronal Doppler Velocities

AGU Fall Meeting, Online, 1-17 December 2020

56. Podladchikova, O.; Harra, L.; Berghmans, D.; Mierla, M.; Rodriguez, L.; Verbeeck, C.
Prospects for improving existing space weather forecasting schemes using Extreme Ultraviolet Imager data onboard Solar Orbiter
4th Swiss SCOSTEP Workshop, Online, 29-30 October 2020

57. Pottiaux, E.; Van Malderen, R.
GNSS-derived water vapour observations at high latitudes: long-term variability and contribution to weather forecasting
GRAPE Workshop, Online, 1-3 July 2020 (invited talk)

58. Ranvier, S.; De Keyser, J, Lebreton, J.-P.
Monitoring of the upper ionosphere with SLP on board PICASSO
SPACEMON: Space Environment Monitoring Workshop, Online, 1-3 December 2020

59. Ranvier, S.; Anciaux, M.; Lebreton, J.-P.; De Keyser, J.
Validation and characterisation of the Sweeping Langmuir Probe (SLP) instrument for the PICASSO mission
EGU General Assembly 2020, Online, 4-8 May 2020

60. Rodriguez, L.; Zhukov, A.; Nicula, B.; Berghmans, D.; Verbeeck, F.; Auchère, F.; Horbury, T.; Laker, R.; Livi, S.; Rodriguez-Pacheco, J.; Aran, A.; Gómez Herrero, R.; Maksimovic, M.; Krupar, V.
Linking EUI to in situ instruments
EUI Consortium meeting, Online, 30 November 2020

61. Rodriguez, L.
Validation for EUHFORIA 2.0
EUHFORIA 2.0 review meeting, Online, 25 May 2020 (invited talk)

62. Rodriguez, L.; Magdalenic, J.; Mierla, M.; Niemela, A.; Samara, E.; Scolini, C.; Vansintjan, R.; Vanlommel, P.; Verbeke, C.
Validation for EUHFORIA 2.0
EUHFORIA 2.0 External Review Meeting, Online, 4 December 2020 (invited talk)

63. Rodriguez, L.; Magdalenic, J.; Mierla, M.; Niemela, A.; Samara, E.; Scolini, C.; Vansintjan, R.; Vanlommel, P.; Verbeke, C.
Validation for EUHFORIA 2.0
EUHFORIA 2.0 annual meeting, Online, 3 December 2020 (invited talk)

64. Samara, E.; Magdalenic, J.; Pinto, R.F.; Jercic, V.; Scolini, C.; Rodriguez, L.; Poedts, S.
Coupling the MULTI-VP model with EUHFORIA
EGU General Assembly 2020, Online, 4-8 May 2020

65. Samara, E.; Pinto, R.F.; Magdalenic, J.; Wijsen, N.; Jercic, V.; Scolini, C.; Jebaraj, I.J.; Rodriguez, L.; Poedts, S.
Implementing the Multi-VP coronal model in EUHFORIA: results and comparisons with the WSA coronal model
ESWS2020, Online, 2-6 November 2020 (poster)

66. Samara, E.; Pinto, R.F.; Magdalenic, J.; Wijsen, N.; Jercic, V.; Scolini, C.; Jebaraj, I.J.; Rodriguez, L.; Poedts, S.
Implementing the Multi-VP coronal model in EUHFORIA: results and comparisons with the WSA coronal model
Annual Meeting of the German Astronomical Society, Online, 21-25 September 2020

67. Samara, E.; Pinto, R.F.; Magdalenic, J.; Wijsen, N.; Jercic, V.; Scolini, C.; Jebaraj, I.J.; Rodriguez, L.; Poedts, S.
Implementing the Multi-VP coronal model in EUHFORIA: results and comparisons with the WSA coronal model
AGU Fall Meeting, Online, 1-17 December 2020

68. Sapundjiev, D.; Stankov, S.
Comparison between the observed and the computer modeled neutron monitor count rates
NMDB@Home - Virtual symposium on cosmic ray studies with neutron detectors, Online, 13–17 July 2020

69. Schifano, L.; Dewitte, S.; Smeesters, L.; Berghmans, F.; Meftah, M.; Keckhut, P.
The Absolute Solar-TErrestrial Radiation Imbalance eXplorer (ASTERIX) 6U CubeSat mission: a European contribution to the monitoring of the Earth's radiation budget from the morning orbit
34th CERES-II Science Team Meeting, Online, 15-17 September 2020

70. Scolini, C.; Pomoell, J.; Chané, E.; Poedts, S.; Rodriguez, L.; Kilpua, E.; Temmer, M.; Verbeke, C.; Dissauer, K.; Veronig, S.; Palmerio, E.; Dumbović, M.
Observation-based modelling of magnetised CMEs in the inner heliosphere with EUHFORIA
EGU General Assembly 2020, Online, 4-8 May 2020 (invited talk)

71. Scolini, C.
Magnetised Coronal Mass Ejections: evolution from the Sun to 1 AU and geo-effectiveness
Thesis, Public PhD Defense, Online, 29 May 2020

72. Teriaca, L. ; Aznar Cuadrado, R. ; Giunta, A. S. ; … and 32 others
First results from combined EUI and SPICE observations of Lyman lines of Hydrogen and He II
AGU Fall Meeting, Online, 1-17 December 2020 (poster)

73. Vanlommel, P.
Outreach, dissemination and exploitation - maximise the impact of EUHFORIA 2.0
EUHFORIA 2.0 General Assembly, 4 December 2020 (invited talk)

74. Van Malderen, R.; Pottiaux, E.; , Klos, A.; … and 14 others
Homogenizing GPS integrated water vapor time series: benchmarking break detection methods on synthetic datasets
International Workshop on Improving GNSS and SAR Tropospheric Products for Meteorology, Luxembourg city, Grand-Duchy of Luxembourg, 25-26 February 2020

75. Van Malderen, R., Pottiaux, E., Klos, A., … and 13 others
Break detection in integrated water vapour benchmark datasets
10th Seminar for Homogenization and Quality Control and 5th Conference on Spatial Interpolation Techniques in Climatology and Meteorology, Online, 12-14 October 2020

76. Van Malderen, R.; Smit, H.G.J.; Thompson, A.M.; Stauffer, R.; Kollonige, D.; Tarasick, D.; Johnson, B.; and ASOPOS panel
Status of the homogenization activity of the global ozonesonde network
LOTUS 3rd workshop, Online, 28-29 May 2020

77. Vansintjan, R.; Calegaro, A.; De Donder, E.; Chabanski, S.; O'Hara, J.; Liber, C.; Laurens, H.; Glover, A.
ESA SSA Space Weather Service Network - Provision of a General Space Weather Dashboard in Support of Spacecraft Operations
ESWS2020, Online, 2-6 November 2020

78. Verbanac, G.; Bandic, M.; Pierrard, V.
Explanation of global plasmapause characteristics in the frame of interchange instability mechanism
EGU General Assembly 2020, Online, 4-8 May 2020 (poster)

79. Verbeeck, C.; Lamy, H.; Calders, S.; Martínez Picar, A.; Calegaro, A.; Anciaux, M.
Year-to-year comparison of BRAMS forward scatter observations of selected meteor showers
International Meteor Conference 2020, Online, 19 September 2020

Public Outreach: Talks and publications for the general public

1. Anciaux, M.; Lamy, H.; Martínez Picar, A.; Calders, S.; Calegaro, A.; Ranvier, S.; Verbeeck, C.
The BRAMS receiving station V2.0
Proceedings of IMC2019, Bollmansruh, Germany, 3-6 October 2019, 2020

2. Bergeot, N.; Alfonsi, L.; Cilliers, P.J.; … ; 22 co-authors and the GRAPE EG members
Polar atmosphere and Geospace: Present knowledge, infrastructures and future research directions
SCAR White Paper, 2020

3. Cisneros, M.
MAJIS project
National Institute of Astronomy, Optics and Electronics (IANOE), Puebla, Mexico, July 2020

4. Cisneros, M.
MAJIS project
Scientific communication journal from Durango, Mexico: Sapiens+, Vol. 1, January-April 2020

5. Clette, F.; Vaquero, J.M.; Cruz Gallego, M.; Lefèvre, L.
Sunspot and Group Number: Recent advances from historical data
Proceedings of the IAU, 14, 156-159, 2020, DOI: 10.1017/S174392131900396X

6. D'Huys, E.; O'Hara, J.
PROBA2 sees a Partial Eclipse on December 26, 2019
P2SC News Item, 9 January 2020

7. D'Huys, E.
PROBA2 data processing to be paused on June 24 - newly calibrated data will be published!
P2SC News Item, 16 June 2020

8. D'Huys, E.; Dominique, M.
Solstice Eclipse
P2SC News Item, 16 June 2020

9. D'Huys, E.; Mierla, M.
Long-term evolution of the solar corona using PROBA2 data
P2SC News Item, 7 July 2020

10. D'Huys, E.; Dominique, M.
December 14, eclipse time!
P2SC News Item, 11 December 2020

11. Janssens, J.
Zon en ruimteweer
MIRA Public Observatory, 23 September 2020

12. Janssens, J.
McIntosh en de zonnevlekken
Zonnekijkdag, 5 July 2020

13. Janssens, J.; Vanlommel, P.; D'Huys, E.
SWIC - Appetizer
SWIC, 15 September 2020

14. Lamy, H.; Anciaux, M.; Ranvier, S.; Martínez Picar, A.; Calders, S.; Calegaro, A.; Verbeeck, C.
Calibration of the BRAMS interferometer
Proceedings of IMC2019, Bollmansruh, Germany, 3-6 October 2019, 2020

15. Lamy, H.
A l'écoute des étoiles filantes
Groupe d'Astronomie de Spa, 31 January 2020

16. Martínez Picar, A.
Clima Solar y Radio Astronomía
Santo Domingo, Dominican Republic, 15 January 2020

17. Van Camp, M.; Declercq, P.-Y.; Camelbeeck, T.; Bruyninx, C.; Legrand, J.; de Viron, O.; Gobron, K.
Vertical land movements in northwest Europe
Data-analyse waterstandreeksen Kust en Schelde, 3 July 2020

18. Vanlommel, P.; Janssens, J.
STCE Newsletter
Weekly newsletter, https://www.stce.be/ , 2020

19. Vanlommel, P.
Wat hebben Zon, satellieten en vliegtuigen gemeen? Ruimteweer!
Soap box Science Brussels, 10 October 2020

20. Vanlommel, P.
PECASUS Operator, level 2
Training for PECASUS operator, Meteowing, 15 October 2020

21. Vanlommel, P.
PECASUS Operator, level 1
Training for PECASUS operator, Meteowing, 22 October 2020

22. Vanlommel, P.
PECASUS Operator, level 2
Training for PECASUS operator, Meteowing, 29 October 2020

23. Vanlommel, P.
PECASUS Operator, level 2
Training for PECASUS operator, Meteowing, 10 November 2020

24. Vanlommel, P.
PECASUS Operator, level 2
Training for PECASUS operator, Meteowing, 19 November 2020

25. Vanlommel, P.
PECASUS Operator, level 2
Training for PECASUS operator, Meteowing, 10 December 2020

26. Vanlommel, P.; Marqué, C.; Maneva, Y.
GNSS, HF and Radiation Dashboards
Training for PECASUS operators, 11 February 2020

27. Vanlommel, P.
Triggers of advisories
Training for PECASUS operators, 11 February 2020

28. Vanlommel, P.
SWx for aviation
Training for PECASUS operators, 11 February 2020

29. Vanlommel, P.; Berghmans, D.
Structures and tasks
Training for PECASUS Operators, 11 February 2020

30. Vanlommel, P.
Triggers for Advisories
Training for PECASUS Operators, 14 January 2020

31. Vanlommel, P.
SWx for aviation
Training for PECASUS Operators, 14 January 2020

32. Vanlommel, P.
Training for PECASUS Operators
Space Pole, 11 February 2020

33. Van Malderen, R.
Climate change and the greenhouse gases water vapour and ozone
Presentation of the RMI Climate Report, Uccle, 15 October 2020.

34. Van Malderen, R.; De Muer, D.; De Backer, H.; Poyraz, D.; Verstraeten, W.W.; De Bock, V.; Delcloo, A.; Mangold, A.; Laffineur, Q.; Allaart, M.; Fierens, F.; Thouret V.
50 jaar ozonpeilingen met weerballonnen in Ukkel
Tijdschrift Lucht, Jaargang 16, nummer 4, december 2020

35. Verbeeck, C.; Lamy, H.; Calders, S.; Martínez Picar, A.; Calegaro, A.; Anciaux, M.
Year-to-year comparison of BRAMS forward scatter observations of selected meteor showers
WGN - Journal of the IMO, 48, 142-145, 2020

36. Verbeeck, C.; Lamy, H.; Calders, S.; Martinez Picar, A.; Calegaro, A.; Anciaux, M.
Year-to-year comparison of BRAMS forward scatter observations of selected meteor showers
Proceedings of IMC2019, Bollmansruh, Germany, 3-6 October 2019, 2020

37. Verbeeck, C.; Lamy, H.; Calders, S.; Martínez Picar, A.; Calegaro, A.
BRAMS forward scatter observations of major meteor showers in 2016–2019
Proceedings of IMC2019, Bollmansruh, Germany, 3-6 October 2019, 2020

38. Verbeeck, C.
Meteor Astronomy with the International Meteor Organization
Nepal Astronomical Society (NASO), 12 December 2020

39. West, M.; D'Huys, E.
The Sun in 2019
ESA webpage, 20 January 2020

List of abbreviations

~	About, proportional to
1D	One dimensional
2D	Two dimensional
3D	Three dimensional
6U	6 Units (cubesats)
Å	Ångstrom (0.1 nm)
A	Article
AAS	American Astronomical Society
ABL	Atmospheric Boundary Layer
ACE	Advanced Composition Explorer
ACFJ	Australia, Canada, France and Japan consortium
AFFECTS	Advanced Forecast For Ensuring Communications Through Space
AGU	American Geophysical Union
AIA	Atmospheric Imaging Assembly (SDO)
ALC	Automatic LIDAR Ceilometer
ALIS	Auroral Large Imaging System
ALTIUS	Atmospheric Limb Tracker for Investigation of the Upcoming Stratosphere
AM	Amplitude Modulation
AOGS	Asia Oceania Geosciences Society
APS	American Physical Society
AR	(1) Active Region ; (2) Annual Report
ARCAS	Augmented Resolution Callisto Spectrometer
ASGARD	An educational space programme for schools (no acronym)
ASOPOS	Assessment of Standard Operating Procedures for OzoneSondes
ASPIICS	Association of Spacecraft for Polarimetric and Imaging Investigation of the Corona of the Sun (PROBA-3)
ASTERIX	Absolute Solar-TErrestrial Radiation Imbalance eXplorer
AU, au	Astronomical Unit; about 150 million km
B_0	Heliographic latitude of the central point of the solar disk (The range of B_0 is $\pm$7.23°)
BE	Belgium
BELSPO	Belgian Science Policy Office
BeNELux	Belgium, The Netherlands, and Luxembourg
BIRA	Koninklijk Belgisch Instituut voor Ruimte-Aëronomie
BISA	Royal Belgian Institute for Space Aeronomy
BPIM	BIRA Plasmasphere-Ionosphere Model
BRAIN-be	Belgian Research Action through Interdisciplinary Networks (BELSPO)
BRAMS	Belgian RAdio Meteor Stations
BUKS	Belgium, UK, and Spain
B.USOC	Belgian User Support and Operation Centre
Bz	Component of the IMF perpendicular to the ecliptic ("north-south" component)
°C	Degrees Celsius
C	Capacitor
C1, C2, C3	Coronagraphs of LASCO (SoHO)
C-class flare	Common x-ray flare
C/NOFS	Communications/Navigation Outage Forecasting System
C/N_0	Carrier-to-Noise
CA	COST Action (COST)
Ca II H	A blue line in the solar spectrum at 396.85 nm
Ca II K	A blue line in the solar spectrum at 393.37 nm
CACTus	Computer Aided CME Tracking software
CALLISTO	Compound Astronomical Low frequency Low-cost Instrument for Spectroscopy and Transportable Observatory
CCMC	Community Coordinated Modeling Center
CERES	Clouds and the Earth's Radiant Energy System
CESRA	Community of European Solar Radio Astronomers
CH	Coronal Hole
CHARM	Contemporary physical challenges in Heliospheric and AstRophysical Models

CINDI	Coupled Ion-Neutral Dynamics Investigation
CIR	Co-rotating Interaction Region
Cluster	ESA/NASA mission to study the Earth's magnetosphere (no acronym)
cm, cm^2	centimeter, square centimeter
CME	Coronal Mass Ejection
CMOS	Complementary Metal-Oxide-Semiconductor
CNES	Centre national d'études spatiales (France)
CNRS	Centre national de la recherche scientifique (France)
Co.	Cooperation
CO_2	Carbon Dioxide
COMESEP	COronal Mass Ejections and Solar Energetic Particles
COPUOS	COmmittee on the Peaceful Uses of Outer Space (UN)
COR (1/2)	Coronagraph (Inner/Outer) onboard STEREO
CORS	Continuously Operating Reference Stations (GNSS)
COSPAR	COmmittee on SPAce Research
COST	(European) COoperation in Science & Technology
COTS	Commercial off-the-shelf
COVID-19	Coronavirus disease 2019
CR	Carrington Rotation
CRMSE	Centred Root Mean Square Errors
CSL	Centre Spatial de Liège
CubeSat	A small satellite measuring 10cm x 10cm x 10cm
CWS	Cross-track Wind Sensor
Δ	Delta (difference)
D2D	Digisonde-to-Digisonde
D3S	Distributed Space weather Sensor System
dB-Hz	decibel-Hertz (bandwidth relative to 1 Hz)
DIARAD	DIfferential Absolute RADiometer
Digisonde	Digitally Integrating Goniometric IonoSONDE
DLR	German Aerospace Center
DOI	Digital Object Identifier
DoY	Day of Year
DPP	Division of Plasma Physics (APS)
DPS	Division for Planetary Sciences (EPSC)
Dr.	Doctor
DSCOVR	Deep Space Climate Observatory
Dst	Disturbance Storm Time index (geomagnetic)
E	East
E, E_- , E_+	Energy, Ingoing energy, Outgoing energy
e.g.	exempli gratia (example given)
e-Callisto	extended Compact Astronomical Low-cost Low-frequency Instrument for Spectroscopy and Transportable Observatory
E-GVAP	EUMETNET GNSS water Vapour Programme
EC	European Commission
ECC	Electrochemical Concentration Cell
ECMWF	European Centre for Medium-Range Weather Forecasts
ed.	Edition
Eds.	Editors
EGNOS	European Geostationary Navigation Overlay Service
EGNSS	European GNSS
EGU	European Geosciences Union
EISCAT	European Incoherent SCATter scientific association
EIT	Extreme ultraviolet Imaging Telescope (SOHO)
EM	(1) Electromagnetic (2) Engineering Model
EPN	EUREF Permanent Network
EPOS	European Plate Observing System
E-PROFILE	EUMETNET Profiling Programme
EPS	European Physical Society
EPSC	European Planetary Science Congress
EPT	Energetic Particle Telescope (PROBA-V)
ERA-Interim	ECMWF Re-Analysis Interim
erg	10^{-7} Joule
Es	Sporadic E-layer (ionosphere)

ES	Earth System (Science and Environmental Management (COST)
ESA	European Space Agency
ESAC	European Space Astronomy Centre
ESC	Expert Service Centre
ESD	ElectroStatic Discharge
ESCAPE	European SpaceCraft for the study of Atmospheric Particle Escape
ESERO	European Space Education Resource Office
ESOC	European Space Operations Centre
ESPD	European Solar Physics Division (EPS)
ESPM	European Solar Physics Meeting
ESTEC	European Space Research and Technology Centre
ESWS	European Space Weather Symposium (2020)
ESWW	European Space Weather Week
et al.	et alii (and other)
EU	European Union
EUHFORIA	European Heliospheric Forecasting Information Asset
EUI	Extreme-Ultraviolet Imager (Solar Orbiter)
EUMETNET	Network of European Meteorological Services
EUMETSAT	European Organisation for the Exploitation of Meteorological Satellites
EUREF	EUropean Reference Frame
EUV	Extreme Ultraviolet
EUVI	Extreme Ultraviolet Imager (STEREO/SECCHI; LGRRS)
EUVM	EUV Monitor (MAVEN)
EVE	Extreme ultraviolet Variability Experiment (SDO)
ExoMars	Exobiology on Mars (ESA, Roscosmos)
$F_{10.7\ cm}$	Solar radio flux at 10.7 cm wavelength
F10.7P	Proxy for $F_{10.7\ cm}$ solar radio flux
F_2	Main ionospheric layer
F_{30}	Solar radio flux at 30 cm wavelength
FAIR	Findable, Accessible, Interoperable, and Re-usable (GNSS)
Fe IX-X	8 resp. 9 times 8 ionized iron
FITS	Flexible Image Transport System
FM	(1) Flight Model (2) Frequency Modulation
FMI	Finnish Meteorological Institute
FNRS	Fonds National de la Recherche Scientifique
foF2	Critical frequency F2-layer
FOV	Field-Of-View
FP7	Framework Programme 7 (EU)
FPA	Focal Plane Assembly
FReSWeD	Future Research on Space Weather Drivers
FRS	Fonds de la Recherche Scientifique
FSI	Full Sun Imager (Solar Orbiter / EUI)
FTE	Full-Time Equivalent
FUV	Far Ultraviolet
G, GB	Gigabyte (10^9 bytes)
Galileo	European GNSS
GAW	Global Atmospheric Watch (WMO)
GBO	Ground-Based Observatory
GCR	Galactic Cosmic Rays
GEANT-4	GEometry ANd Tracking (simulation platform)
GeV	Giga electronvolt (10^9 . 1.6 . 10^{-19} Joule)
GFZ	Deutsches GeoForschungsZentrum (German Research Centre for Geosciences)
GHz	Gigahertz (10^9 Hz)
GLE	Ground Level Enhancement
GLONASS	GLObal NAvigation Satellite System (Russia)
GNSS	Global Navigation Satellite System
GNSS4SWEC	Advanced GNSS tropospheric products for the monitoring of Severe Weather Events and Climate
GOES	Geostationary Operational Environmental Satellite

GOME	Global Ozone Monitoring experiment (SCIAMACHY)
GOMESCIA	GOME/SCIAMACHY/GOME-2
GONG	Global Oscillation Network Group
GPS	Global Positioning System (USA)
GRAPE	GNSS Research and Application for Polar Environment
GSFC	Goddard Space Flight Center
h	(1) hour ; (2) Planck's constant ($6.62607004 \times 10^{-34}$ m^2 kg / s)
H	(1) Hydrogen ; (2) Heat flux
H-alpha (Hα)	A red visible spectral line at 656.28 nm created by Hydrogen
HF	High Frequency (3-30 MHz)
HI	Neutral atomic Hydrogen
H2020	Horizon 2020 (EU)
He, He II	Helium, ionized Helium
HEK	Heliophysics Events Knowledgebase
HF	High Frequency
HI	Heliospheric Imager (STEREO)
h_mF_2	peak density height of F_2-layer
HMI	Heliospheric and Magnetic Imager (SDO)
HRI	High Resolution Imager (Solar Orbiter / EUI)
HSRS	Humain Solar Radio Spectrograph
HSS	High Speed Stream
HuRAS	Humain Radio Astronomy Station
HXR	Hard x-rays
Hz	Hertz (per second)
I-V	Current-Voltage
IAG	International Association of Geodesy
IAGA	International Association of Geomagnetism and Aeronomy
IAS	Institut d'Astrophysique Spatiale (France)
IASB	Institut royal d'Aéronomie Spatiale de Belgique
IASC	International Arctic Science Committee
IAU	International Astronomical Union
ICAO	International Civil Aviation Organization
ICME	Interplanetary CME
ICSO	International Conference on Space Optics
ICT	Information and Communication Technologies
IDL	Interactive Data Language
i.e.	"id est" (that is)
IEEE	Institute of Electrical and Electronics Engineers
IGS	International GNSS Service
IHDEA	International Heliophysics Data Environment Alliance
IMC	International Meteor Conference
IMF	Interplanetary Magnetic Field
IMO	International Meteor Organization
INAOE	Instituto Nacional de Astrofísica, Óptica y Electrónica - National Institute for Astrophysics, Optics and Electronics (Mexico)
INGV	Istituto nazionale di geofisica e vulcanologia (Italy)
InSight	Interior Exploration using Seismic Investigations, Geodesy and Heat Transport
INSPIRE	International Satellite Program in Research and Education
IOP	Institute of Physics
IPAG	Institut de Planétologie et d'Astrophysique de Grenoble
IPF	International Polar Foundation
IPSL	Institut Pierre-Simon Laplace
IR	Infrared
IRAP	Institut de Recherche en Astrophysique et Planétologie (France)
IRENE	International Radiation Environment near Earth
IRI	International Reference Ionosphere
IRM	Institut Royal Météorologique
ISAS	Institute of Space and Astronautical Science
ISC	(1) International Science Council; (2) International Steering Committee

ISN	International Sunspot Number
ISO	International Organization for Standardization
ISS	International Space Station
ISSI	International Space Science Institute
ISSS	(1) International School of Space Science; (2) International School/Symposium for Space Simulations
ISWAT	International Space Weather Action Teams (COSPAR)
IT	Information Technology
IUGG	International Union of Geodesy and Geophysics
IVOA	International Virtual Observatory Alliance
IWV	Integrated Water Vapour
JGR	Journal of Geophysical Research
jHV	jHelioViewer
JPEG	Joint Photographic Experts Group
JSON	JavaScript Object Notation
JSWSC	Journal of Space Weather and Space Climate
JUICE	JUpiter ICy moons Explorer
k	wave number
K	(1) Local K-index: A 3-hour geomagnetic index, ranging from 0 (quiet) to 9 (extremely severe storm); (2) degrees Kelvin
K*	Local 1-minute resolution K index
Ka-band	"Kürz above": Radio frequency band from 27-40 GHz
KAW	Kinetic Alfvén Waves
keV	kilo electronvolt (10^3 . 1.6 . 10^{-19} Joule)
kHz	kilo Hertz (10^3 /second)
km	kilometer
km/s	kilometers per second
KMI	Koninklijk Meteorologisch Instituut
KNMI	Koninklijk Nederlands Meteorologisch Instituut
K_p	A geomagnetic index, ranging from 0 (quiet) to 9 (extremely severe storm)
KSO	Kanzelhöhe Solar Observatory
KSB	Koninklijke Sterrenwacht van België
KUL	Katholieke Universiteit Leuven
kV	kiloVolt (10^3 Volt)
λ	wavelength
l/m²	Liter per square meter
L-class	Large class satellite (ESA)
L	Letter (manuscript)
L*	Set of Earth's magnetic field lines which cross the Earth's magnetic equator at * earth radii from the centre of the Earth (e.g. L = 2)
L_0	Heliographic longitude of the central point of the solar disk
L1, … , L5	First, … , fifth Lagrangian point
L1, L2	GPS frequencies: L1 = 1575.42 MHz, L2 = 1227.60 MHz
LaRa	Lander Radio science (ExoMars)
LASCO	Large Angle Spectrometric Coronagraph (SOHO); small (C2) and wide (C3) field of view
Lat	Latitude
LATMOS	Laboratoire ATmosphères, Milieux, Observations Spatiales (France)
LDE	Long Duration Event
LEO	Low Earth Orbit
LGGRS-EUVI	LaGRange Remote Sensing instruments (EUVI)
LIDAR	LIght Detection And Radar
LIEDR	Local Ionospheric Electron Density profile Reconstruction
LMSAL	Lockheed Martin Solar and Astrophysics Laboratory
LOC	Local Organising Committee
LOFAR	Low-Frequency Array
Lon	Longitude
LOTUS	Long-term Ozone Trends and Uncertainties in the Stratosphere
Ls	Solar longitude
LT	Local Time
LTI	Lower thermosphere and ionosphere region
LUCI	Lagrange eUv Coronal Imager (Lagrange)
LVF	Linear Variable Filter

Ly-α	Lyman-alpha, a spectral line in the VUV at 121.6 nm
LYA	Ly-α
LYRA	Large Yield Radiometer, formerly called Lyman Alpha Radiometer (PROBA2)
LWS	Living With a Star
μm	micrometer (10^{-6} meter)
M-class	Medium class satellite (ESA)
M-class flare	Medium x-ray flare
m, m^2, m^3	Meter, square meter, cubic meter
MAJIS	Moons And Jupiter Imaging Spectrometer (JUICE)
MAVEN	Mars Atmosphere and Volatile EvolutioN (NASA)
MAX-DOAS	Multi-axis differential optical absorption spectroscopy
MB	Megabyte (10^6 bytes)
mbar	millibar
MER	Mars Exploration Rover
METIS	Multi Element Telescope for Imaging and Spectroscopy (SolO)
MeV	Mega electronvolt (10^6 . 1.6 . 10^{-19} Joule)
MHD	Magnetohydrodynamics
MHz	Megahertz (10^6/s)
MIT	Massachusetts Institute of Technology
MJD	Modified Julian Day
ML	Maximum Likelihood
MLH	mixing layer height
MLT	Magnetic Local Time
mm	millimeter (10^{-3} meter)
mm/s	millimeter per second
MOMA	Multi-wavelength Observations and Modelling of Aurora
MoMo	Model of Mars Ionosphere
MPS	Max Planck Institute for Solar System Research
ms	millisecond (10^{-3} second)
MULTI-VP	multiple-1D solar wind model (not an acronym)
MUV	Mid Ultraviolet
ν	Frequency
N	North
N-S	North-South
N_2	Nitrogen
nA	nano Ampère (10^{-9} meter)
NASA	National Aeronautics and Space Administration
NASO	Nepal Astronomical Society
NASU	National Academy of Sciences of Ukraine
NATO	North Atlantic Treaty Organization
NeQuick	Electron density Quick calculation model (ionospheric model)
Net-TIDE	Pilot Network for Identification of Travelling Ionospheric Disturbances in Europe
NIR	Near IR
NL	The Netherlands
NM	Neutron Monitor
nm	nanometer (10^{-9} meter)
NMDB	Neutron Monitor DataBase
N_mF_2	peak density of F_2-layer
No.	Number of
NO_2	Nitrogen dioxide
NOAA	National Oceanic and Atmospheric Administration
NOMAD	Nadir and Occultation for MArs Discovery (ExoMars)
NP	Non-parametric test
NRT	Near Real Time
ns	nanosecond (10^{-9} second)
NSO	National Solar Observatory
nT	nano-Tesla (10^{-9} Tesla)
NUV	Near Ultraviolet
NWC	Northwest Cape of Australia
NWP	Numerical Weather Prediction
O	Oxygen
O_3	Ozone
ODC	On Duty Center (PECASUS)
ODYN	Open-Source Software Analysis Tool to Investigate Space Plasma Turbulence and Nonlinear DYNamics
ORB	Observatoire Royal de Belgique
ORFEES	Observation Radio Fréquences pour l'Etude des Eruptions Solaires
P	The position angle between the geocentric north pole and the solar rotational north pole measured eastward from geocentric north. The range in P is $\pm$26.3°

P2SC	PROBA2 Science Center
PARAFOG	Predictive Alert of RAdiation FOG
PB	Petabyte (10^{15} bytes)
PBC	Primary Backup-Center (PECASUS)
PECASUS	Pan-European Consortium for Aviation Space weather User Services
PFSS	Potential Field Source Surface
pfu	particle (proton) flux unit: the number of particles registered per second, per square cm, and per steradian
PhD	Doctor of Philosophy
PI	Principal Investigator
PICASSO	PICo-satellite for Atmospheric and Space Science Observations
PRESTO	Fast warning message for important SWx events
PROBA	PRoject for OnBoard Autonomy
PROBA-V	PROBA-Vegetation
PROBE	PROfiling the atmospheric Boundary layer at European scale (COST)
PRODEX	PROgramme for the Development of scientific Experiments
ps	picosecond (10^{-12} second)
PTB	Physikalish-Technische Bundesanstalt (Germany)
PYRILIOS	A campaign for NIR Sun irradiance measurement, campaign name based on 'Sun' and 'Fire' in Greek (no acronym)
Q&A	Questions and Answers
QE	Quantum Efficiency
QPP	Quasi-periodic pulsation
ρ_T	gyroradius
R	Resistor
R&D	Research and Development
R-ESC	Space Radiation ESC
RAS	Royal Astronomical Society
RC circuit	An electric circuit composed of resistors and capacitors
RC time	The time constant (in seconds) of an RC circuit
ReSourCE	Radio Sciences Research on AntarCtic AtmosphEre
RF	Radio Frequency
RHESSI	Reuven Ramaty High Energy Solar Spectroscopic Imager
RISE	Rotation and Interior Structure Experiment (InSight)
RMI(B)	Royal Meteorological Institute (of Belgium)
RMS	Root Mean Square
ROB	Royal Observatory of Belgium
Roscosmos	Russian Space Agency
RSSB	Royal Statistical Society of Belgium
R_{sun}	Solar radius (~ 696,000 km)
RWC	Regional Warning Center
σ	sigma (confidence level)
s	second
S	South
S-band	Radio frequency band from 2-4 GHz
S/C	Spacecraft
S-class	Small class satellite (ESA)
SAA	South Atlantic Anomaly
SAFIRE	SolAr Flux monItoRing Equipment
SANSA	South African National Space Agency
SAR	(1) Superactive region; (2) Synthetic Aperture Radar
SBC	Secondary Backup-Center (PECASUS)
SC24, SC25	Solar Cycle 24, Solar Cycle 25
SCAR	Scientific Committee on Antarctic Research
SCIAMACHY	SCanning Imaging Absorption spectroMeter for Atmospheric CHartographY (ENVISAT)
SCK-CEN	Studiecentrum voor Kernenergie - Centre d'Etude de l'Energie Nucléaire
SCOPE	Solar Coronagraph for OPErations
SCOSTEP	Scientific Committee on Solar Terrestrial Physics
SDO	Solar Dynamics Observatory
SDR	Software Defined Radio
SECCHI	Sun Earth Connection Coronal and Heliospheric Investigation (STEREO)
SEP	Solar Energetic Particle
SEPEM	Solar Energetic Particle Environment Modelling

SEU	Single Event Upset
SFU, sfu	Solar Flux Unit (10^{-22} W m^{-2} Hz^{-1})
SHINE	Solar Heliospheric & Interplanetary Environment
SIDC	Solar Influences Data analysis Center
SILSO	Sunspot Index and Long-term Solar Observations
SIMBA	Sun-earth IMBAlance
SKA	Square Kilometre Array
SLP	Sweeping / Segmented / Single/ Split / Spherical Langmuir Probe
SLT	Solar Local Time
SM	Spare Model
SMILE	Solar wind-Magnetosphere-Ionosphere Link Explorer (ESA)
sms	short message service
SN	(1) Sunspot Number ; (2) Space weather and Near-earth objects ; (3) Standard normal homogenization tests
SOC	Science Operations Centre
SOHO	SOlar & Heliospheric Observatory
SOIR	Solar Occultation in the Infrared
SOL-ACES	SOLar Auto-Calibrating Extreme ultraviolet and ultraviolet Spectrometers (ISS-SOLAR)
SOLAR	ESA project onboard ISS (Columbus Laboratory), controlled by B.USOC, and having 3 main instruments: SOVIM, SOLSPEC and SOL-ACES
SOLARNET	European network of solar physics researchers and facilities (H2020)
SOLIS	Synoptic Optical Long-term Investigations of the Sun (NSO)
SolO	Solar Orbiter
SOLSPEC	SOLar SPECtral irradiance measurements (ISS-SOLAR)
SOVIM	Solar Variations and Irradiance Monitor (ISS-SOLAR)
SP4GATEWAY	Space Plasma Physics Payload Package conceptual design for the Deep Space Gateway Lunar Orbital Platform
SPACEMON	Space Environment Monitoring workshop
SPADE	Small Phased Array DEmonstrator
SPD	Solar Physics Division (AAS)
SPENVIS (-NG)	SPace ENVironment Information System (- Next Generation)
SPICE	Spectral Imaging of the Coronal Environment (SolO)
SPIE	Society of Photo-optical Instrumentation Engineers
SPRING	Solar Physics Research Integrated Network Group (SOLARNET)
SPS	Science for Peace and Security (NATO)
sr	steradian
SRB	Solar Radio Burst
SREM	Standard Radiation Environment Monitor (Integral, Rosetta)
SSA	(1) Space Situational Awareness ; (2) singular spectrum analysis
SSCC	SSA Space Weather Coordination Centre
SSI	Solar Spectral Irradiance
SSN	SunSpot Number
STAFF	Solar Timelines viewer for AFFECTS
STCE	Solar-Terrestrial Centre of Excellence
STCL	Space Technology & Calibration Laboratories
STEREO	Solar-TErrestrial RElations Observatory
STM	Structural Model
SunPy	software library for solar physics based on Python
SUVI	Solar Ultraviolet Imager (GOES)
SW	Space Weather (journal)
SWAP	Sun Watcher using APS detector and image Processing (PROBA2)
SWAVES	STEREO WAVES
SWE	Space Weather

SWEC	Space Weather Education Center
SWEK	Space Weather Event Knowledgebase
SWIC	Space Weather Introductory Course
SWPC	Space Weather Prediction Center (USA)
SWSC	Journal of Space Weather and Space Climate
SWT	Science Working Team
SWx	Space weather
SXR	Soft x-rays
SZA	Solar Zenith Angle
τ	Time
T, TB	Terabyte (10^{12} bytes)
TEC	Total Electron Content
Tech-TIDE	Warning and Mitigation Technologies for TIDs Effects
TECu	TEC unit ($10^{16} e \cdot m^{-2}$)
THEMIS	Time History of Events and Macroscale Interactions during Substorms (NASA mission)
TID	Travelling Ionospheric Disturbance
TROPOMI	TROPOspheric Monitoring Instrument
TSI	Total Solar Irradiance
UCD	Unified content descriptors
UCL	Université Catholique de Louvain
UHF	Ultra High Frequency (0.3 - 3 GHz)
UK	United Kingdom
ULB	Université libre de Bruxelles
UNCOPUOS	United Nations Committee on the Peaceful Use of Outer Space
URAN	Ukrainian Radio Interferometer of NASU
URSI	International Union of Radio Science - Union Radio-Scientifique Internationale
US(A)	United States (of America)
USET	Uccle Solar Equatorial Table
UT(C)	(Coordinated) Universal Time
UV	Ultraviolet
UVC-II	Second solar ultraviolet radiometer comparison campaign
v	Velocity (speed)
V	Volt
V1, 2, …	Version 1, 2, …
VACNT	Vertically Aligned Carbon Nanotubes
VarSITI	Variability of the Sun and Its Terrestrial Impact
VHF	Very High Frequency
VIP	Very Important Person
VIRGO	Variability of solar IRradiance and Gravity Oscillations (SoHO)
VIS	Visible
VKI	Von Karman Institute
VLF	Very Low Frequency
VOEvent	Virtual Observatory Event
Vol.	Volume
VSWMC	Virtual Space Weather Modelling Centre
VSx	Virtual Spacecraft
VTEC	Vertical TEC
VUB	Vrije Universiteit Brussel
VUV	Vacuum Ultraviolet
VVS	Vereniging Voor Sterrenkunde
W	(1) Watt; (2) West
W/m^2	Watt per square meter
WAVES	Radio and plasma wave investigation (WIND, STEREO)
WDC	World Data Center
WFOV	Wide Field Of View
WG	Working Group
WGN	WerkGroepNieuws (journal of IMO)
WMO	World Meteorological Organization
WP	Work Package
WRC	World Radiation Center
WS	Workshop
WSA	Wang-Sheeley-Arge (model for solar wind)
X-band	Radio frequency band from 8-12 GHz
X-class flare	Extreme x-ray flare
XRT	X-Ray Telescope (Hinode)
ZTD	Zenith Total Delay